

(NASA-CR-135351) THE EFFECT OF MINOR ADDITIONS OF TITANIUM ON THE FRACTURE TOUGHNESS OF Fe-12Ni ALLOYS AT 77K Final Report, 1 Nov. 1976 - 31 Oct. 1977 (Kentucky Univ.) · 92 p HC A05/MF A01 CSCL 11F G3/26 07285 N78-19259 Unclas

THE EFFECT OF MINOR ADDITIONS OF TITANIUM ON THE  
FRACTURE TOUGHNESS OF Fe-12Ni ALLOYS AT 77K

by

H. CONRAD, C. YIN AND G. A. SARGENT

Prepared For

National Aeronautics and Space Administration

January 16, 1978

Contract NSG-3125

Final Report

Technical Management  
NASA Lewis Research Center  
Cleveland, Ohio  
Material and Structures Division  
Joseph R. Stephens

Department of Metallurgical Engineering and Materials Science  
University of Kentucky  
Lexington, KY 40506

## CONTENTS

	Page
ABSTRACT	
INTRODUCTION	1
EXPERIMENTAL PROCEDURE	4
Materials	4
Optical Microscopy	4
Transmission Electron Microscopy (TEM)	5
Scanning Electron Microscopy (SEM)	5
Auger Electron Spectroscopy (AES)	6
RESULTS	8
Mechanical Properties	8
Scanning Electron Microscopy (SEM)	9
Optical Microscopy	10
Transmission Electron Microscopy (TEM)	11
Auger Electron Spectroscopy (AES)	11
DISCUSSION	13
SUMMARY	16
REFERENCES	18

THE EFFECT OF MINOR ADDITIONS OF TITANIUM ON THE FRACTURE TOUGHNESS  
OF Fe-12Ni ALLOYS AT 77K

H. Conrad, C. Yin and G. Sargent

Metallurgical Engineering and Materials Science Department  
University of Kentucky  
Lexington, KY 40506

Abstract

The reasons for the improvement in the fracture toughness of an Fe-12Ni base alloy at 77K by the addition of small amounts of Ti were investigated employing optical microscopy, TEM, SEM and Auger electron spectroscopy. Ti additions ranging from 0.18 to 0.99 at.% and heat treatments of 2 hours at 550, 685 and 820°C respectively followed by a water quench were considered, since previous work by Witzke and Stephens had shown that maximum  $K_{Icd}$  occurred for an Fe-12Ni-0.18Ti alloy heat treated at 685°C.

It was here found that  $K_{Icd}$  at 77K for all the alloys and heat treatments correlated with the fraction of ductile fracture compared to intergranular and cleavage fracture, the latter modes being predominant in the Fe-12Ni base alloy without Ti additions. Cubic and rectangular shaped inclusions were noted in the SEM fractographs of the alloys with the Ti additions. A fine precipitate was observed by TEM for the Fe-12Ni-0.18Ti alloy heat treated at 550°C; this precipitate was not observed for the 685 and 820°C heat treatments of the same alloy. Auger mappings of the fracture surfaces indicated a weak to moderate association of the interstitials C, N and O with Ti, the degree of which depended on the particular interstitial and the heat treatment temperature.

It was concluded that the increase in  $K_{Icd}$  due to the initial 0.18 at.% addition of Ti was due to a scavenging of interstitials which normally segregate at the grain boundaries and to the refinement of the microstructure. The subsequent decrease in  $K_{Icd}$  with further Ti additions was attributed to the increase in flow stress and slight lowering of the fracture stress resulting from these additions. It was further inferred that the effects of Ti additions and heat treatment on the flow and fracture stresses may be due in large part to their influence on the amount, size and distribution of the precipitate which was observed.

THE EFFECT OF MINOR ADDITIONS OF TITANIUM ON THE FRACTURE TOUGHNESS  
OF Fe-12Ni ALLOYS AT 77K

H. Conrad, C. Yin and G. A. Sargent

Introduction

One of the factors to be considered in the development of iron-base alloys for cryogenic applications is the detrimental effect on toughness of impurity elements such as oxygen, nitrogen and sulfur (1-4). This problem is generally controlled by adding reactive metals to the melt which combine with these impurities and thereby reduce or eliminate their detrimental effect. Recognizing this, Witzke and Stephens (5) investigated the effects of minor additions (up to 4 at.%) of eleven reactive metals on the tensile properties and fracture toughness of a binary Fe-12Ni base alloy. This base alloy was chosen because prior work by Jin et al (6) indicated that an Fe-12Ni alloy with titanium additions was ductile at 77K. In their study Witzke and Stephens (5) found that Al, Ti, V, Nb and Ta improved the fracture toughness of the Fe-12Ni alloy at 77K; Zr and Hf and Ce, La and Y were less effective and Si had no effect. Further, they found that the toughness was dependent on the concentration of the reactive metal (peaking sharply at relatively small concentration for most additions) and the heat treatment employed (in the range of 550 to 820°C followed by a water quench). Concurrent optical and transmission electron microscopy (TEM) studies by them indicated that: (a) substructure plays a minor role in fracture toughness and (b) precipitate particles were not generally observed except in those alloys containing strong carbide-forming additions such as Hf and Ta. Scanning electron

microscopy (SEM) examination of the fracture surfaces of the broken fracture toughness specimens revealed that ductile fracture (dimpled rupture) occurred in varying degrees, being most evident in the toughest materials.

The work of Witzke and Stephens (5) thus clearly established that significant improvements can be obtained in the fracture toughness of the Fe-12Ni alloy by the minor additions of certain reactive metals, especially Al, Ti and Nb. However, the nature of the gettering which lead to the improved fracture toughness was not clearly ascertained, nor was the reason for the strong influence of the heat treatment. The present investigation was therefore undertaken to provide additional information regarding these two unresolved questions. A better understanding of these aspects of the subject is important in optimizing the beneficial effects of the reactive metal additions and in providing guidelines for the development of improved alloys.

The approach taken in this investigation was to characterize in more detail the microstructure (using optical microscopy and TEM), solute distribution (using Auger electron spectroscopy), and fracture surface morphology (using scanning electron microscopy, SEM) of the tensile and slow bend fracture toughness specimens which had been previously tested by Witzke and Stephens (5) and which were made available to the present authors. The initial studies focused on the Fe-12Ni - x Ti alloys because: (a) a large increase in the fracture toughness of the Fe-12Ni base alloy had been obtained by the addition of titanium, (b) a significant effect of heat treatment on the fracture toughness had occurred and (c) preliminary SEM examination of the fracture surface of broken fracture toughness specimens by the present authors revealed a good number of inclusions within the dimples of the ductile fracture regions.

The titanium additions considered in this study ranged from 0 to 1.0 at.% and the heat treatments consisted of 2 hours at 550, 685 and 820°C respectively, followed by a water quench. Within this range of composition and heat treatments, Witzke and Stephens (5) found that maximum fracture toughness occurred for the addition of 0.18 at.% (0.15 wt.%) Ti combined with the 685°C heat treatment.

## Experimental Procedure

### 1. Materials

The Fe-12Ni and Fe-12Ni-xTi alloy tensile and notch bend fracture toughness specimens considered here (chemical compositions of which are given in Table I) were provided by Witzke and Stephens; the preparation, heat treatment and testing procedure of the specimens have been presented in detail elsewhere (5). Briefly, ingots of the alloys were prepared by nonconsumable arc melting in an argon atmosphere from high purity Fe, Ni and Ti. To adequately homogenize the ingots, each alloy was given a minimum of four melts. The ingots were hot rolled at 1100°C to the desired thickness (7 mm for the notch bend specimens and 1 mm for the tensile test specimens) and air cooled to room temperature. Tensile and notch bend specimens cut from the rolled sheet were then heat treated for two hours at 550, 685 and 820°C respectively, followed by a water quench. According to the Fe-Ni phase transformation diagram for continuous heating or cooling shown in Fig. 1, the temperatures of the heat treatments are in the  $\alpha$ ,  $\alpha + \gamma$  and  $\gamma$  phase fields respectively. Differential thermal analysis (7-9) indicates that the Ti additions of 0.18 to 0.99 at.% considered here are not expected to appreciably alter the phase transformation diagram.

### 2. Optical Microscopy

Transverse sections were cut from the broken notch bend fracture toughness specimens, mounted in a cold-setting resin and polished using conventional metallographic techniques. The polished surfaces were etched in a solution consisting of 33 parts water, 33 parts nitric acid, 33 parts acetic acid, and 1 part hydrofluoric acid, which was further diluted to 1 part



distilled water. Etching time was varied depending on the heat-treatment.

### 3. Transmission Electron Microscopy

Transverse sections with a thickness of 0.38mm (0.015 in.) were cut from the broken notch bend specimens and mounted on the flat surface of a ceramic circular disk with double stick Scotch tape. The specimens were then polished on both sides using silicon carbide papers going from 240 to 600 grit under flowing water to a thickness of about 0.15mm (0.006 in.), following which they were chemically polished in a solution of 5% hydrofluoric acid in 95%  $H_2O_2$  to a thickness of 0.10mm (0.004 in.). Thin foil samples suitable for TEM examination were then prepared from these specimens by the Fischione twin-jet polisher using an electrolyte of 250ml methonal, 150ml butal alcohol and 20ml perchloric acid.

### 4. Scanning Electron Microscopy

One of the broken halves of the notch bend fracture toughness specimens was mounted on the standard specimen holder of a Phillips Stereoscon-Mark 2A SEM, using a silver paste as the mounting glue to avoid buildup of a surface charge. The fracture surface of the specimen was then examined with the emissive mode operated at 25KV and with the primary beam normal to the surface. The percentage of ductile fracture (compared to intergranular and cleavage) and the dimple size of the ductile fracture regions were determined from SEM photomicrographs. The dimple size was measured by the linear intercept method on those micrographs which were considered to be most representative of the morphology of the fracture surface. The percentage of ductile fracture was obtained by scanning the entire fracture surface of a specimen at a constant magnification and then averaging the percentage of ductile fracture estimated for each scan area.

## 5. Auger Electron Spectroscopy (AES)

A Varian Auger electron spectrometer system was used to examine the fracture surfaces of the notch bend specimens. Since a suitable electron image of the fracture surface could not be obtained with the scanning sample positioner and TV monitor, a selected random area of the fracture surface was chosen for Auger spectrum analysis and Auger elemental image mapping. Further, since the fracture surfaces had been exposed to the atmosphere for some time prior to the Auger analysis, a technique developed by Palmberg (10), which consists of simultaneous ion bombardment and AES analysis, was employed to remove the influence of any contamination which may have occurred. The basic procedures used here to obtain the final Auger image mapping for the elements C, N, O, Ti, Ni and Fe on a particular selected area of fracture surface were then in general as follows:

a) The fracture surface of a notch bend specimen was mounted on the carousel sample holder located in the center of a bell jar. The bell jar system was then evacuated to a pressure of  $4 \times 10^{-6}$  Pa or better. A schematic of the vacuum chamber and related controlling electronics is given Figure 2.

b) The fracture surface normal was aligned parallel to the primary beam, which was generated by the 10 KeV integral electron gun. Therefore, the angle between the fracture surface normal and the axis of ion bombardment gun was about  $60^\circ$ .

c) The axial position of the sample was adjusted with respect to the Cylindrical Mirror Analyzer (CMA) to obtain a maximum, properly shaped, elastic peak and a measure of the instrumental line width (ILW).

d) After the ILW was defined on a selected surface area, a complete scan of the Auger spectra for specific elements was performed with a primary beam energy of 6.5KeV, filament current of 2.90 A and high voltage output of 1200V. A typical scan is shown in Fig. 3, which gives a plot of the Auger spectra for C and O at a particular area on the fracture surface of the Fe-12Ni-0.18 Ti alloy heat-treated at 685°C.

e) Finally, the Auger elemental image mapping for a fixed Auger electron energy associated with a particular element (for example, O at E = 510eV or 490eV) was obtained by switching the CMA unit to the Auger mapping controlled unit, thereby yielding a map of the distribution of that element on the fracture surface. The mappings were photographed (representing a magnification of 175X) only after about 1 hour of ion bombardment.

## Results

### 1. Mechanical Properties

The true stress-true strain curves (derived from data provided by Witzke and Stephens) for the tensile tests at 77K on the Fe-12Ni-xTi alloys are presented in Fig. 4. Tensile properties extracted from these curves are given in Table II and are plotted as a function of Ti content in Fig. 5. To be noted is that the yield stress  $\sigma_{YS}$  increases significantly with Ti content for the 550°C heat treatment, but does not change appreciably for the 685 and 820°C treatments. On the other hand, the tensile strength  $\sigma_{UTS}$  increases with Ti content for all three heat treatments, the effect being however somewhat larger for the 550°C treatment than for the other two. The true fracture stress  $\sigma_F$  increases appreciably with the addition of 0.18 at.% (0.15 wt.%) Ti for all three heat treatment temperatures; further increase in Ti content generally leads to a slight decrease in  $\sigma_F$ . In general,  $\sigma_F$  tends to increase slightly with increase in heat treatment temperature for all alloy compositions.

Also to be noted from Fig. 5 is that ductility indicators such as the uniform elongation  $\epsilon_u$ , the true fracture strain  $\epsilon_F$  and the strain hardening exponent  $n = d \ln \sigma / d \ln \epsilon$  all go through a maximum at 0.18 at.% (0.15 wt.%) Ti. Considering the effect of heat treatment, the 550°C treatment yields higher values of  $\epsilon_u$  and  $n$  than does the 685 or 820°C treatment, whereas the reverse is true for  $\epsilon_F$ .

The fracture toughness values obtained by Witzke and Stephens (5) are presented as a function of Ti content and heat treatment in Fig. 6. Similar to the ductility indicators, a maximum in  $K_{Icd}$  occurs for the addition of 0.18 at.% (0.15 wt.%) Ti. Of the three heat treatments, the 685°C treatment yields the largest value of  $K_{Icd}$  and the 550°C treatment the lowest.

Thus, of the three tensile test ductility indicators, the true strain at fracture  $\epsilon_F$  correlates best with fracture toughness.

Also included in Fig. 6 is the work to fracture  $W_F$  given by the area under the true stress-true strain curves of Fig. 4. To be noted is that the effects of Ti and heat treatment on  $W_F$  are similar to those on  $K_{Icd}$ . This correlation is further evident in Fig. 7 where  $K_{Icd}$  is plotted versus  $W_F$  for the various Ti additions and heat treatments.

## 2. Scanning Electron Microscopy (SEM)

SEM fractographs of the fracture surfaces of the tensile and fracture toughness specimens tested at 77K are presented in Figs. 8-19. Pertinent features of the structures are summarized in Tables III and IV. A good portion of the fracture surface area of the fracture toughness specimens consists of intergranular and/or cleavage fracture. These brittle fracture modes also occurred in most of the tensile specimens, exceptions being the Fe-12Ni-0.18 Ti alloy heat treated at all three temperatures and Fe-12Ni-0.47 Ti alloy heat treated at 685°C. For these particular additions and heat treatments entirely ductile fracture was observed. Of special significance is that all additions of Ti eliminate the intergranular fracture which occurred in the Fe-12Ni base alloy. In the case of cleavage, the amount of this fracture mode is significantly reduced by the minimum Ti addition of 0.18 at.% (0.15 wt.%) for the 685 and 820°C heat treatments and then increases again at the higher Ti contents.

A plot of the fracture toughness versus the percentage of ductile fracture for the various materials and heat treatments is given in Fig. 20. It is seen that a correlation exists between  $K_{Icd}$  and the percentage of ductile fracture, suggesting that the effects of Ti additions and heat treatments are to a large extent through their effects on the fracture mode.

Inclusions ranging in size from 1 to 5 $\mu$ m and of average spacing of 20-50 $\mu$ m were present on all fracture surfaces. They were for the most part spheroidal in shape in the Fe-12Ni base alloy and cubic or rectangular in the alloys with Ti additions, the relative number of the latter two shapes increasing with increase in Ti content.

Upon comparing the fractographs of broken tensile specimens with those of the fracture toughness specimens, it was found that the tensile specimens exhibited a higher percentage of ductile fracture and a smaller dimple size than the fracture toughness specimens. Also, the dimple size in the tensile specimens was independent of heat treat temperature, while that in the fracture toughness specimens increased with heat treatment temperature. The size, shape and average spacing of the inclusions in the two types of specimens were similar.

### 3. Optical Microscopy

Photomicrographs of the various materials heat treated at the three temperatures are presented in Figs. 21-26. No pronounced effect of the titanium additions on the microstructure is evident for the 550°C heat treatment; however, a refinement of the structure occurs for the 685 and 820°C treatments. Moreover, for the 685°C treatment the titanium addition not only refines the structure, but also yields a more equiaxed structure, which is revealed more clearly by the TEM observations discussed below. For all materials, the structure for the 685°C treatment is finer than that for the 550°C treatment. It coarsens upon increasing the heat treatment temperature from 685 to 820°C, but is still finer for the 820°C treatment than that for the 550°C treatment. These effects of heat treatment on the microstructure are in keeping with the phase diagram of Fig. 1 and the associated  $\gamma \rightarrow \alpha$  transformation; they are similar to those observed by others for Fe-12Ni (8,9) and for Fe-Ni alloys in general (11-13).

#### 4. Transmission Electron Microscopy (TEM)

Typical TEM micrographs of the Fe-12Ni base alloy and of the Fe-12Ni-0.18Ti alloy heat treated at the three designated temperatures are presented in Figs. 27-29. In all cases there exist regions with a high density of dislocations mixed with areas almost devoid of dislocations, the total density of dislocations tending to increase with increase in heat treatment temperature. Fig. 28, which gives the TEM structures for the same crystallographic orientation of the foils, clearly shows that the 0.18 at.% titanium addition has produced a more equiaxed transformation product. A fine precipitate (probably  $\text{Ni}_3\text{Ti}$  or  $\text{Fe}_2\text{Ti}$ ) occurs in the Fe-12Ni-0.18 at.% Ti alloy heat treated at 550°C, whereas there is no evidence of a precipitate in the Fe-12Ni alloy, without titanium, nor in the Fe-12Ni-0.18 at.% Ti alloy heat treated at 685 and 820°C.

#### 5. Auger Electron Spectroscopy

Auger spectrum mappings for the elements Fe, Ni, Ti, C, N and O on the fracture surfaces of the broken fracture toughness specimens tested at 77K are presented in Figs. 30-55. Each image photograph gives the characteristic intensity distribution for the designated element in the photographs provides an indication of the relative affinity between the various elements in a particular alloy. The affinities deduced from the mappings of Figs. 30-55 are summarized in Table V. The results indicate the following:

- a. Nickel is always associated with the iron.
- b. For the Fe-12Ni base alloy heat treated at 550°C, the interstitials N and O are rather uniformly distributed, whereas C tends to avoid regions with high concentrations of Fe and Ni. When the heat treatment temperature is increased to 685°C, C tends to associate with O but still avoids Fe and Ni.

c. For the Fe-12Ni-xTi alloys heat treated at 550 and 685°C, the interstitials C, N and O tend to occur in regions where the Ti atoms are located, the tendency increasing with increase in heat treat temperature. Upon increasing the heat treat temperature to 820°C, a stronger association of N with Ti occurs, but O and C occur in regions of low Ti content.

d. The association of Ni with Ti only occurs for the Fe-12Ni-0.18 Ti alloy heat treated at 550°C and the Fe-12Ni-0.99 Ti alloy heat treated at 820°C.



## Discussion

As pointed out above, Witzke and Stephens (5) found that maximum  $K_{Icd}$  occurred for the Fe-12Ni-0.18Ti alloy heat treated at 685°C. Since the present studies have shown that  $K_{Icd}$  for the various titanium additions and heat treatments correlates with the percentage of ductile fracture, the effects of the Ti additions and heat treatments may be explained in terms of their influence on the fracture mode. The fact that maximum fracture toughness already occurred for the smallest Ti addition (0.18 at.%) is then explained as follows. A simple calculation shows that this amount of Ti is sufficient to combine with all of the interstitial atoms which are present to form simple Ti compounds. The cubic and rectangular inclusions observed in the SEM fractographs are probably these compounds formed during the gettering of the melt. Upon forming these compounds, the concentration of deleterious interstitials (probably oxygen) at the grain boundaries is reduced to the point where their weakening effect is eliminated and intergranular fracture no longer occurs. The decrease in toughness with further additions of Ti beyond 0.18 at.% is then probably due to the fact that such additions produce an increase in the flow stress and at the same time cause a slight decrease in the fracture stress, thereby leading to an earlier (strain wise) intersection of the flow stress curve with the fracture stress curve. This then leads to a decrease in the true fracture strain  $\epsilon_F$  and the work of fracture  $W_F$ , and in turn the fracture toughness, since  $K_{Icd}$  was found to correlate with  $\epsilon_F$  and  $W_F$ . The increase in flow stress with the addition of Ti could be due to an increase in the amount of the precipitate (probably  $Ni_3Ti$  or  $Fe_2Ti$ ) which was observed for the 550°C heat treatment and to a reduction in the fineness of the microstructure associated with the  $\gamma \rightarrow \alpha$  transformation. The influence

of heat treatment, temperature might then also be through its effect on the amount, size and distribution of the precipitate and on the dislocation structure and other microstructural features produced by the  $\gamma \rightarrow \alpha$  transformation. Additional detailed TEM studies are needed to more fully evaluate the microstructural changes which occurred and their possible influence on  $K_{Icd}$ .

The Auger electron spectroscopy mappings of the fracture surfaces indicated that the interstitials C, N and O were only weakly associated with the Ti atoms for the 550 and 685°C heat treatments. Upon increasing the heat treatment temperature to 820°C the association between the N and Ti atoms became stronger, whereas that for the other two interstitials became weaker. This preference of Ti for N is in accord with estimates (14) of the bond energies between Ti and the interstitials C, N and O; see Table VI. It is seen from this table that for each type of measurement the bonding energy between the Ti and N atoms is slightly higher than that for the other two interstitials.

We wish at this point to mention certain limitations regarding the present Auger mappings. Since the amplitude of an Auger peak is proportional to the number of atoms of an element within the first two or three atomic layers of the specimen surface, the morphology of the surface, and any slight contamination of it, will have a significant effect on the strength of the Auger peak and the element image mapping. Moreover, in order to obtain Auger peaks of Ti and/or Ni, the sensitivity of the instrument had to be increased to the limit, which permits the detection of 0.1 at.% of these elements on the surface layers. Therefore, the non-uniform distribution of the Fe and Ni image mappings (Fig. 30) do not represent alloy segregation, but rather that these exist in the surface layers atoms other than just Fe or Ni.

Further, the Auger mappings did not provide any clear evidence for the existence of the inclusions which were observed in the SEM fractographs, nor of the precipitates observed by TEM. This was probably due to the small size of these particles, which was between 1-5 $\mu$ m in the case of the inclusions and less than 1 $\mu$ m in the case of the precipitates. These sizes are near or below the resolving power of the Auger mapping system and hence would not normally show up.

Of additional interest is the fact that only rarely was an inclusion seen in the TEM observations, whereas such inclusions were abundantly evident in the SEM fractographs. A simple calculation based on the average spacing of the inclusions in the SEM fractographs indicated that the probability of seeing one at the magnifications employed in TEM was about one in a thousand.

### Summary

Witzke and Stephens (5) studied the effects of minor additions of Ti (0.18-1.0 at.%) on the fracture toughness at 77K of a Fe-12Ni base alloy heat treated at 550, 685 and 820°C respectively and found that maximum  $K_{Icd}$  occurred for addition of 0.18 at.% Ti heat treated at 685°C. The following is a summary of the more significant findings of the present investigation using optical microscopy, TEM, SEM and Auger electron spectroscopy into the reasons for this improvement in  $K_{Icd}$ :

1.  $K_{Icd}$  at 77K for all alloys and heat treatments considered here correlated with the fraction of ductile fracture compared to intergranular and cleavage fracture, the latter modes being predominant in the Fe-12Ni base alloy without Ti additions.

2. Inclusions 1-5 $\mu$ m in size and 20-50 $\mu$ m spacing were noted in the SEM fractographs of both tensile and fracture toughness specimens tested at 77K. The inclusions were spheroidal in shape in the Fe-12Ni base alloy, but were for the most part cubic or rectangular in the Fe-12Ni-xTi alloys.

3. A refinement in the microstructure occurred as a result of the Ti additions for the 685 and 820°C heat treatments, which temperatures were in the  $\alpha + \gamma$  and  $\gamma$  regions respectively of the phase diagram.

4. A fine precipitate was observed by TEM in the Fe-12Ni-0.18Ti alloy heat treated at 550°C; this precipitate was not seen for the 685 and 820°C heat treatments of this particular alloy.

5. Auger mappings indicated a weak to moderate association of the interstitials C, N and O with Ti, the degree of which depended on the particular interstitial element and the heat treat temperature.

6. To explain these findings the following were inferred from the results obtained:

- a. The increase in  $K_{Icd}$  resulting from the initial addition of 0.18 at.% Ti is due to: (1) the scavenging of interstitials which normally segregate to the grain boundaries and (2) refining of the microstructure, making cleavage more difficult.
- b. The subsequent decrease in  $K_{Icd}$  for Ti addition >0.18 at.% is due to the increase in flow stress resulting from these additions and a slight decrease in fracture stress, which in turn leads to an earlier intersection of the flow curve with the cleavage fracture stress curve.
- c. The effects of the Ti additions and heat treat temperature on  $K_{Icd}$  is partly due to their influence on the amount, size and distribution of the precipitate which was observed at 550°C.

## References

1. J. A. Rinebolt and W. J. Harris, Jr., Trans., ASM (1951) 43 1175.
2. E. A. Steigerwald and C. Vishnevsky, : Literature Survey on the Influence of Alloy Elements on the Fracture Toughness of High Strength Steels, TRW, Inc. (AMMRC-CR-67-13(F) AD-665432). (1968).
3. W. P. Rees and B. E. Hopkins, J. Iron and Steel Inst. (1952) 172 403.
4. F. B. Pickering: The Effect of Composition and Microstructure on Ductility and Toughness. Symposium: Toward Improved Ductility and Toughness, Climax Molybdenum Development Co. (Japan)Ltd. (1971) p.9.
5. Walter R. Witzke and Joseph R. Stephens: Effect of Minor Reactive Metal Additions on Fracture Toughness of Iron-12 Percent Nickel Alloy at  $-196^{\circ}$  and  $25^{\circ}\text{C}$ , NASA TN D-8232, May 1976.
6. S. Jin, J. W. Morris, Jr. and V. F. Zackey: Advan. Cryog Eng., 19 (1974) p. 379.
7. F. W. Jones and W. I. Pumphrey., J. Iron Steel Inst. (1949) 163 121.
8. G. Sasaki, D. Eng. Thesis, University of California, Berkeley, Calif. July 1973.
9. S. Jim, J. W. Morris, Jr., and V. F. Zackey, Met. Trans. (1975) 6A 141.
10. P. W. Palmberg, J. Vacuum Sci. Technol., (1972) 9 160.
11. A. Gilbert and W. S. Owen, Acta Met. 10 45 (1962).
12. S. Floreen, Met. Reviews, (1968) p. 115.
13. S. M. Chilton and G. R. Speich, Met. Trans. 1 1019 (1970).
14. H. Conrad, "Effect of Interstitials on the Strength of Titanium", in preparation for publication in Prog. in Mat. Sci.

Table I. Chemical Composition of the Materials

Specimen Number	Interstitial Content								
	Fe		Ni		Ti		O	N	C
	At.%	Wt.%	At.%	Wt.%	At.%	Wt.%	PPM(WT.)		
C-974-T	88.10	87.60	11.90	12.40	0	0	160	41	26
D-367-T	87.67	87.15	12.15	12.70	0.18	0.15	61	12	18
D-27-T	87.33	86.65	12.20	12.75	0.47	0.40	68	13	25
D-141-T	86.81	86.40	12.20	12.76	0.99	0.84	63	28	36

Table II. Tensile Properties of Fe-12Ni-xTi Alloys Tested at 77K

NOMINAL COMPOSITION  (at%)	YIELD STRESS (0.2% STRAIN) $\sigma_{YS}$  (MPa)	TENSILE STRENGTH $\sigma_{UTS}$  (MPa)	FRACTURE STRESS $\sigma_F$  (MPa)	UNIFORM STRAIN $\epsilon_U$	TRUE FRACTURE STRAIN $\epsilon_F$	STRAIN HARDENING EXPONENT  n	AREA UNDER TRUE STRESS-STRAIN CURVE $W_F$  ( $10^6$ J/m <sup>3</sup> )
550°C 2 hrs, WQ							
Fe-12Ni	848.2	949.2	1068.7	0.0720	0.1861	0.0990	179.3
Fe-12Ni-0.18Ti	866.8	1050.3	1723.8	0.1365	0.7985	0.1250	1049.7
Fe-12Ni-0.47Ti	1032.3	1213.6	1532.1	0.0858	0.3980	0.0760	525.3
Fe-12Ni-0.99Ti	1283.0	1432.4	1688.6	0.0624	0.2826	0.0540	428.8
685°C 2 hrs, WQ							
Fe-12Ni	881.5	929.6	1100.4	0.0041	0.1717	0.0720	173.6
Fe-12Ni-0.18Ti	834.6	1018.9	2025.1	0.0765	0.9470	0.0750	1397.7
Fe-12Ni-0.47Ti	866.8	1055.5	1880.3	0.0403	0.7208	0.0347	996.5
Fe-12Ni-0.99Ti	872.6	1155.7	1912.7	0.0630	0.6717	0.0530	994.7
820°C 2 hrs, WQ							
Fe-12Ni	861.9	957.3	1300.4	0.0107	0.3387	0.0280	379.6
Fe-12Ni-0.18Ti	949.9	1026.6	2090.6	0.0656	0.9755	0.0616	1482.8
Fe-12Ni-0.47Ti	800.9	1003.2	1838.2	0.0509	0.7611	0.0420	1050.7
Fe-12Ni-0.99Ti	956.7	1180.5	1772.7	0.0472	0.5769	0.0370	835.2



TABLE III. Summary of SEM Observations on the Fracture Surface of the Tensile Specimens Tested at 77K

Specimen Number	Nominal Composition (at%)	Annealing Temperature (°C)	Morphology of Inclusions	Dimple Size (Microns)	Fracture Surface Characteristics
C974-T-1	Fe-12Ni	550	Spheroidal	2.54	60% cleavage fracture; 40% ductile fracture; dimple regions are inter-mixed with cleavage fracture regions; dimple size is not uniform.
C974-T-3	Fe-12Ni	685	Spheroidal	2.77	90% cleavage and inter-granular fracture; 10% ductile fracture
C974-T-5	Fe-12Ni	820	Spheroidal and Cubical	5.08	50% cleavage fracture; 50% ductile fracture; dimple size is not uniform
D367-T-2	Fe-12Ni-0.18Ti	550	Spheroidal and Cubical	2.89	100% ductile fracture; dimple size is not uniform
D367-T-4	Fe-12Ni-0.18Ti	685	Spheroidal and Rectangular	1.86	100% ductile fracture; dimple size is not uniform
D367-T-6	Fe-12Ni-0.18Ti	820	Spheroidal and Cubical	2.25	100% ductile fracture; uniform dimple size
D27-T-2	Fe-12Ni-0.47Ti	550	Spheroidal and Rectangular	2.95	15% cleavage fracture; 85% ductile fracture
D27-T-4	Fe-12Ni-0.47Ti	685	Spheroidal and Cubical	1.73	100% ductile fracture; dimple size is not uniform
D-27-T-6	Fe-12Ni-0.47Ti	820	Spheroidal, Hexagonal and Rectangular	2.37	5% cleavage fracture; 95% ductile fracture

TABLE III CONTINUED

D-141-T-2	Fe-12Ni-0.99Ti	550	Irregular Shape	2.60	20% cleavage fracture; 80% ductile fracture
D-141-T-4	Fe-12Ni-0.99Ti	685	Cubical and Rectangular	1.73	10% cleavage fracture; 90% ductile fracture; dimple size is irre- gular
D-141--6	Fe-12Ni-0.99Ti	820	Spheroidal	2.03	10% cleavage fracture; 90% ductile fracture

TABLE IV. Summary of SEM Observations on the Fracture Surface of the Fracture Toughness Specimens Tested at 77K

Specimen Number	Nominal Composition (at%)	Annealing Temperature (C°)	Morphology of Inclusions	Dimple Size (Microns)	Fracture Surface Characteristics
C974-B-1	Fe-12Ni	550	Spheroidal	3.54	80% cleavage fracture; 20% ductile fracture
C974-B-3	Fe-12Ni	685	Spheroidal	not measurable	98% cleavage and intergranular fracture; 2% ductile fracture
C974-B-5	Fe-12Ni	820	Spheroidal	not measurable	90% cleavage and intergranular fracture; 10% ductile fracture
C367-B-2	Fe-12Ni-0.18Ti	550	Spheroidal and Cubical	1.71	90% cleavage fracture; 10% ductile fracture
C367-B-4	Fe-12Ni-0.18Ti	685	Spheroidal	6.49	50% cleavage fracture; 50% ductile fracture
C367-B-6	Fe-12Ni-0.18Ti	820	Spheroidal and Cubical	7.68	50% cleavage fracture; 50% ductile fracture
D27-B-2	Fe-12Ni-0.47Ti	550	Rectangular	not measurable	98% cleavage fracture; 2% ductile fracture
D27-B-6	Fe-12Ni-0.47Ti	820	Cubical and Rectangular Shape	8.82	50% cleavage fracture; 50% ductile fracture
D141-B-2	Fe-12Ni-0.99Ti	550	Irregular Shape	not measurable	100% cleavage fracture
D141-B-4	Fe-12Ni-0.99Ti	685	Spheroidal and Rectangular	3.45	80% cleavage fracture; 20% ductile fracture
D141-B-6	Fe-12Ni-0.99Ti	820	Small Spheroidal	11.06	80% cleavage fracture; 20% ductile fracture

TABLE V. Relative Affinities of the Elements in Ti-12Ni-xTi Alloys  
Determined from Auger Mappings

Nominal Composition (at%)	Degree of Association			Moderate Dissociation	Relatively Uniform Distribution	Non Uniform Distribution Assoc. or Dissoc.
	Strong	Moderate	Weak			
550°C 2 Hours, W. Q.						
Fe-12Ni	Ni, Fe	-----	-----	C (Fe, Ni)	O, N	-----
Fe-12Ni-0.18Ti	Ni, Fe	-----	Ni, Ti, C, O	-----	N	-----
Fe-12Ni-0.47Ti	Ni, Fe	-----	Ti, C, O	-----	O	-----
685°C 2 Hours, W. Q.						
Fe-12Ni	Ni, Fe	-----	-----	C (Fe, Ni)	N	C, O
Fe-12Ni-0.18Ti	Ni, Fe	-----	-----	Ti, C, N, O	---	-----
Fe-12Ni-0.99Ti	Ni, Fe	-----	-----	Ti, C, N, O	---	-----
820°C 2 Hours, W. Q.						
Fe-12Ni-0.18Ti	Ni, Fe	Ti, N	-----	-----	---	O, C
Fe-12Ni-0.47Ti	Ni, Fe	Ti, N	-----	C (Fe, Ni)	---	O
Fe-12Ni-0.99Ti	Ni, Fe	Ti, N	O, C	-----	---	-----

TABLE VI. Summary of Bond Energies, e, for TiO, TiN and TiC Compounds Determined by Various Methods and the Activation Energy for Diffusion,  $Q_D$ , for Dilute Solutions of the Interstitial Solutes in Ti. All Energies in eV. (From Conrad (14)).

System	Bond Energy e Derived From			Activation Energy for Diffusion
	$\Delta H^\theta$	$\Delta H_s$	$\gamma_s$	$Q_D$
Ti-O	2.13	1.17	1.17	2.18
Ti-N	2.22	1.70	1.42	2.50
Ti-C	2.18	1.25	1.13	2.00

Notes:

- $\Delta H^\theta$  = Heat of formation  
 $\Delta H_s$  = Heat of sublimation  
 $\gamma_s$  = Surface energy

## List of Illustrations

- Fig. 1. Phase transformation diagram for heating and cooling of Fe-Ni alloys (Ref 8 ).
- Fig. 2. Schematic of vacuum chamber and controlling electronics for Varian Auger electron spectrometer.
- Fig. 3. Auger spectra for C and O from fracture surface of Fe-12Ni-0.18Ti alloy heat treated at 685°C and tested at 77K.
- Fig. 4. True stress-true strain curves of Fe-12Ni - xTi alloys heat treated at 550, 685, and 820°C.
- Fig. 5. Tensile properties at 77K of Fe-12Ni -xTi alloys versus Ti content as a function of heat treatment temperature.
- Fig. 6.  $K_{Icd}$  and work-to fracture in tension  $W_F$  at 77K versus Ti content as a function of heat treatment temperature.
- Fig. 7.  $K_{Icd}$  versus  $W_F$  at 77K for Fe-12Ni - xTi alloys heat treated at 550, 685, and 820°C.
- Fig. 8. SEM fractographs of Fe-12Ni alloy heat treated at 550°C and tested at 77K.
- Fig. 9. SEM fractographs of Fe-12Ni-0.18Ti alloy heat treated at 550°C and tested at 77K.
- Fig. 10 SEM fractographs of Fe-12Ni-0.47Ti alloy heat treated at 550°C and tested at 77K.
- Fig. 11 SEM fractographs of Fe-12Ni-0.99Ti alloy heat treated at 550°C and tested at 77K.
- Fig. 12 SEM fractographs of Fe-12Ni alloy heat treated at 685°C and tested at 77K.
- Fig. 13 SEM fractographs of Fe-12Ni-0.18Ti alloy heat treated at 685°C and tested at 77K.

- Fig. 14. SEM fractograph of Fe-12Ni-0.47Ti alloy heat treated at 685°C and tested at 77K.
- Fig. 15. SEM fractographs of Fe-12Ni-0.99Ti alloy heat treated at 685°C and tested at 77K.
- Fig. 16. SEM fractographs of Fe-12Ni alloy heat treated at 820°C and tested at 77K.
- Fig. 17. SEM fractographs of Fe-12Ni-0.18Ti alloy heat treated at 820°C and tested at 77K.
- Fig. 18. SEM fractographs of Fe-12Ni-0.47Ti alloy heat treated at 820°C and tested at 77K.
- Fig. 19. SEM fractographs of Fe-12Ni-0.99Ti alloy heat treated at 820°C and tested at 77K.
- Fig. 20.  $K_{Icd}$  versus the fraction of ductile fracture at 77K for Fe-12Ni - xTi alloys heat treated at 550, 685, and 820°C.
- Fig. 21. Optical microstructure of Fe-12Ni and Fe-12Ni-0.18Ti specimens heat treated at 550°C.
- Fig. 22. Optical microstructure Fe-12Ni-0.47Ti and Fe-12Ni-0.99Ti specimens heat treated at 550°C.
- Fig. 23. Optical microstructure of Fe-12Ni and Fe-12Ni-0.18Ti specimens heat treated at 685°C.
- Fig. 24. Optical microstructure of Fe-12Ni-0.99Ti specimens heat treated at 685°C.
- Fig. 25. Optical microstructure of Fe-12Ni and Fe-12Ni-0.18Ti specimens heat treated at 820°C.
- Fig. 26. Optical microstructure of Fe-12Ni-0.47Ti and Fe-12Ni-0.99Ti specimens heat treated at 820°C.
- Fig. 27. TEM microstructure of Fe-12Ni and Fe-12Ni-0.18Ti alloys heat treated at 550°C.

- Fig. 28. TEM microstructure of Fe-12Ni and Fe-12Ni-0.18Ti alloys heat treated at 685°C.
- Fig. 29. TEM microstructure of Fe-12Ni and Fe-12Ni-0.18Ti alloys heat treated at 820°C.
- Fig. 30. Auger Spectrum mapping for Ni and Fe of the fracture surface of a notch bend specimen of Fe-12Ni alloy heat treated at 550°C and tested at 77K.
- Fig. 31. Auger Spectrum mapping for O and C of the fracture surface of a notch bend specimen of Fe-12Ni alloy heat treated at 550°C and tested at 77K.
- Fig. 32. Auger Spectrum mapping for N of the fracture surface of a notch bend specimen of Fe-12Ni alloy heat treated at 550°C and tested at 77K.
- Fig. 33. Auger Spectrum mappings for Ni and O of the fracture surface of a notch bend specimen of Fe-12Ni-0.18Ti alloy annealed at 550°C and tested at 77K.
- Fig. 34. Auger Spectrum mappings for Ti and C of the fracture surface of a notch bend specimen of Fe-12Ni-0.18Ti alloy annealed at 550°C and tested at 77K.
- Fig. 35. Auger Spectrum mapping for Ni and Fe of the fracture surface of a notch bend specimen of Fe-12Ni-0.47Ti alloy heat treated at 550°C and tested at 77K.
- Fig. 36. Auger Spectrum mapping for Ti and C of the fracture surface of a notch bend specimen of Fe-12Ni-0.47Ti alloy heat treated at 550°C and tested at 77K.
- Fig. 37. Auger Spectrum mapping for N and O of the fracture surface of a notch bend specimen of Fe-12Ni-0.47Ti alloy heat treated at 550°C and tested at 77K.
- Fig. 38. Auger Spectrum mapping for Ni and Fe of the fracture surface of a notch bend specimen of Fe-12Ni alloy heat treated at 685°C and tested at 77K.
- Fig. 39. Auger Spectrum mapping for O and C of the fracture surface of a notch bend specimen of Fe-12Ni alloy heat treated at 685°C and tested at 77K.
- Fig. 40. Auger Spectrum mapping for N of the fracture surface of a notch bend specimen of Fe-12Ni alloy heat treated at 685°C and tested at 77K.



- Fig. 41. Auger Spectrum mapping for Ni and Fe of the fracture surface of a notch bend specimen of Fe-12Ni-0.18Ti alloy heat treated at 685°C and tested at 77K.
- Fig. 42. Auger Spectrum mapping for Ti and C of the fracture surface of a notch bend specimen of Fe-12Ni-0.18Ti alloy heat treated at 685°C and tested at 77K.
- Fig. 43. Auger Spectrum mapping for N and O of the fracture surface of a notch bend specimen of Fe-12Ni-0.18Ti alloy heat treated at 685°C and tested at 77K.
- Fig. 44. Auger Spectrum mapping for Ni and Fe of the fracture surface of a notch bend specimen of Fe-12Ni-0.99Ti alloy heat treated at 685°C and tested at 77K.
- Fig. 45. Auger Spectrum mapping for Ti and C of the fracture surface of a notch bend specimen of Fe-12Ni-0.99Ti alloy heat treated at 685°C and tested at 77K.
- Fig. 46. Auger Spectrum mapping for N and O of the fracture surface of a notch bend specimen of Fe-12-Ni-0.99Ti alloy heat treated at 685°C and tested at 77K.
- Fig. 47. Auger Spectrum mapping for Ni and Fe of the fracture surface of a notch bend specimen of Fe-12Ni-0.18Ti alloy heat treated at 820°C and tested at 77K.
- Fig. 48. Auger Spectrum mapping for Ti and C of the fracture surface of a notch bend specimen of Fe-12Ni-0.18Ti alloy heat treated at 820°C and tested at 77K.
- Fig. 49. Auger Spectrum mapping for N and O of the fracture surface of a notch bend specimen of Fe-12Ni-0.18Ti alloy heat treated at 820°C and tested at 77K.

- Fig. 50. Auger Spectrum mapping for Ni and Fe of the fracture surface of a notch bend specimen of Fe-12Ni-0.47Ti alloy heat-treated at 820°C and tested at 77K.
- Fig. 51. Auger Spectrum mapping for Ti and C of the fracture surface of a notch bend specimen of Fe-12Ni-0.47Ti alloy heat treated at 820°C and tested at 77K.
- Fig. 52. Auger Spectrum mapping for N and O of the fracture surface of a notch bend specimen of Fe-12Ni-0.47Ti alloy heat treated at 820°C and tested at 77K.
- Fig. 53. Auger Spectrum mapping for Ni and Fe of the fracture surface of a notch bend specimen of Fe-12Ni-0.99Ti alloy heat treated at 820°C and tested at 77K.
- Fig. 54. Auger Spectrum mapping for Ti and C of the fracture surface of a notch bend specimen of Fe-12Ni-0.99Ti alloy heat treated at 820°C and tested at 77K.
- Fig. 55. Auger Spectrum mapping for N and O of the fracture surface of a notch bend specimen of Fe-12Ni-0.99Ti alloy heat treated at 820°C and tested at 77K.

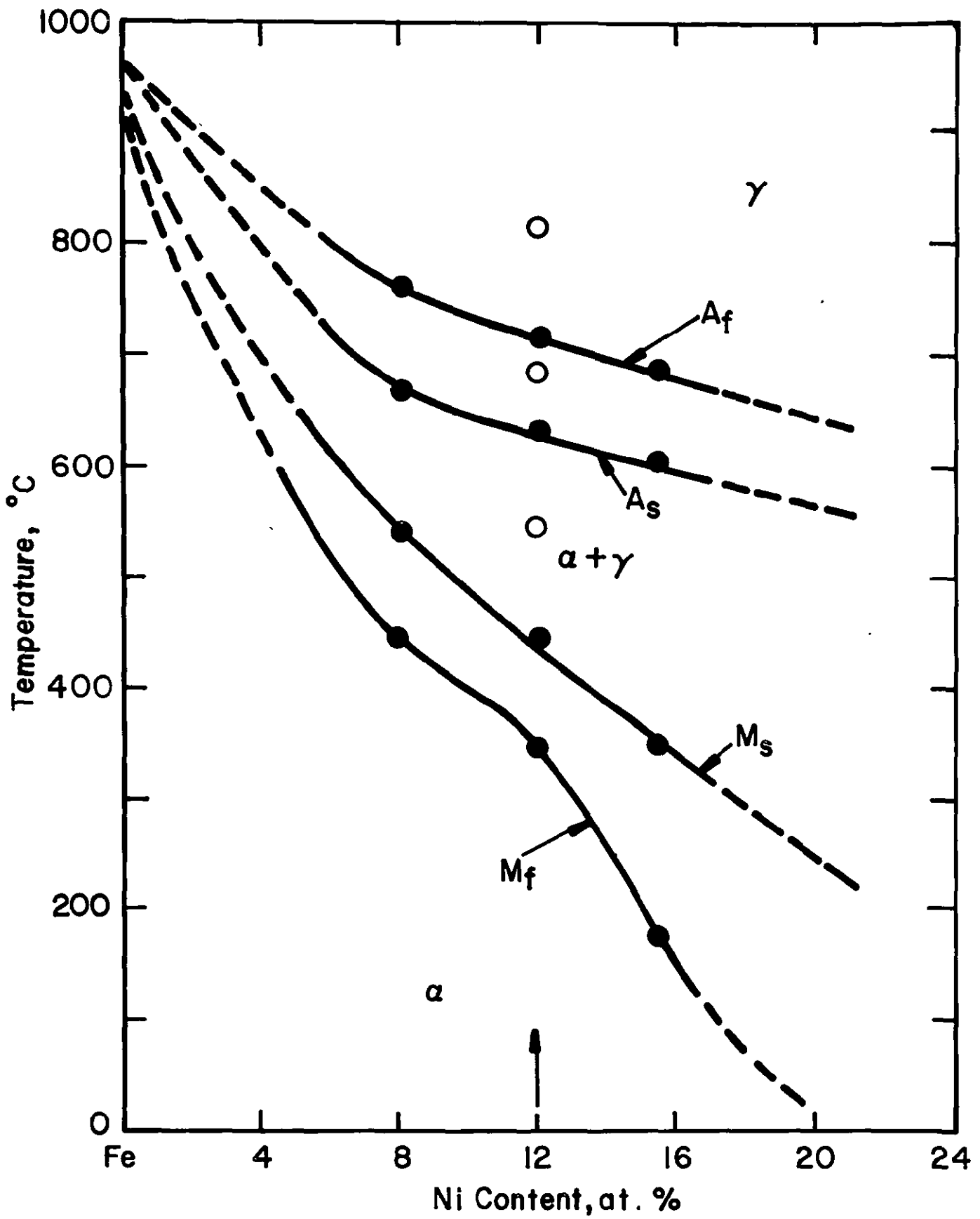


Fig. 1. Phase transformation diagram for heating and cooling of Fe-Ni alloys (Ref 8).

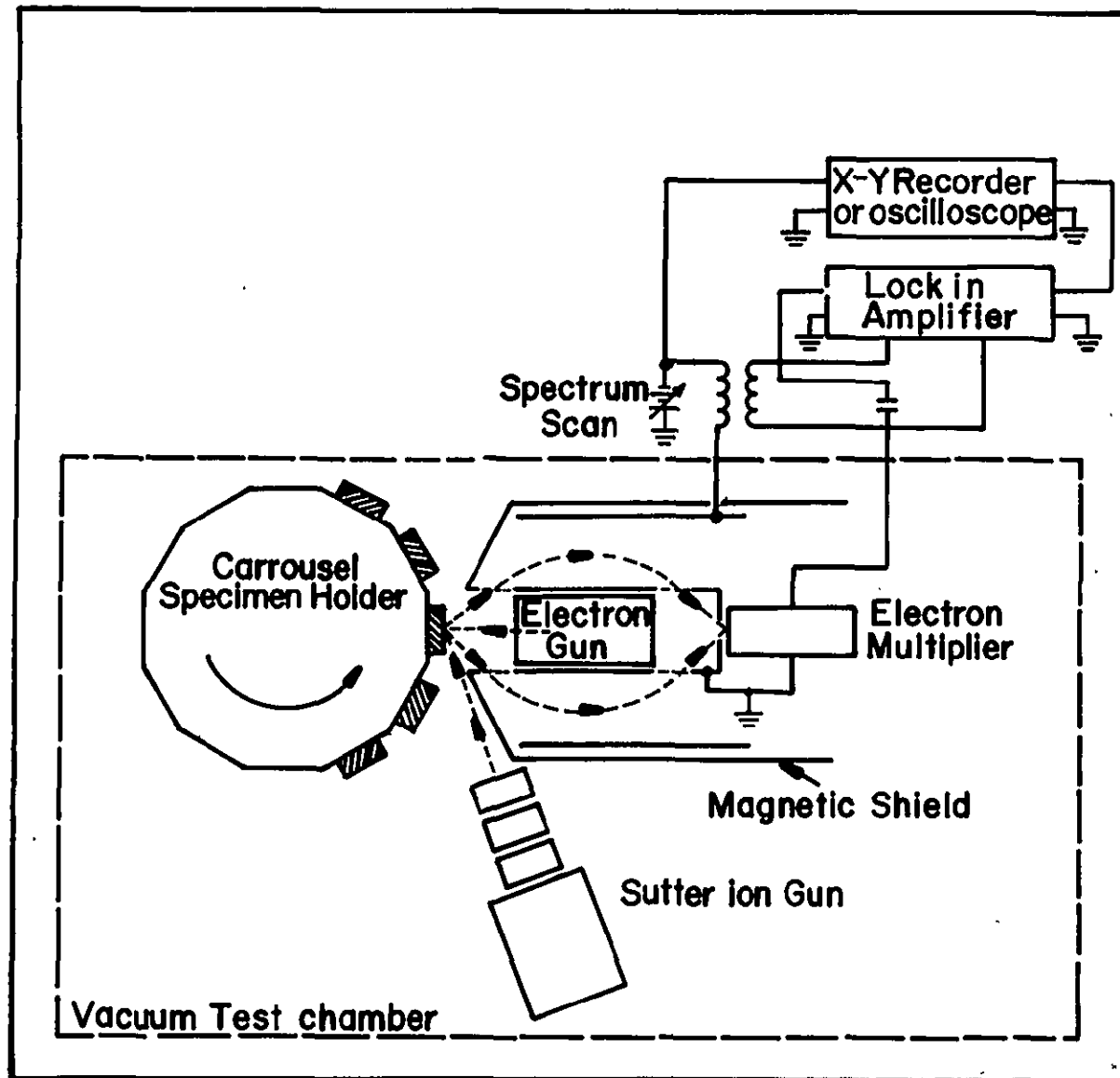


Fig. 2. Schematic of vacuum chamber and controlling electronics for Varian Auger electron spectrometer.

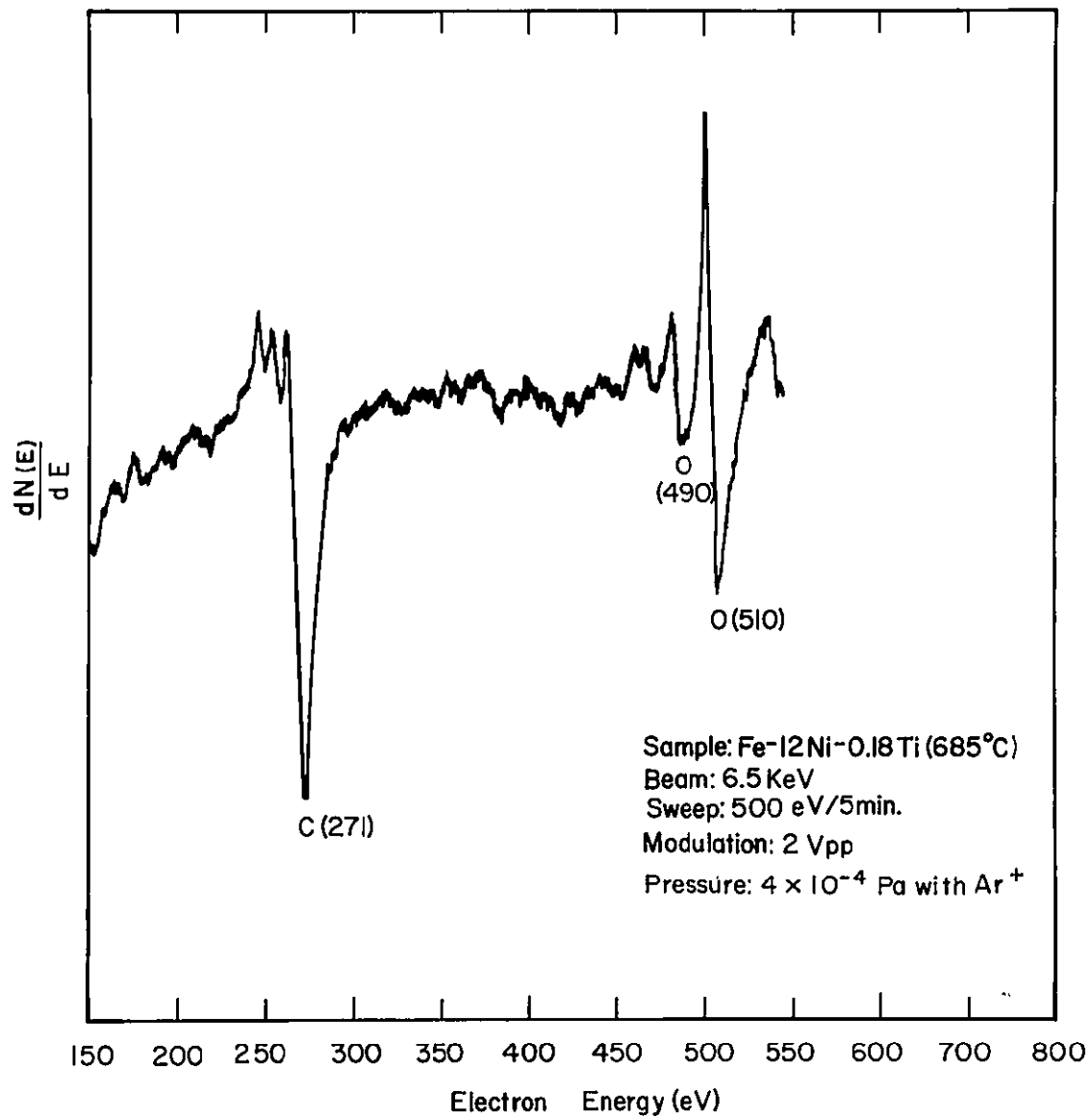


Fig. 3. Auger spectra for C and O from fracture surface of Fe-12Ni-0.18Ti alloy heat treated at 685°C and tested at 77K.

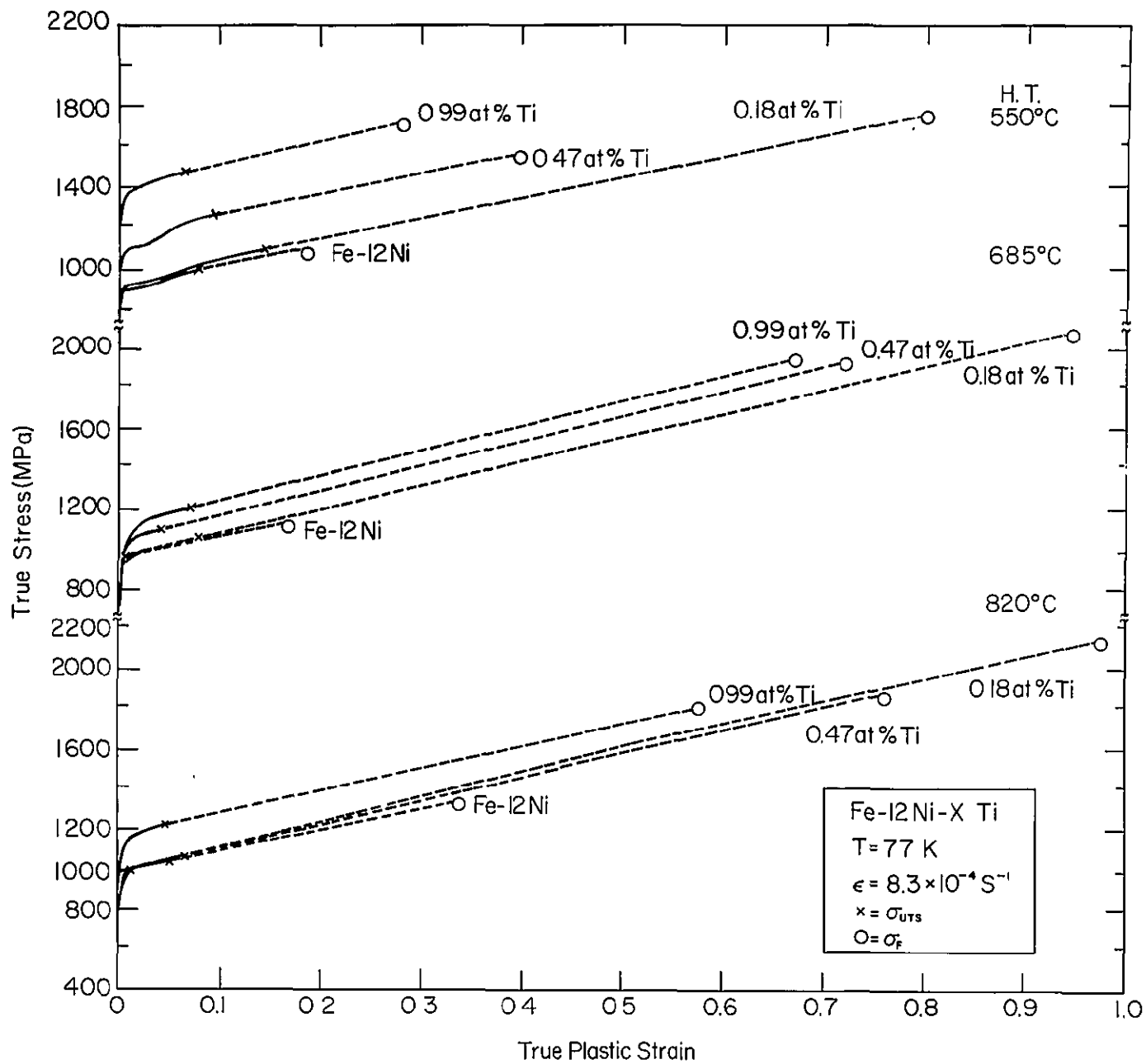


Fig. 4. True stress-true strain curves of Fe-12Ni - xTi alloys heat treated at 550, 685, and 820°C.

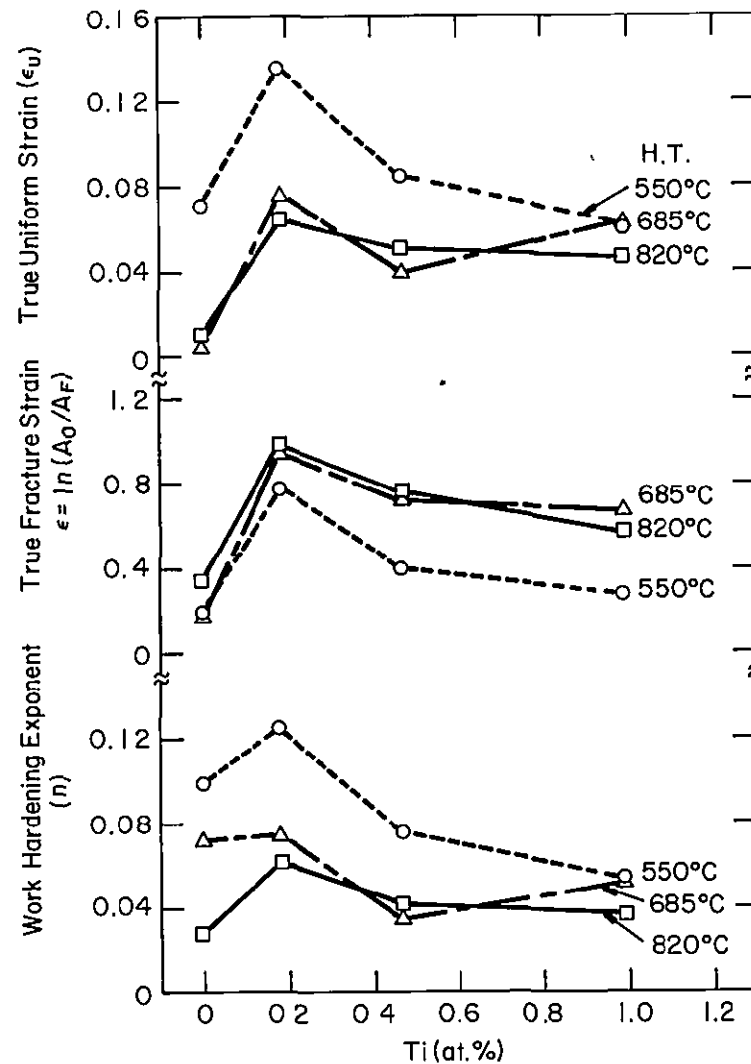
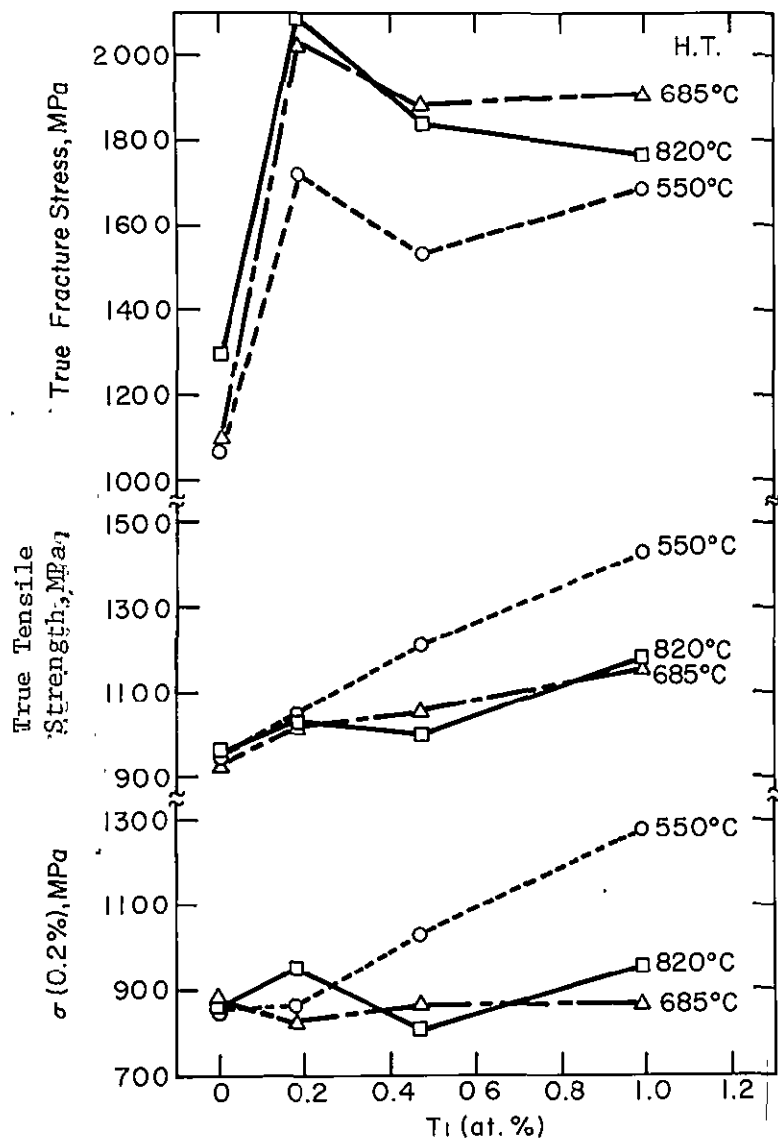


Fig. 5. Tensile properties at 77K of Fe-12Ni-xTi alloys versus Ti content as a function of heat treatment temperature.

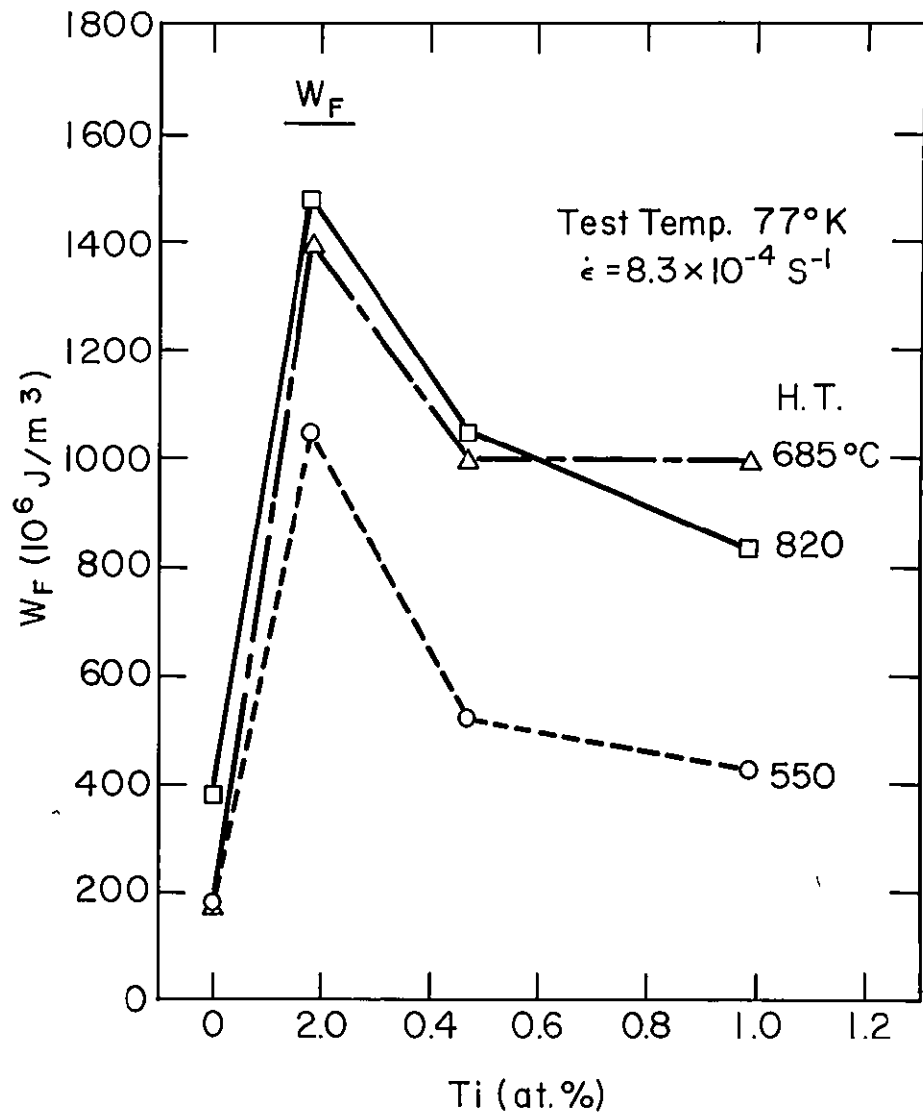
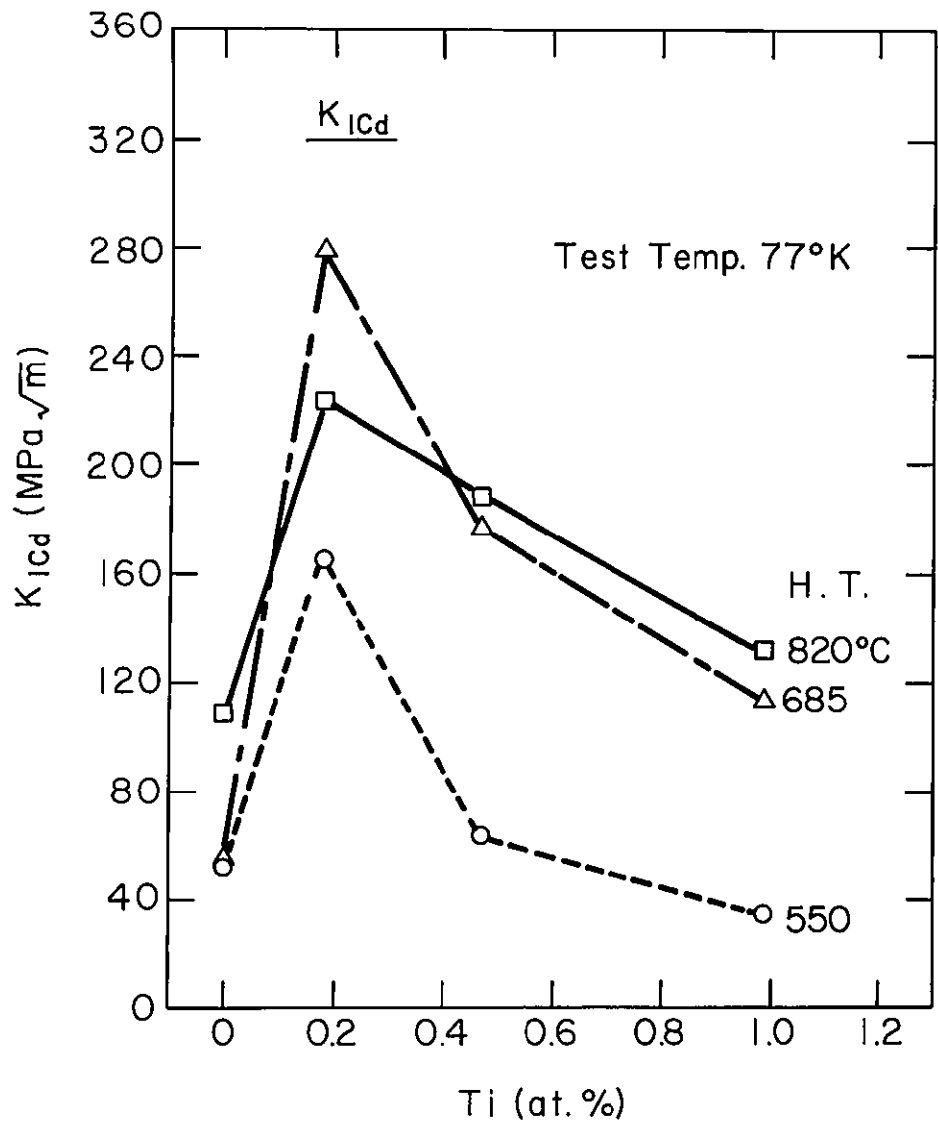


Fig. 6.  $K_{Icd}$  and work-to fracture in tension  $W_F$  at 77K versus Ti content as a function of heat treatment temperature.



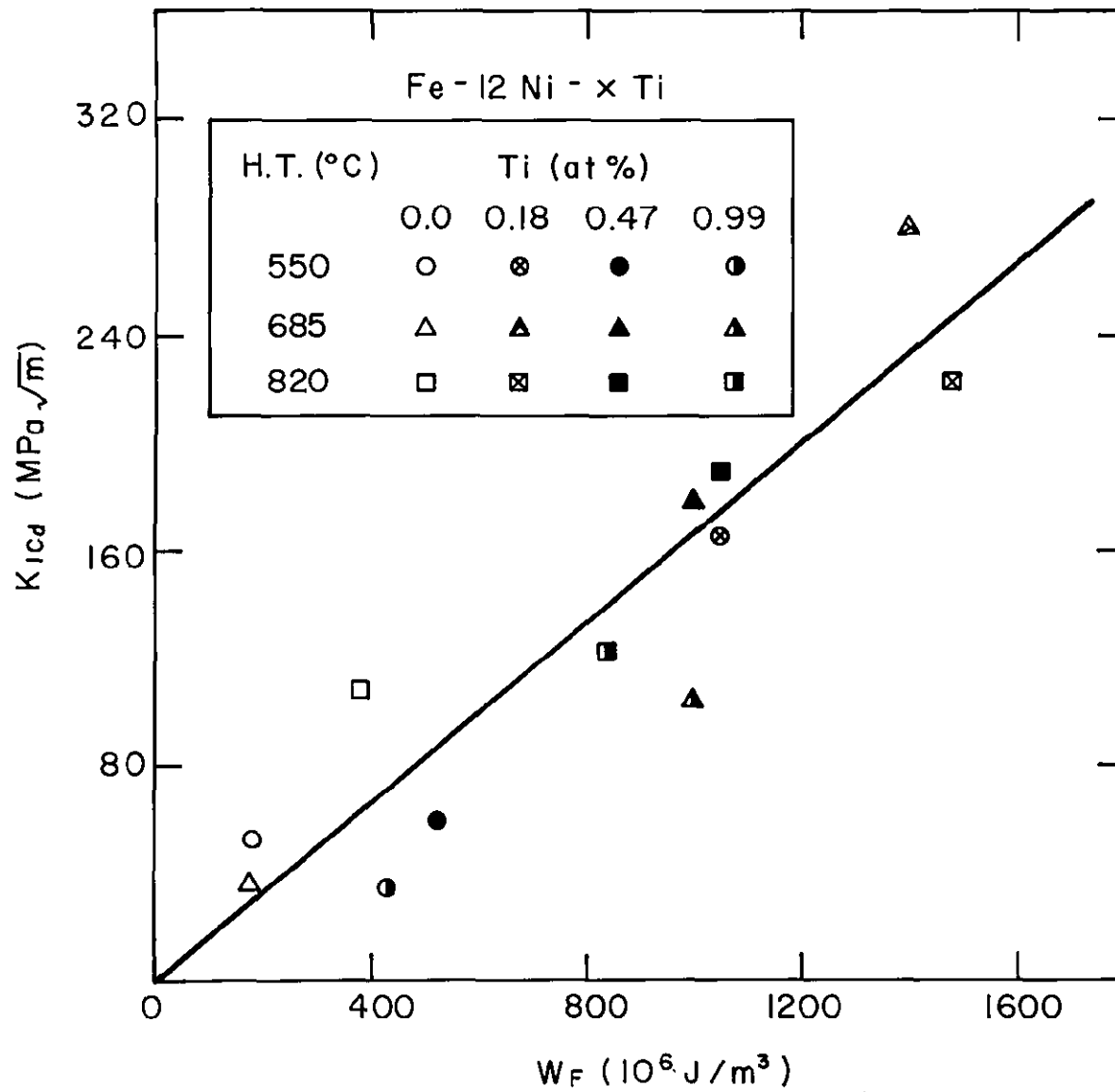
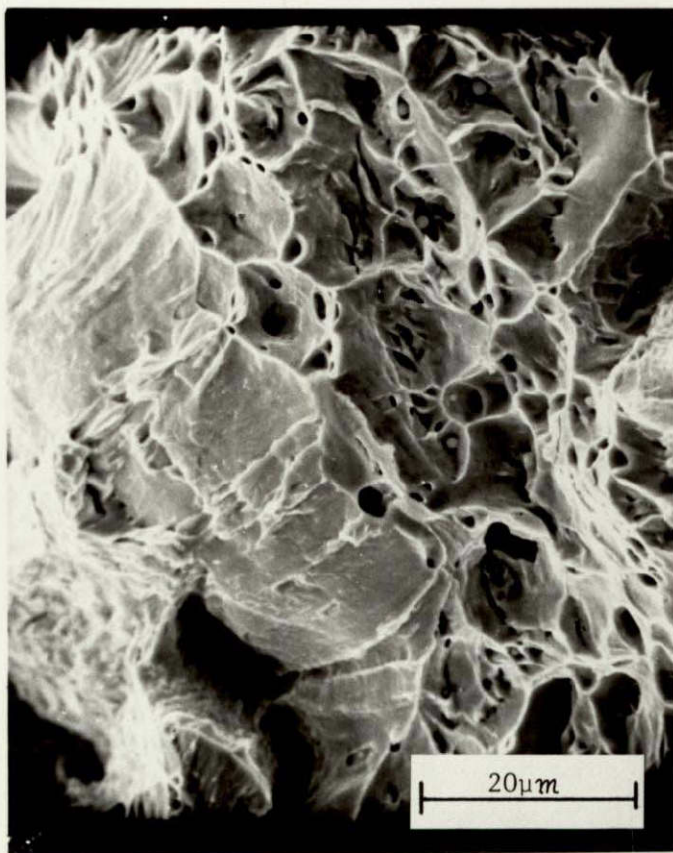
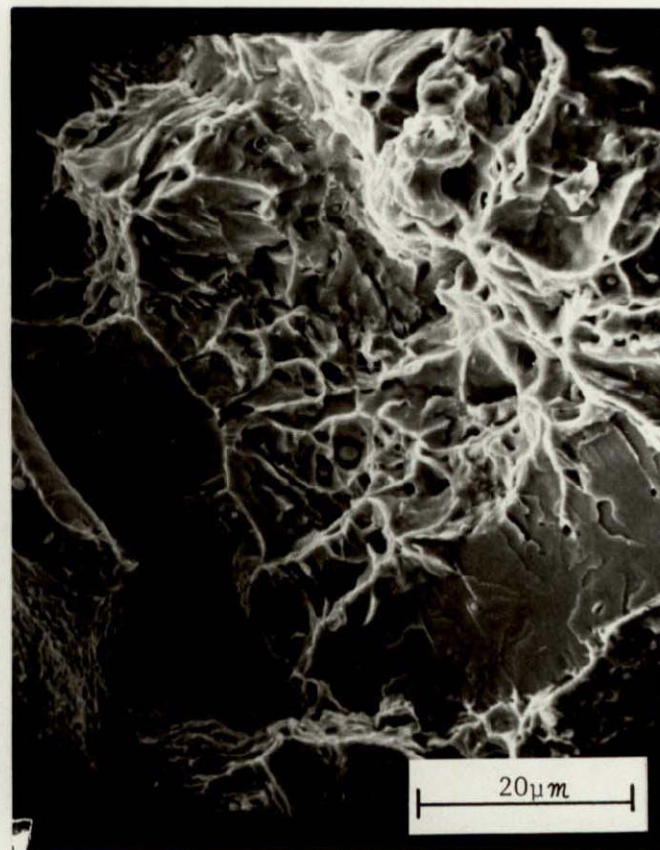


Fig. 7.  $K_{Icd}$  versus  $W_F$  at 77K for Fe-12Ni - xTi alloys heat treated at 550, 685, and 820°C.

ORIGINAL PAGE IS  
OF POOR QUALITY



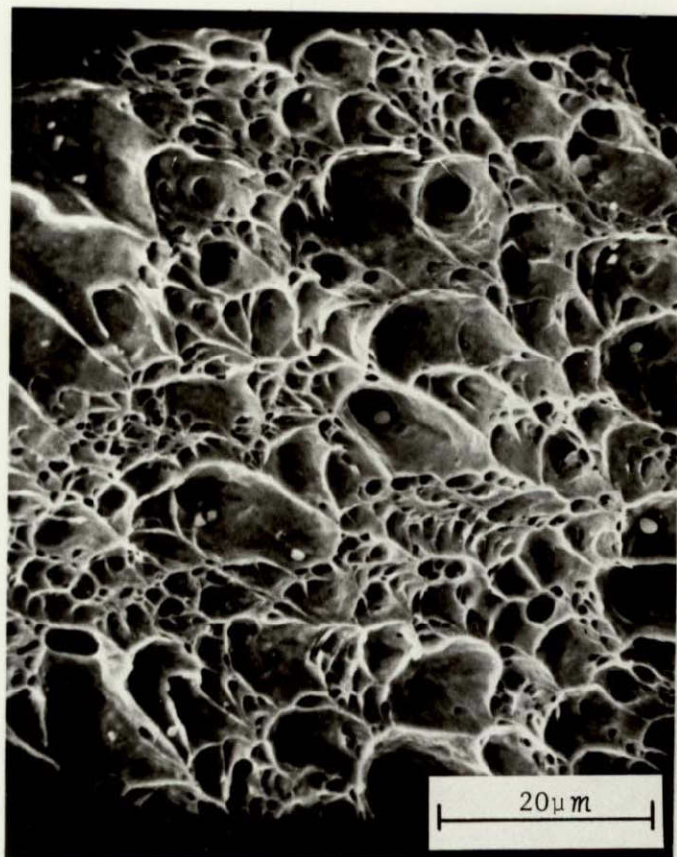
(a) Tensile Specimen



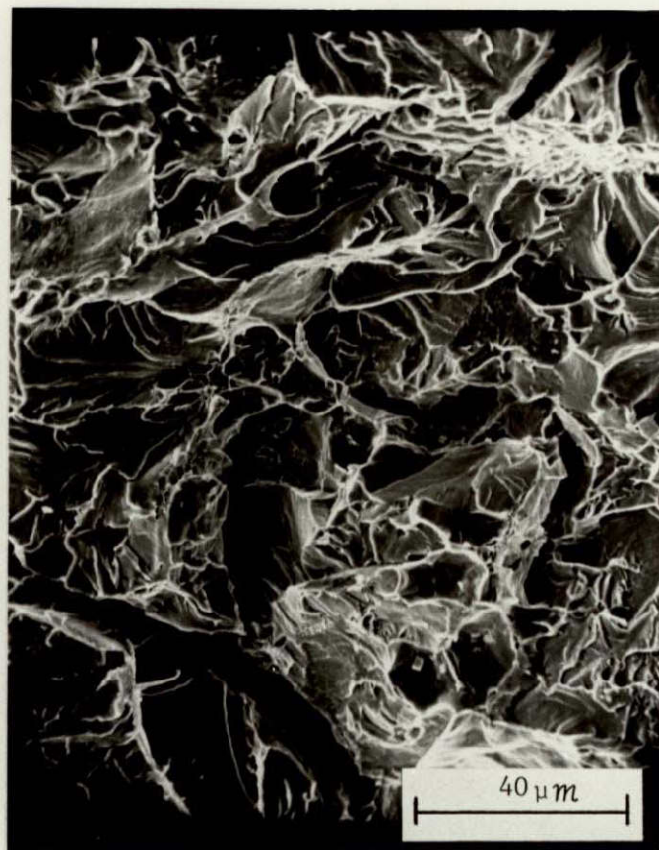
(b) Notch Bend Specimen

Figure 8 SEM fractographs of Fe-12Ni alloy heat-treated at 550°C and tested at 77K

ORIGINAL PAGE IS  
OF POOR QUALITY

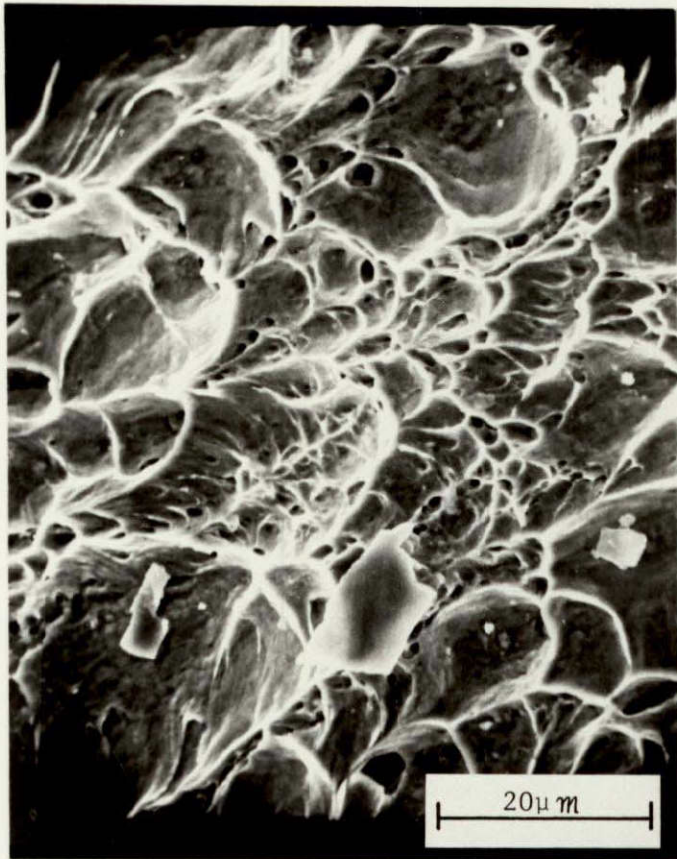


(a) Tensile Specimen

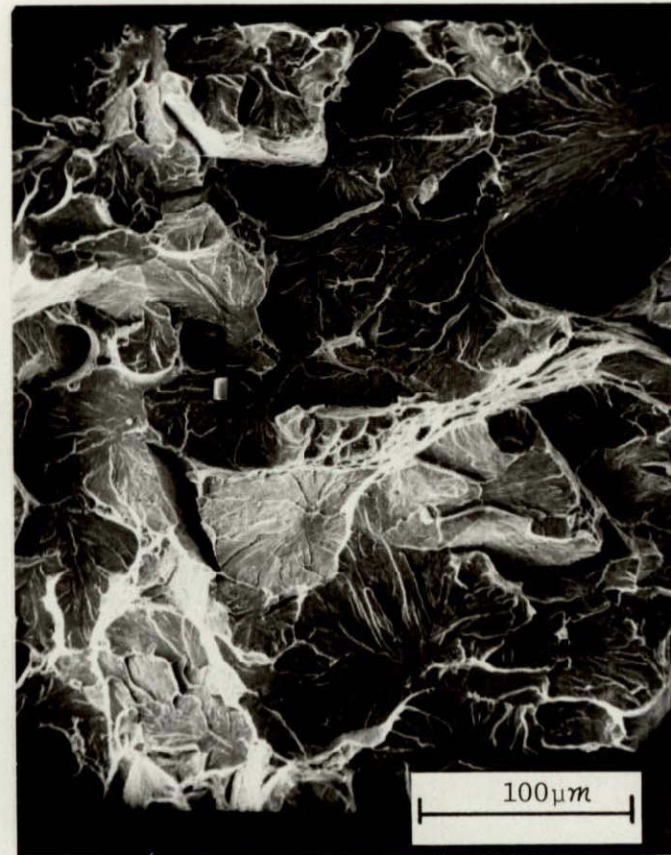


(b) Notch Bend Specimen

Figure 9 SEM fractographs of Fe-12Ni-0.18Ti alloy heat treated at 550°C and tested at 77K.



(a) Tensile Specimen



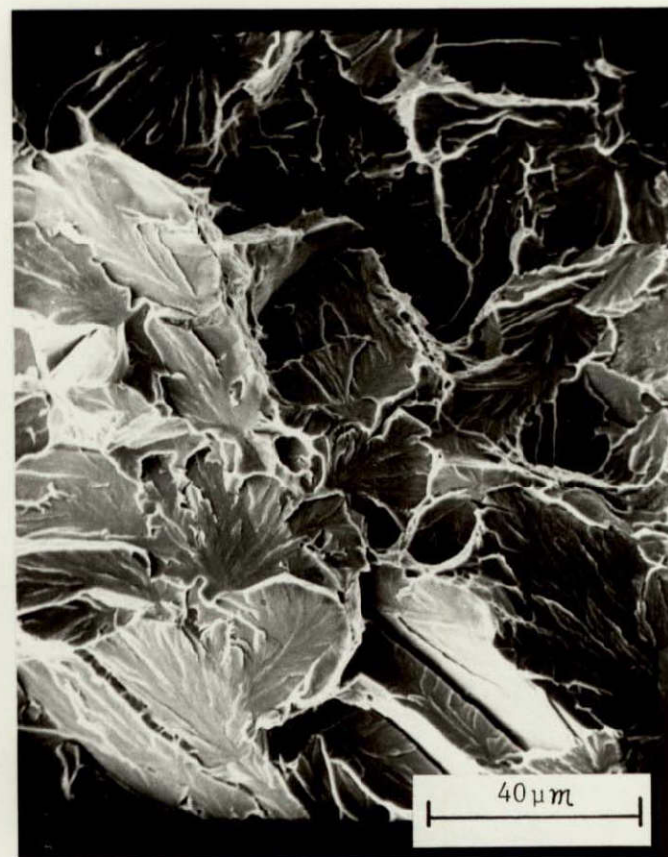
(b) Notch Bend Specimen

Figure 10 SEM fractographs of Fe-12Ni-0.47Ti alloy heat treated at 550°C and tested at 77K.

ORIGINAL PAGE IS  
OF POOR QUALITY



(a) Tensile Specimen



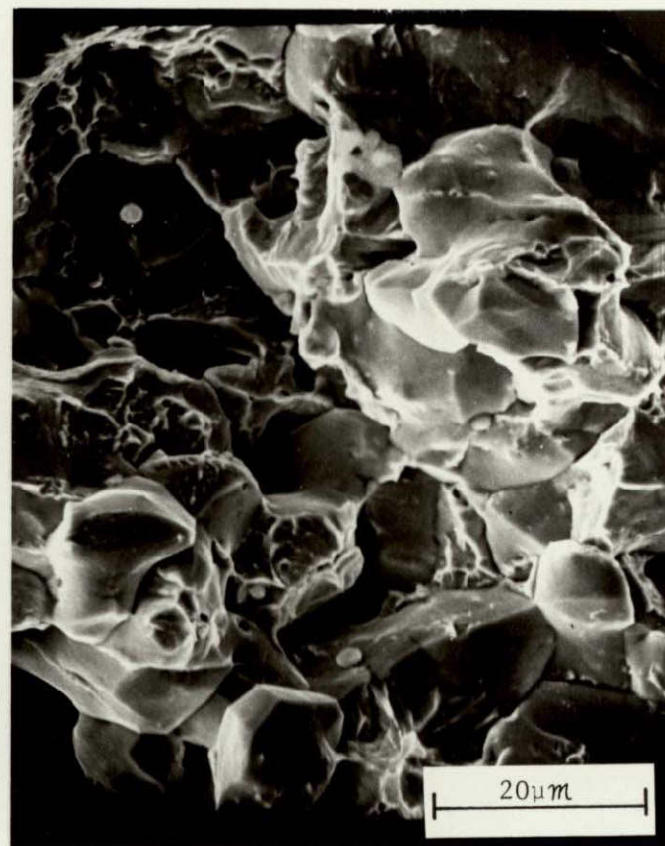
(b) Notch Bend Specimen

Figure 11 SEM fractographs of Fe-12Ni-0.99Ti alloy heat treated at 550°C and tested at 77K.

ORIGINAL PAGE IS  
OF POOR QUALITY

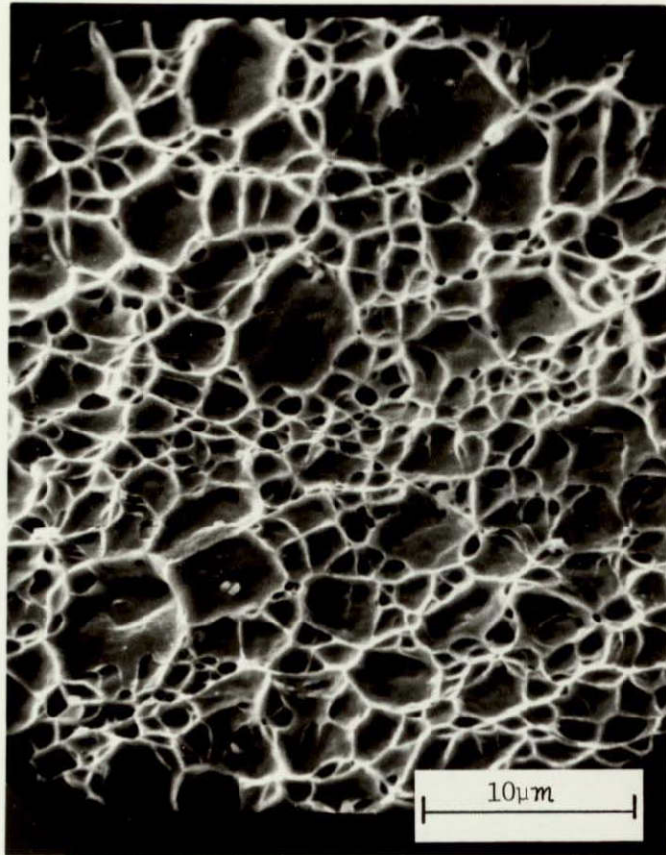


(a) Tensile Specimen

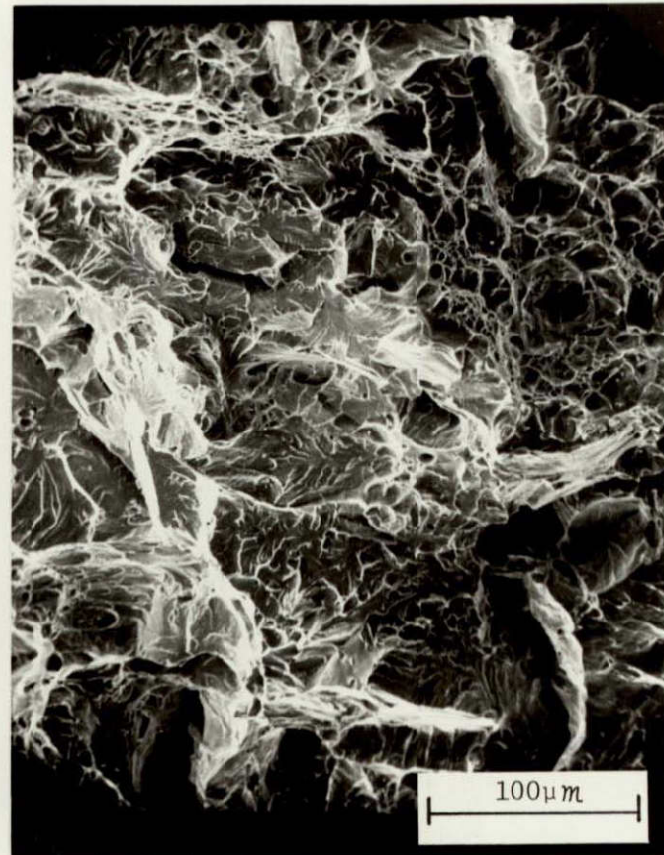


(b) Notch Bend Specimen

Figure 12 SEM fractographs of Fe-12Ni alloy heat treated at 685°C and tested at 77K.



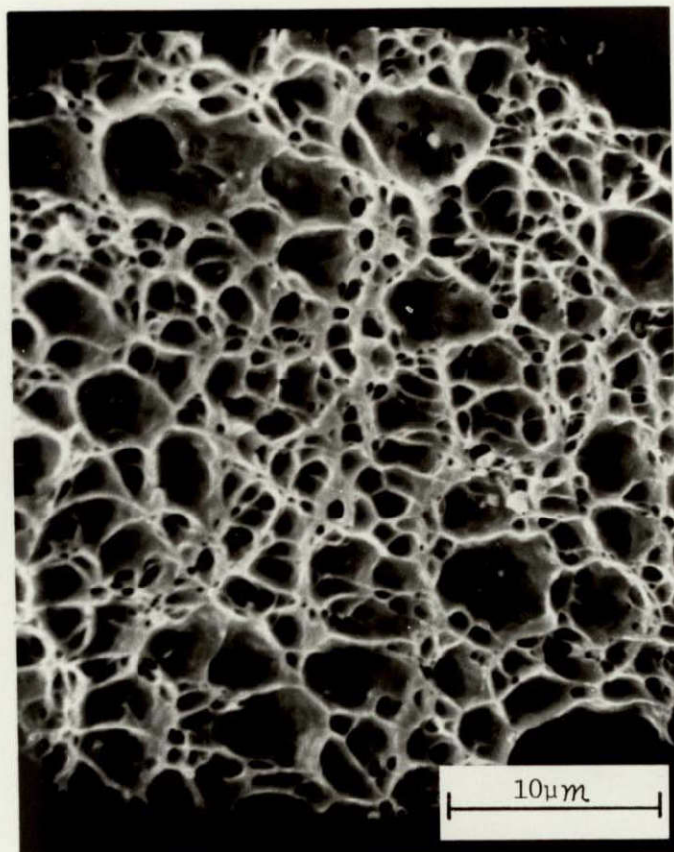
(a) Tensile Specimen



(b) Notch Bend Specimen

Figure 13 SEM fractographs of Fe-12Ni-0.18Ti alloy heat treated at 685°C and tested at 77K.

ORIGINAL PAGE IS  
OF POOR QUALITY

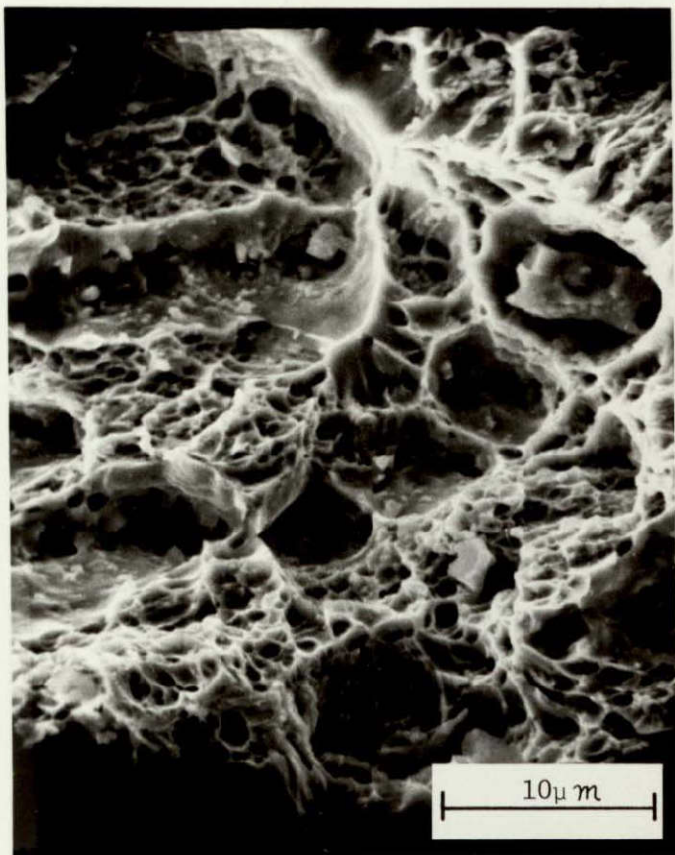


Tensile Specimen

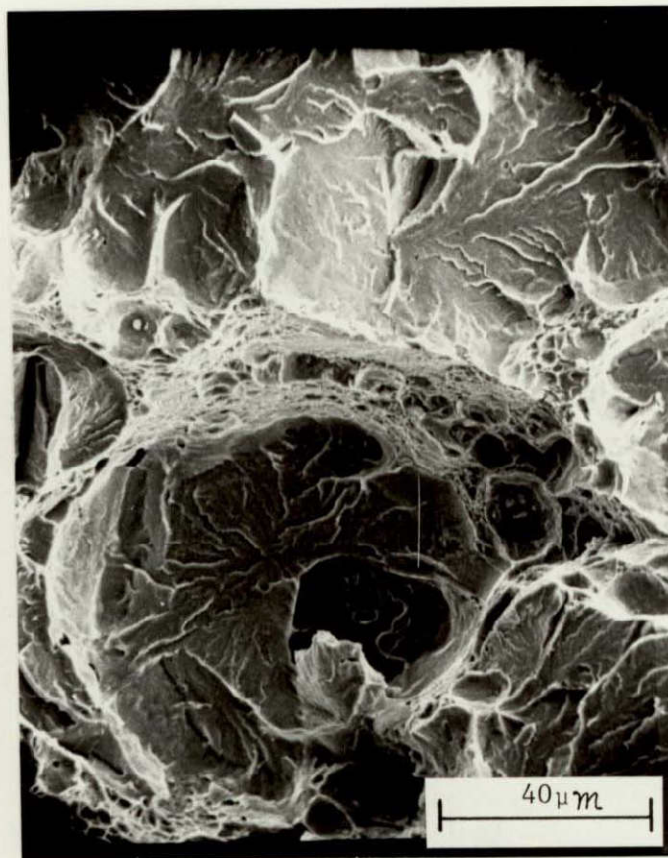
Figure 14 SEM fractograph of Fe-12Ni-0.47Ti alloy heat treated at 685°C and tested at 77K.

ORIGINAL PAGE IS  
OF POOR QUALITY



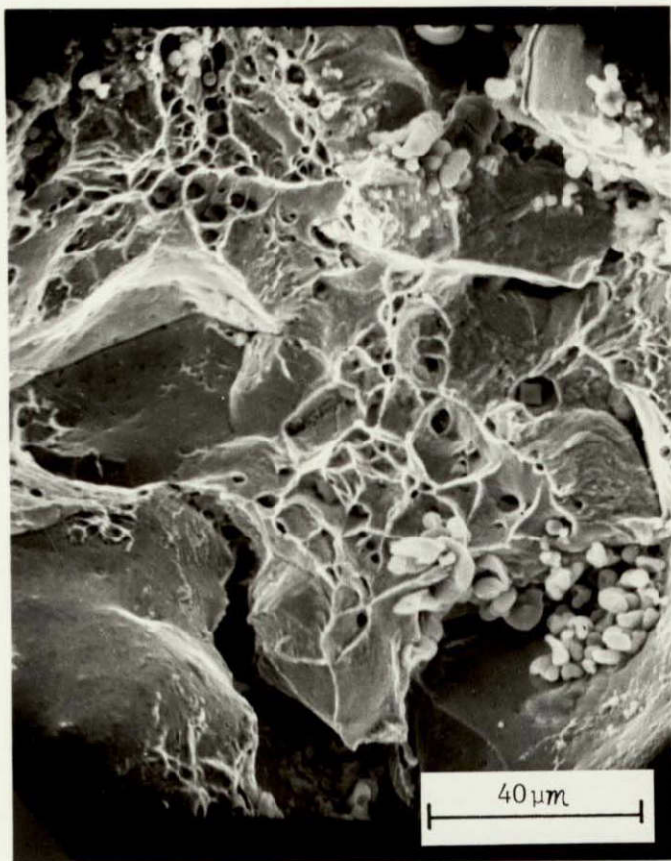


(a) Tensile Specimen

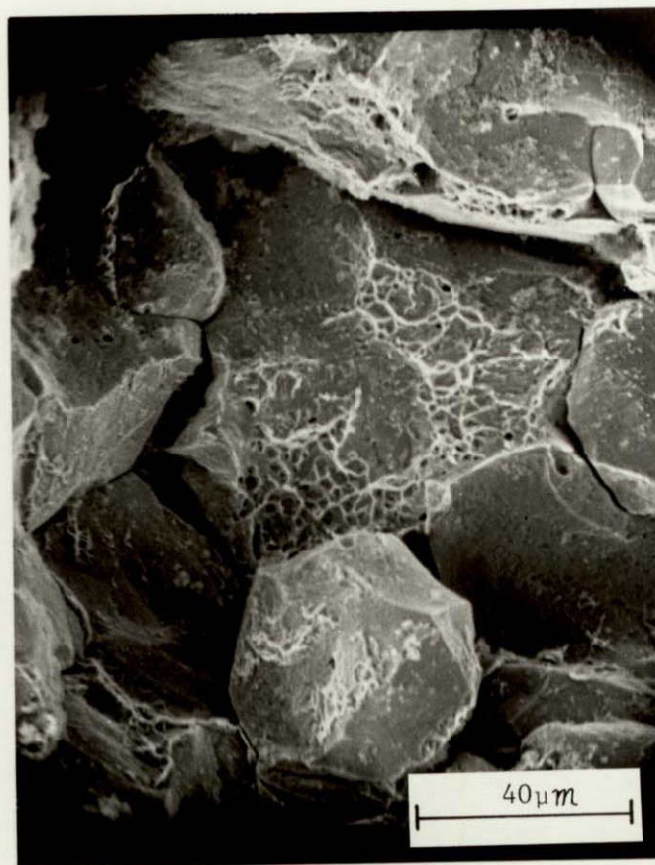


(b) Notch Bend Specimen

Figure 15 SEM fractographs of Fe-12Ni-0.99Ti alloy heat treated at 685°C and tested at 77K.



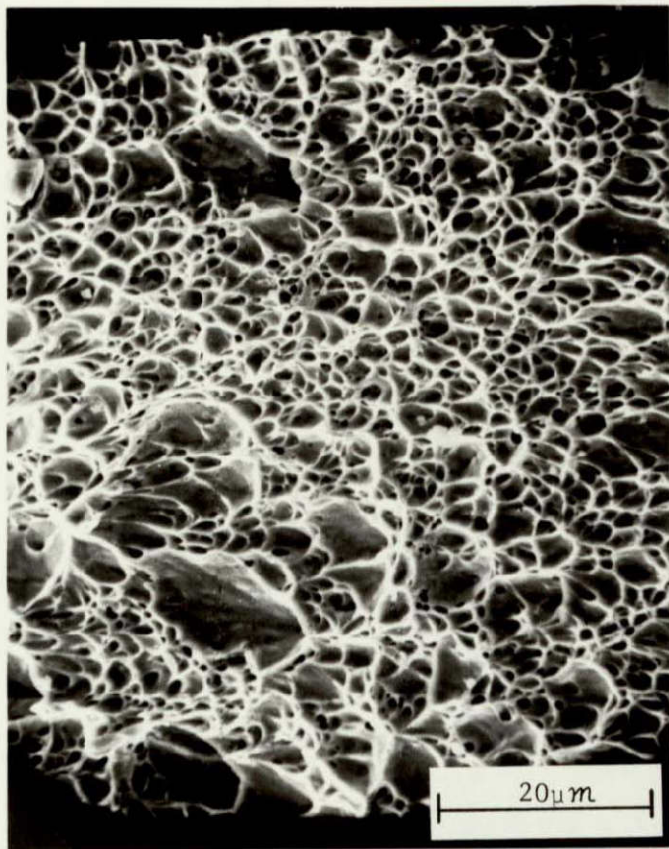
(a) Tensile Specimen



(b) Notch Bend Specimen

Figure 16 SEM fractographs of Fe-12Ni alloy heat treated at 820°C and tested at 77K.

ORIGINAL PAGE IS  
OF POOR QUALITY

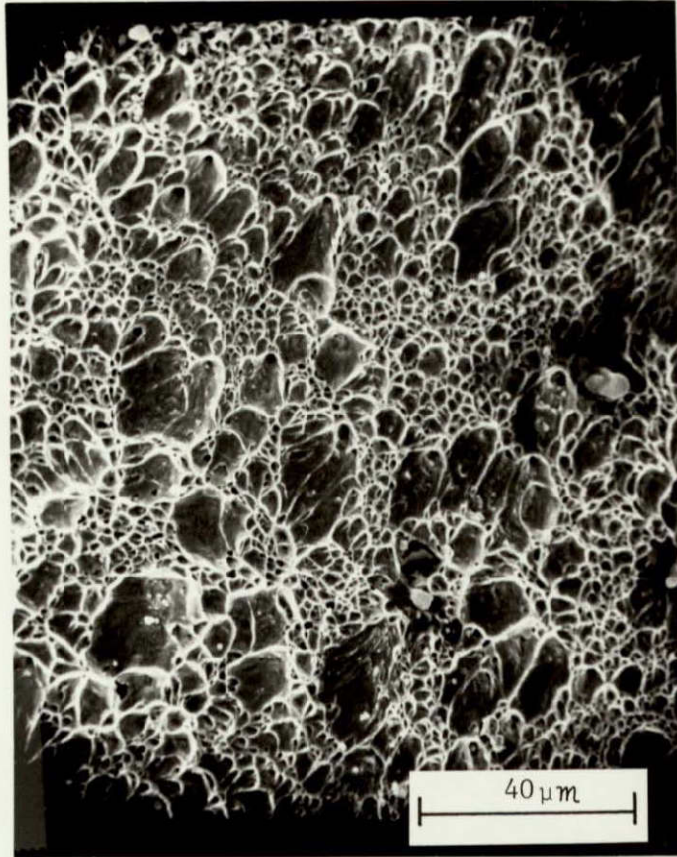


(a) Tensile Specimen

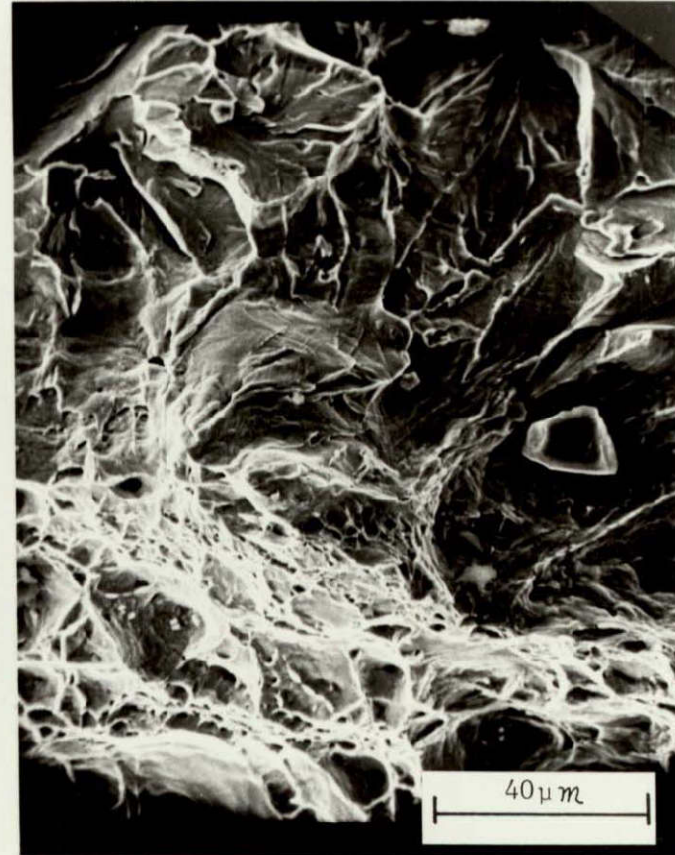


(b) Notch Bend Specimen

Figure 17 SEM fractographs of Fe-12Ni-0.18Ti alloy heat treated at 820°C and tested at 77K.



(a) Tensile Specimen



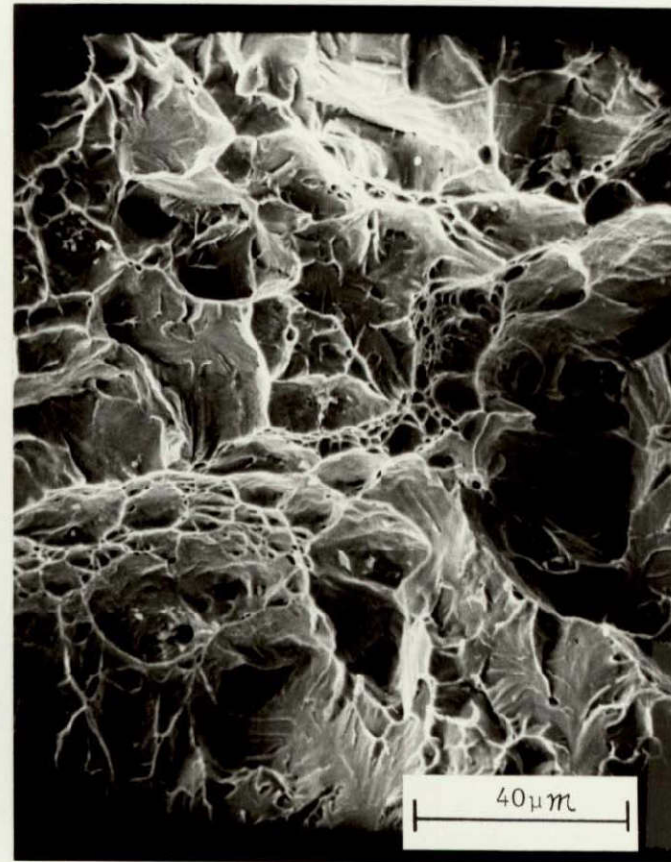
(b) Notch Bend Specimen

Figure 18 SEM fractographs of Fe-12Ni-0.47Ti alloy heat treated at 820°C and tested at 77K.

ORIGINAL PAGE IS  
OF POOR QUALITY



(a) Tensile Specimen



(b) Notch Bend Specimen

Figure 19 SEM fractographs of Fe-12Ni-0.99Ti alloy heat treated at 820°C and tested at 77K.

ORIGINAL PAGE IS  
OF POOR QUALITY

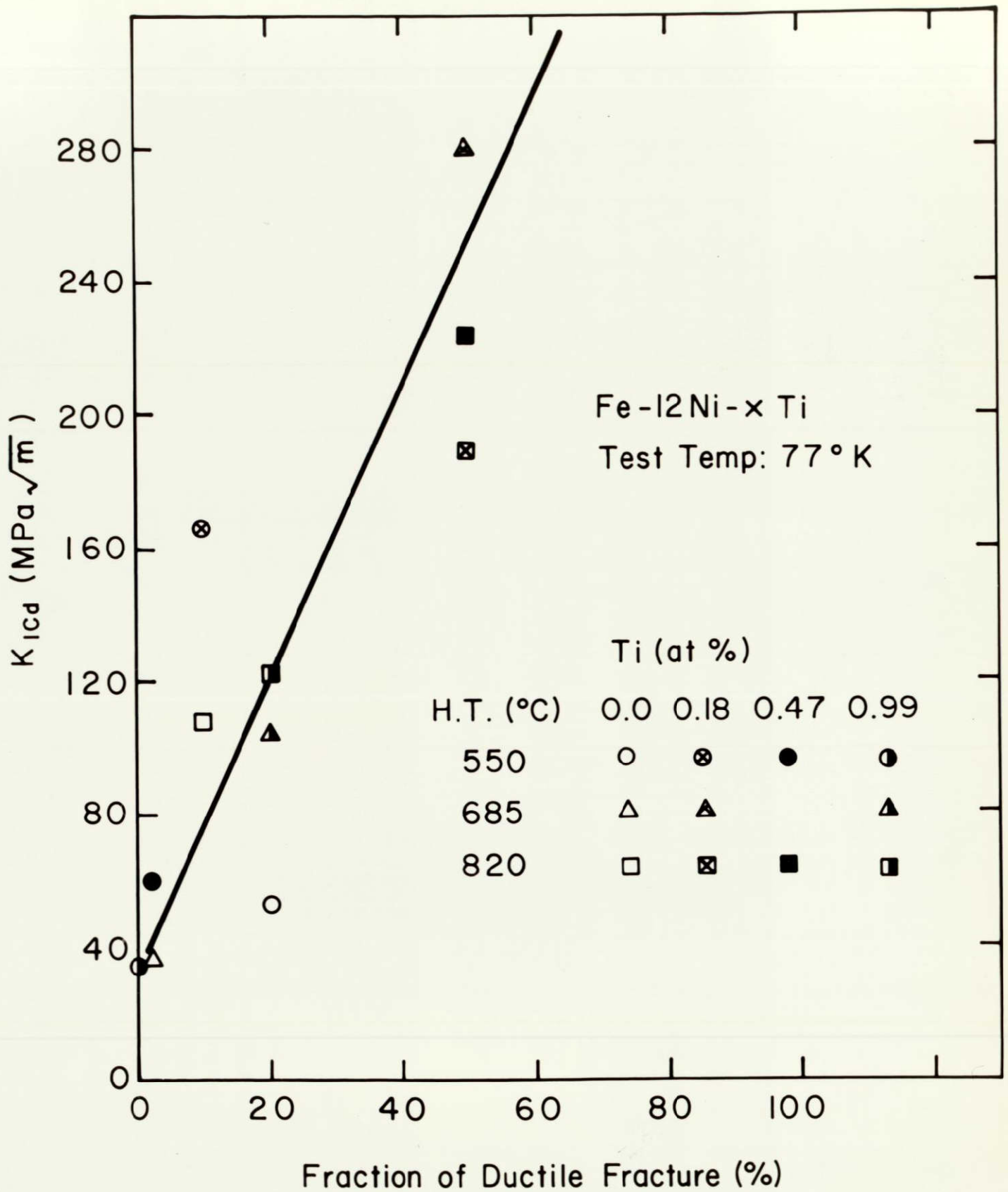


Fig. 20.  $K_{Icd}$  versus the fraction of ductile fracture at 77K for Fe-12Ni - xTi alloys heat treated at 550, 685, and 820°C.



(a) Fe-12Ni alloy



(b) Fe-12Ni-0.18Ti alloy

Figure 21 Optical microstructure of Fe-12Ni and Fe-12Ni-0.18Ti specimens heat treated at 550°C.

ORIGINAL PAGE IS  
OF POOR QUALITY



(a) Fe-12Ni-0.47Ti alloy



(b) Fe-12Ni-0.99Ti alloy

Figure 22 Optical microstructure Fe-12Ni-0.47Ti and Fe-12Ni-0.99Ti specimens heat treated at 550°C.

ORIGINAL PAGE IS  
OF POOR QUALITY



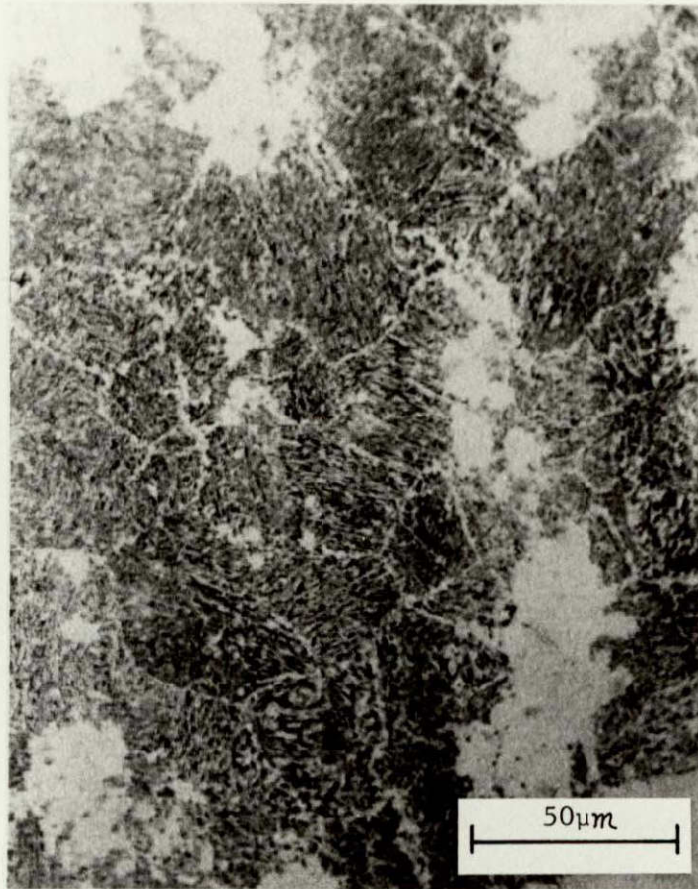


(a) Fe-12Ni alloy



(b) Fe-12Ni-0.18Ti alloy

Figure 23 Optical microstructure of Fe-12Ni and Fe-12Ni-0.18Ti specimens heat treated at 685°C.

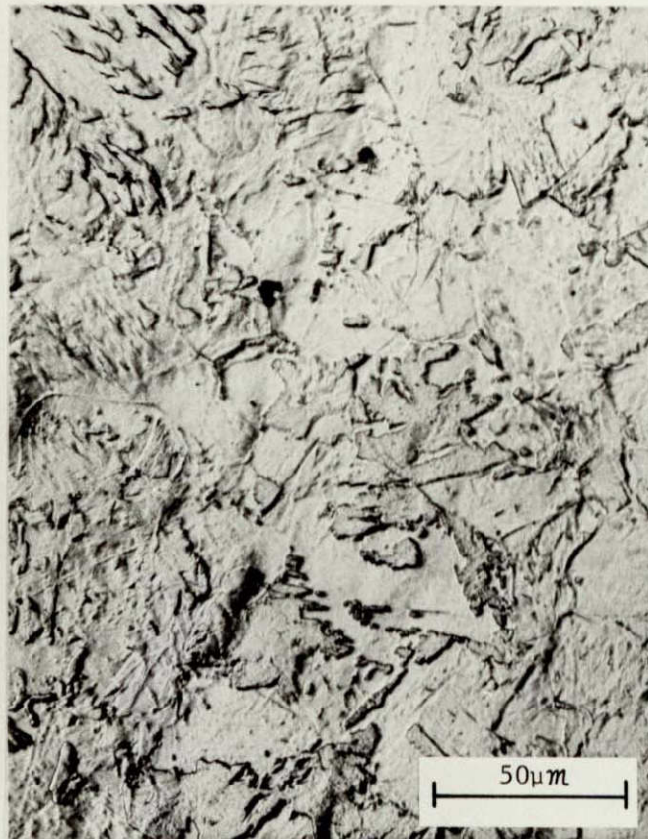


ORIGINAL PAGE IS  
OF POOR QUALITY

Figure 24 Optical microstructure of Fe-12Ni-0.99Ti specimens heat treated at 685°C.



(a) Fe-12Ni alloy



(b) Fe-12Ni-0.18Ti alloy

Figure 25 Optical microstructure of Fe-12Ni and Fe-12Ni-0.18Ti specimens heat treated at 820°C.

ORIGINAL PAGE IS  
OF POOR QUALITY



(a) Fe-12Ni-0.47Ti alloy



(b) Fe-12Ni-0.99Ti alloy

Figure 26 Optical microstructure of Fe-12Ni-0.47Ti and Fe-12Ni-0.99Ti specimens heat treated at 820°C.

ORIGINAL PAGE IS  
OF POOR QUALITY



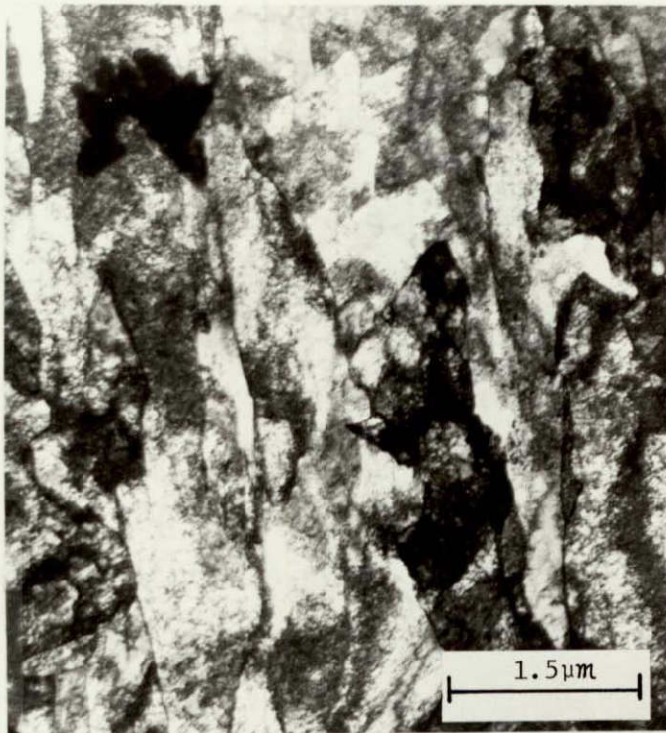
Foil Orientation  $\langle 110 \rangle$   
(a) Fe-12Ni alloy



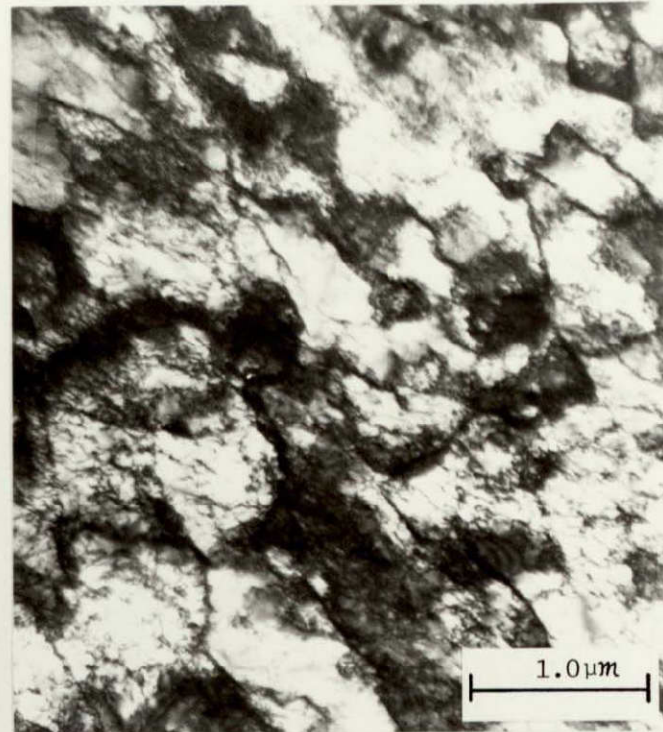
Foil Orientation  $\langle 110 \rangle$   
(b) Fe-12Ni-0.18Ti Alloy

Figure 27 TEM microstructure of Fe-12Ni and Fe-12Ni-0.18Ti alloys heat treated at 550°C.

ORIGINAL PAGE IS  
OF POOR QUALITY



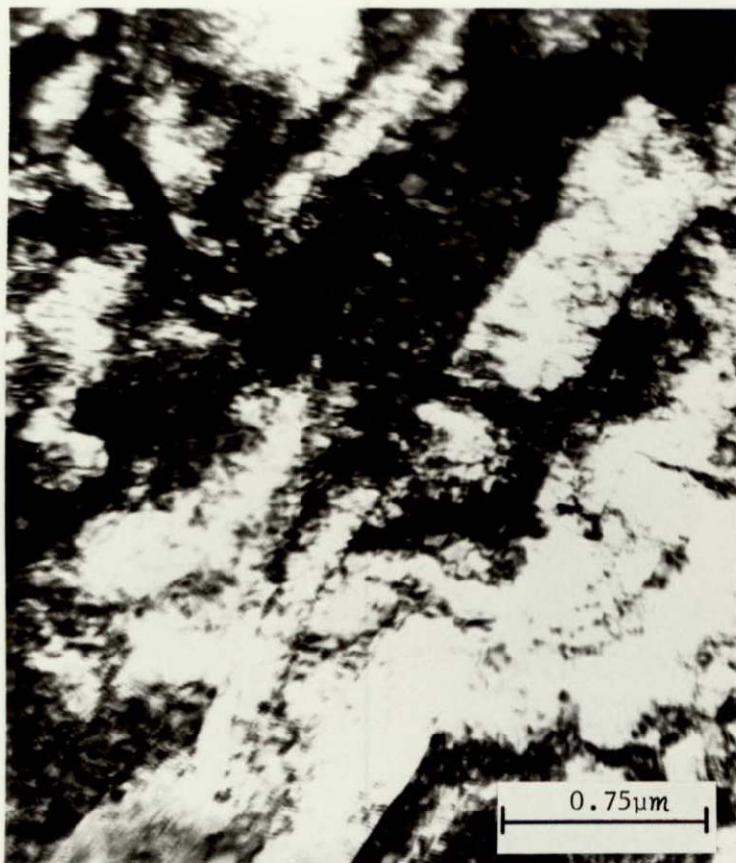
Foil Orientation  $\langle 111 \rangle$   
(a) Fe-12Ni alloy



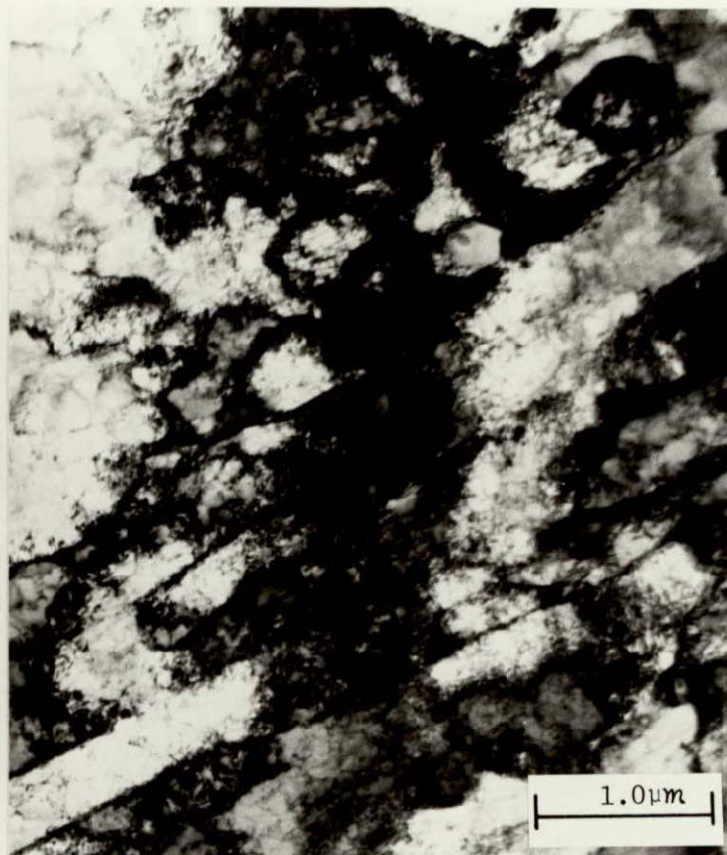
Foil Orientation  $\langle 111 \rangle$   
(b) Fe-12Ni-0.18Ti alloy

Figure 28 TEM microstructure of Fe-12Ni and Fe-12Ni-0.18Ti alloys heat treated at 685°C.

ORIGINAL PAGE IS  
OF POOR QUALITY



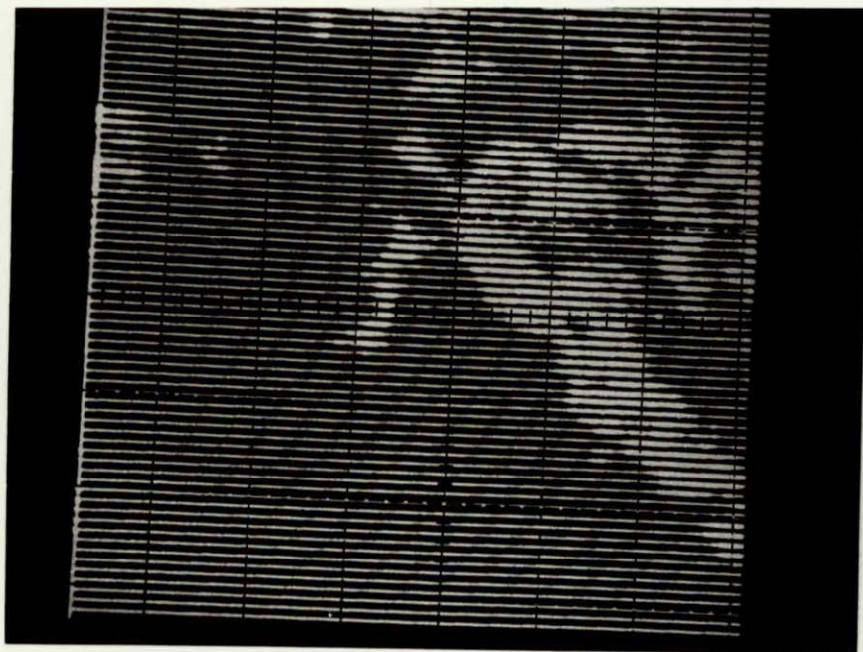
Foil Orientation  $\langle 111 \rangle$   
(a) Fe-12Ni alloy



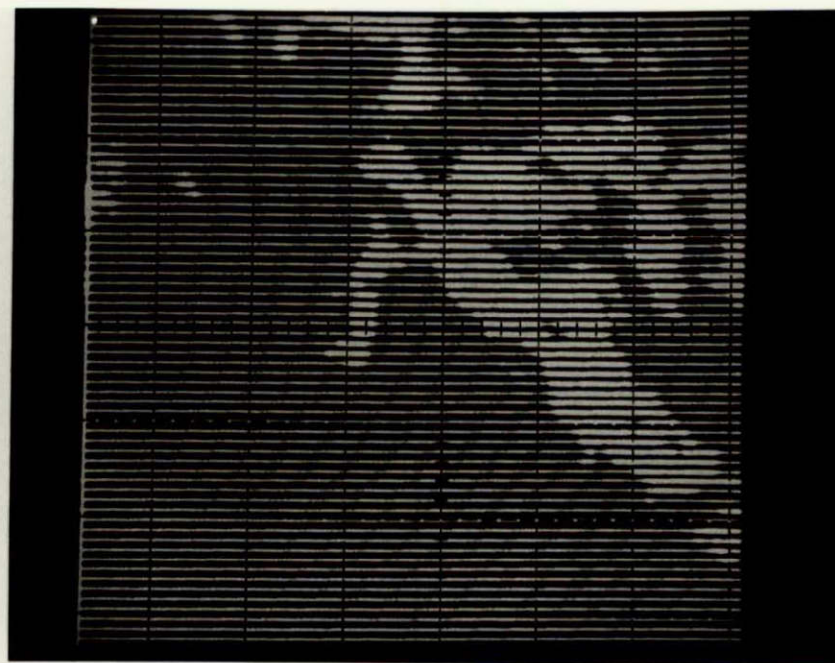
Foil Orientation  $\langle 012 \rangle$   
(b) Fe-12Ni-0.18Ti alloy

Figure 29 TEM microstructure of Fe-12Ni and Fe-12Ni-0.18Ti alloys heat treated at 820°C.

ORIGINAL PAGE IS  
OF POOR QUALITY



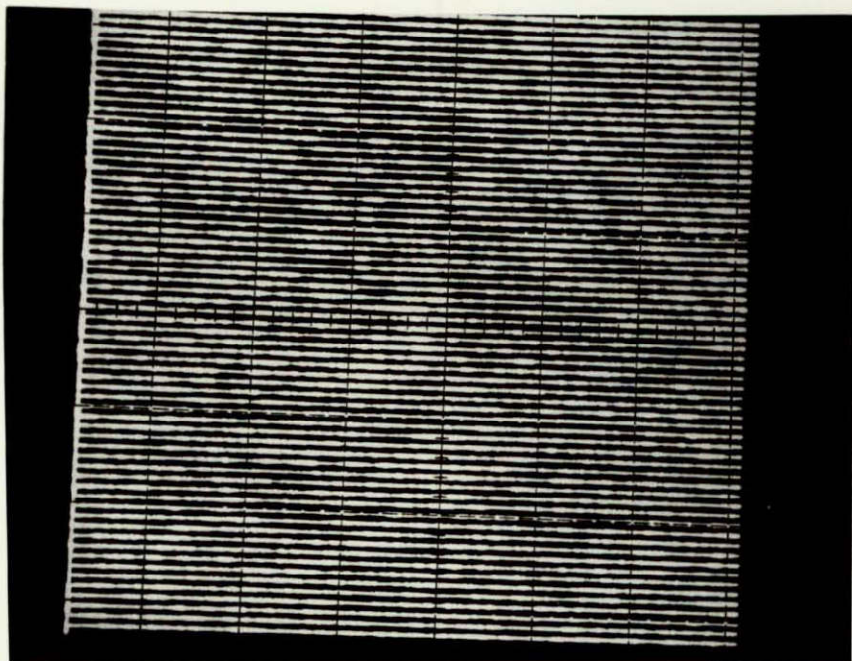
Auger Spectrum mapping for Ni at 847eV



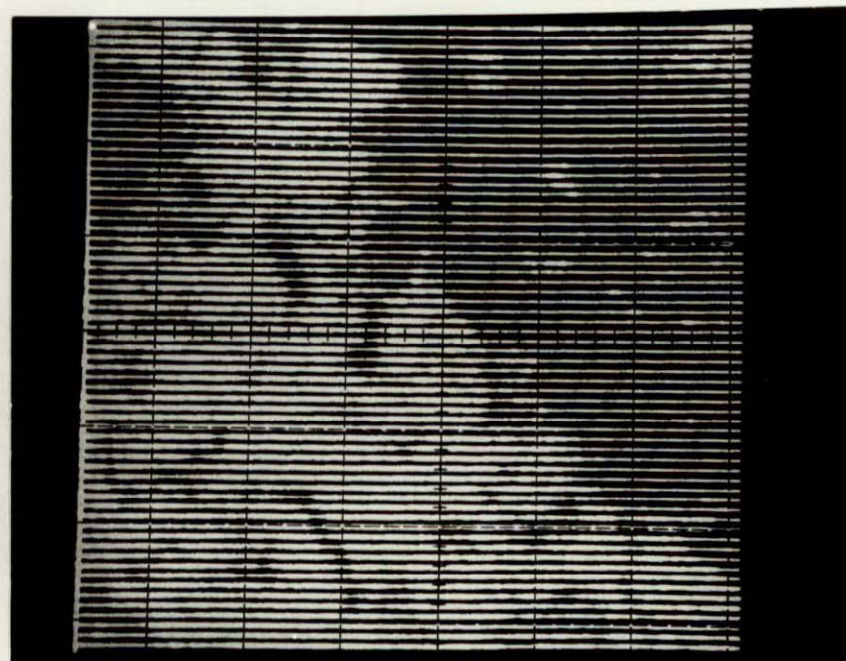
Auger Spectrum mapping for Fe at 595eV

Figure 30 Auger Spectrum mapping for Ni and Fe of the fracture surface of a notch bend specimen for Fe-12Ni alloy heat treated at 550°C and tested at 77K.



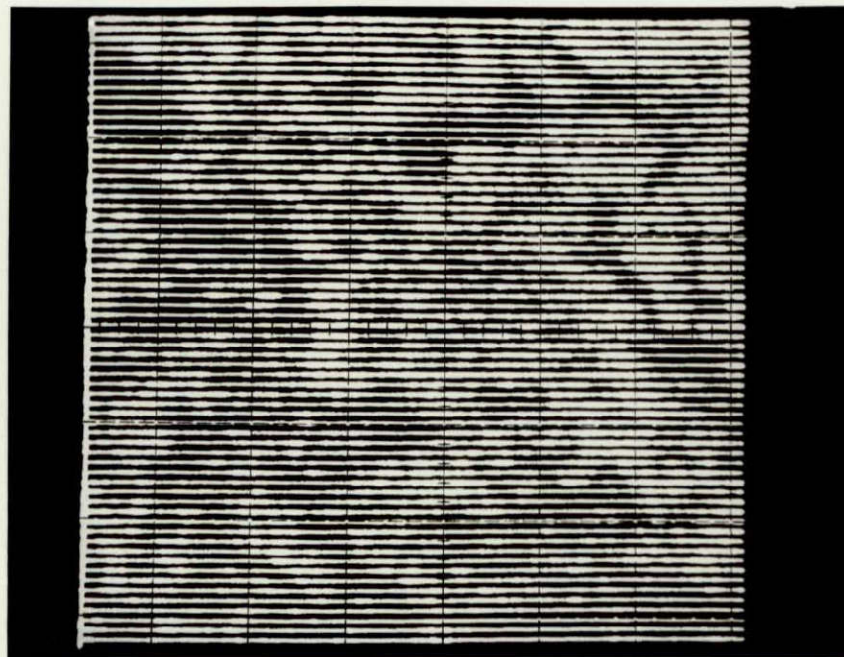


Auger Spectrum mapping for O at 510eV



Auger Spectrum mapping for C at 271eV

Figure 31 Auger Spectrum mapping for O and C of the fracture surface of a notch bend specimen of Fe-12Ni alloy heated treated at 550°C and tested at 77K.



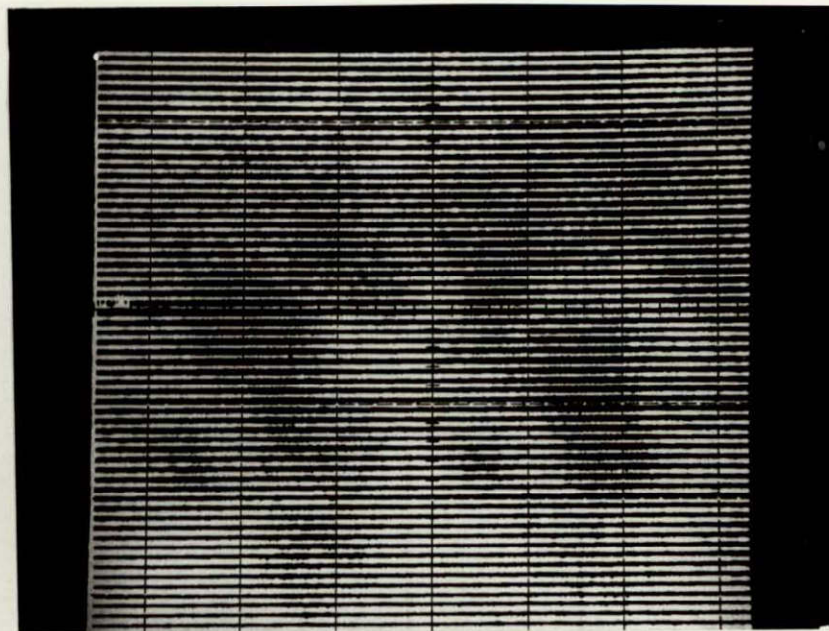
ORIGINAL PAGE IS  
OF POOR QUALITY

Auger Spectrum mapping for N at 383eV

Figure 32 Auger Spectrum mapping for N of the fracture surface of a notch bend specimen for Fe-12Ni alloy heat treated at 550°C and tested at 77K.

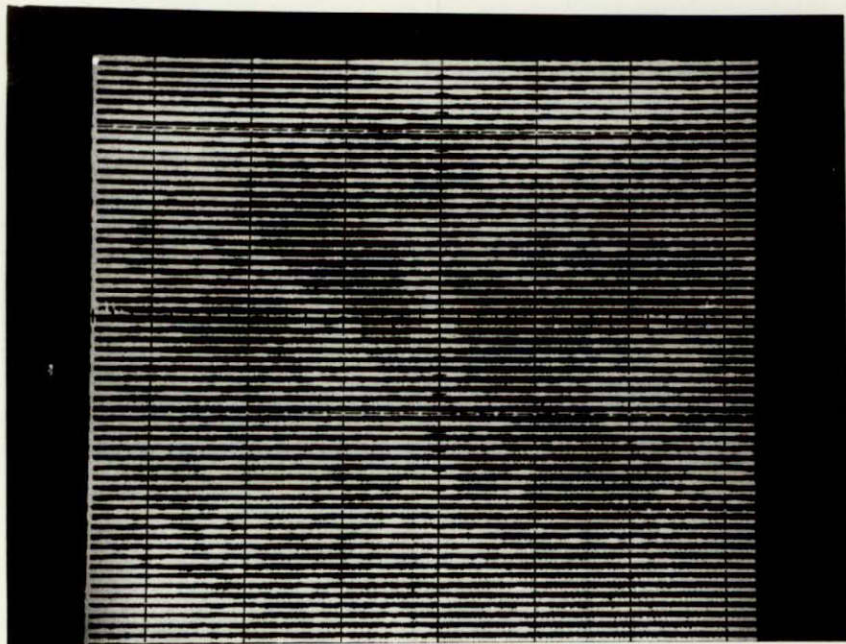


Auger Spectrum mapping for Ni at 780eV

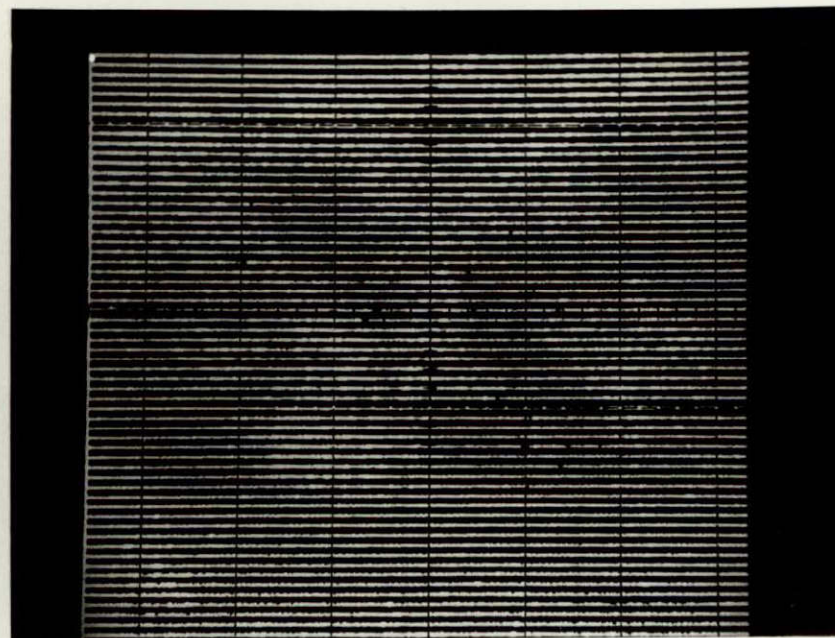


Auger Spectrum mapping for O at 510eV

Figure 33 Auger Spectrum mappings for Ni and O of the fracture surface of a notch bend specimen of Fe-12Ni-0.18Ti alloy annealed at 550°C and tested at 77K.

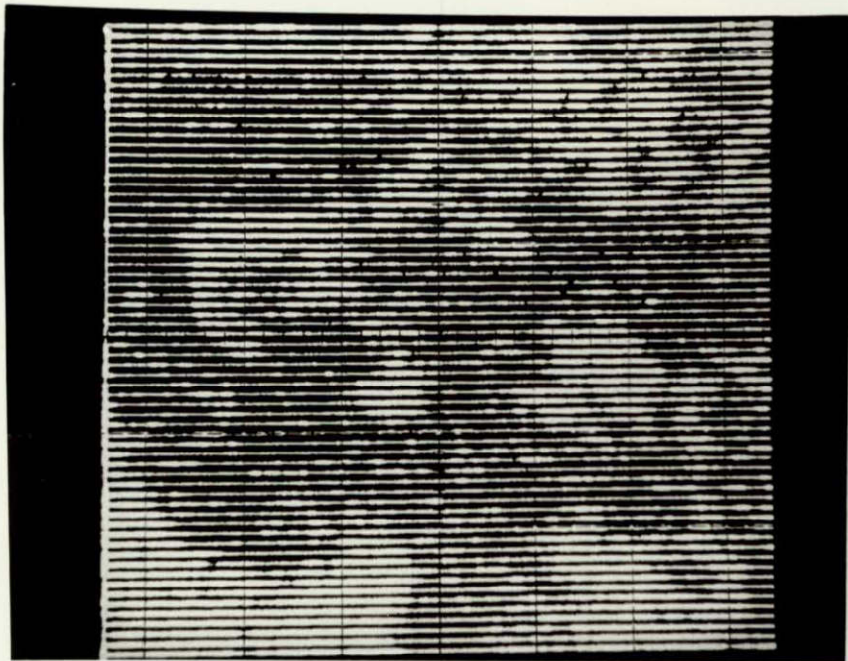


Auger Spectrum mapping for Ti at 453eV

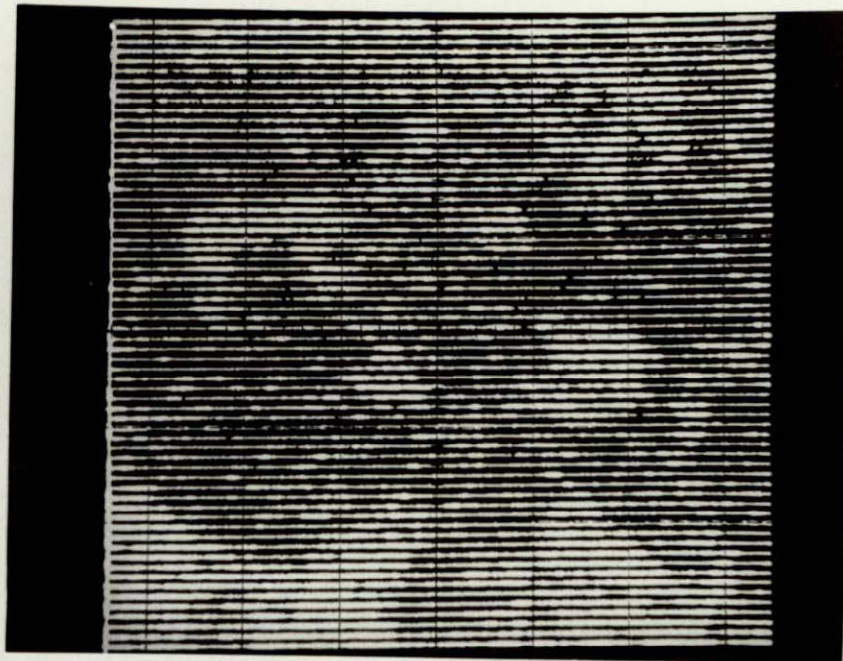


Auger Spectrum mapping for C at 271eV

Figure 34 Auger Spectrum mapping for Ti and C of the fracture surface of a notch bend specimen of Fe-12Ni-0.18Ti alloy annealed at 550°C and tested at 77K.

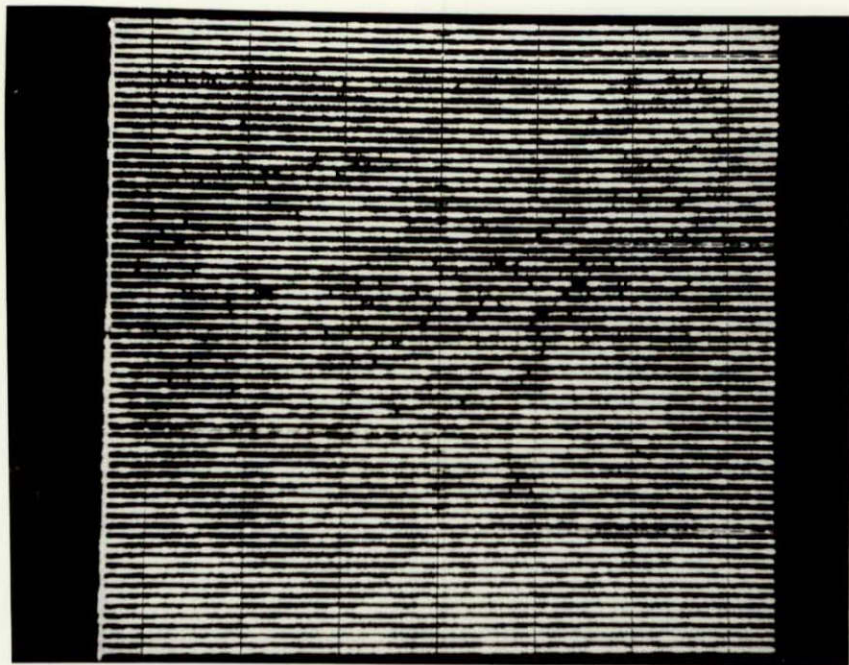


Auger Spectrum mapping for Ni at 847eV

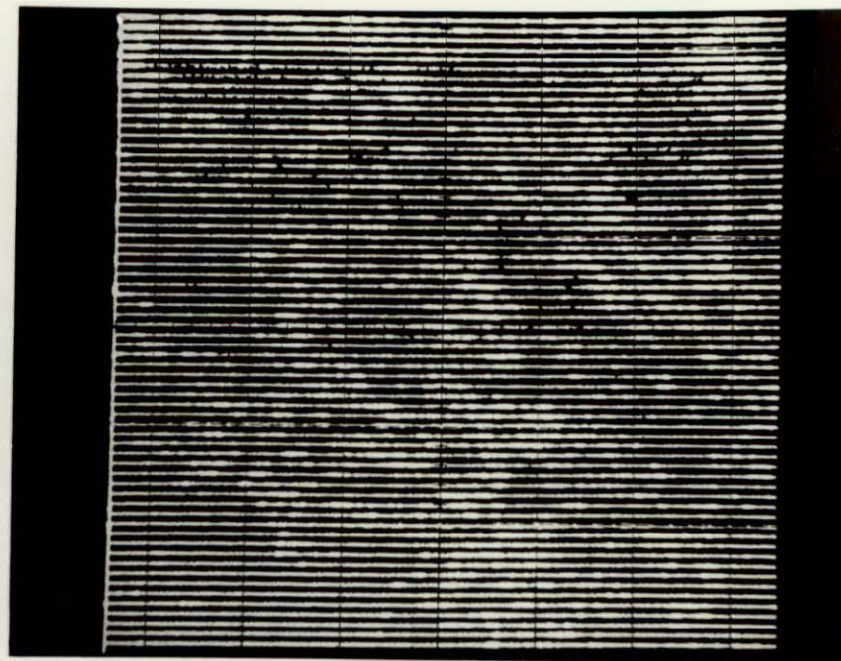


Auger Spectrum mapping for Fe at 595eV

Figure 35 Auger Spectrum mapping for Ni and Fe of the fracture surface of a notch bend specimen of Fe-12Ni-0.47Ti alloy heat treated at 550°C and tested at 77K.

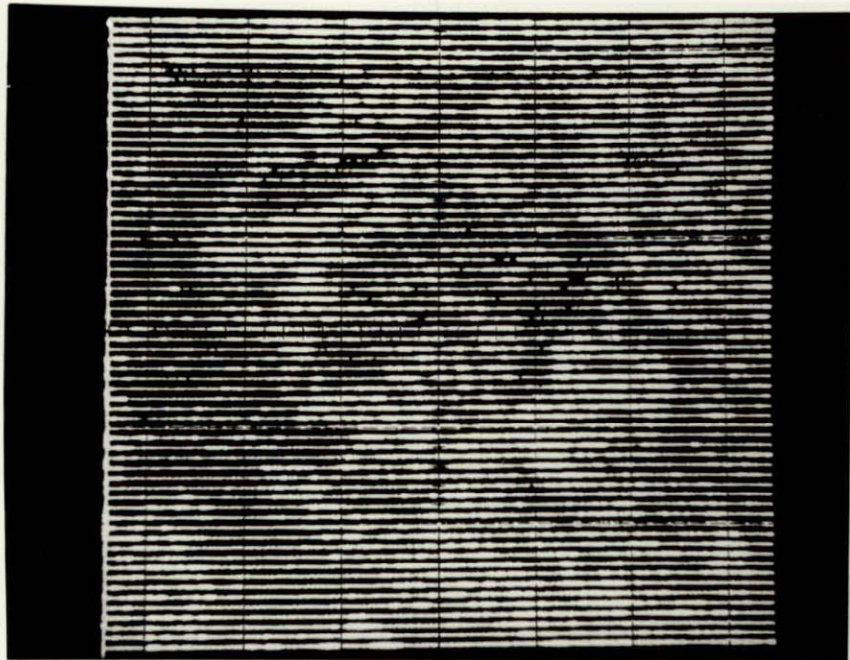


Auger Spectrum mapping for Ti at 453eV

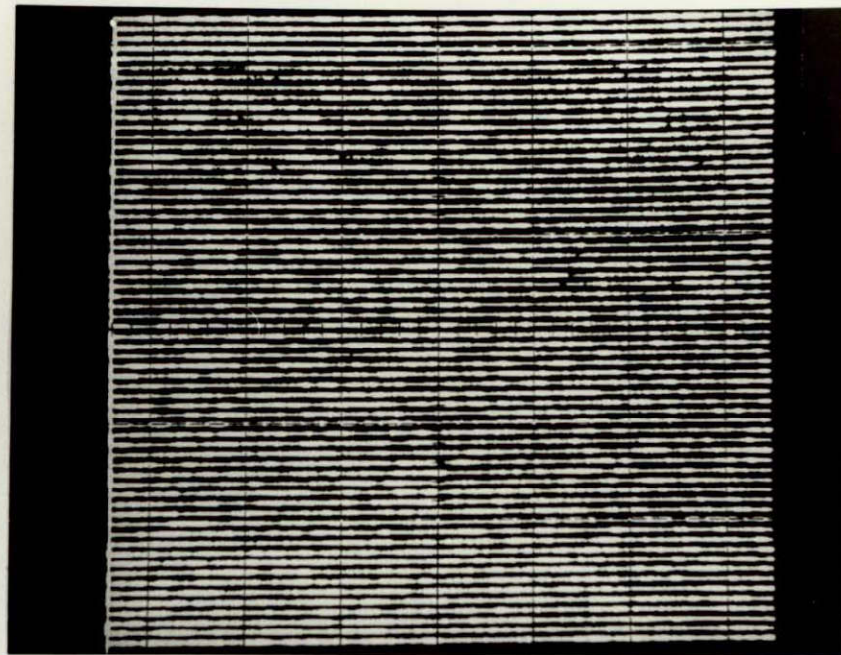


Auger Spectrum mapping for C at 271eV

Figure 36 Auger Spectrum mapping for Ti and C of the fracture surface of a notch bend specimen of Fe-12Ni-0.47Ti alloy heat treated at 550°C and tested at 77K.

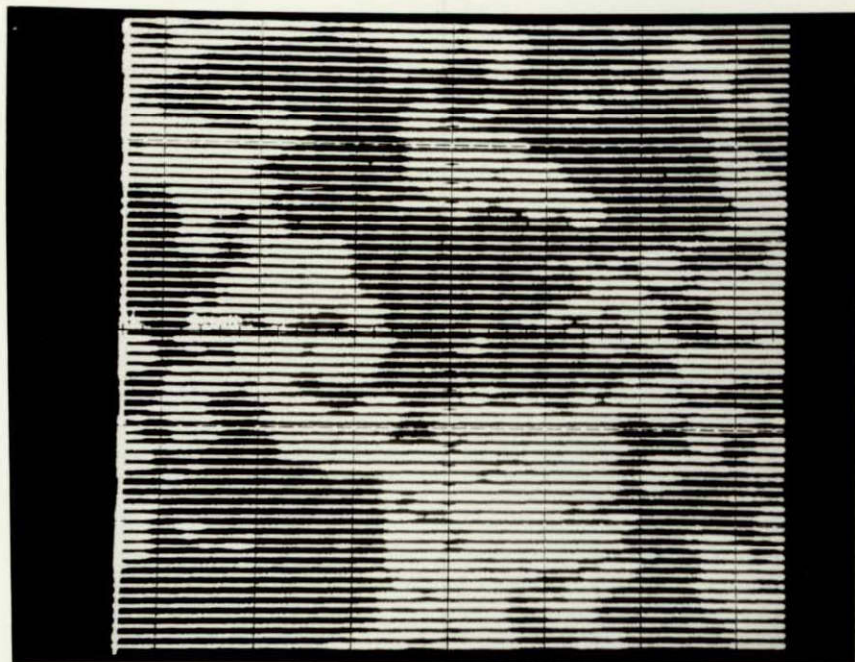


Auger Spectrum mapping for N at 383eV

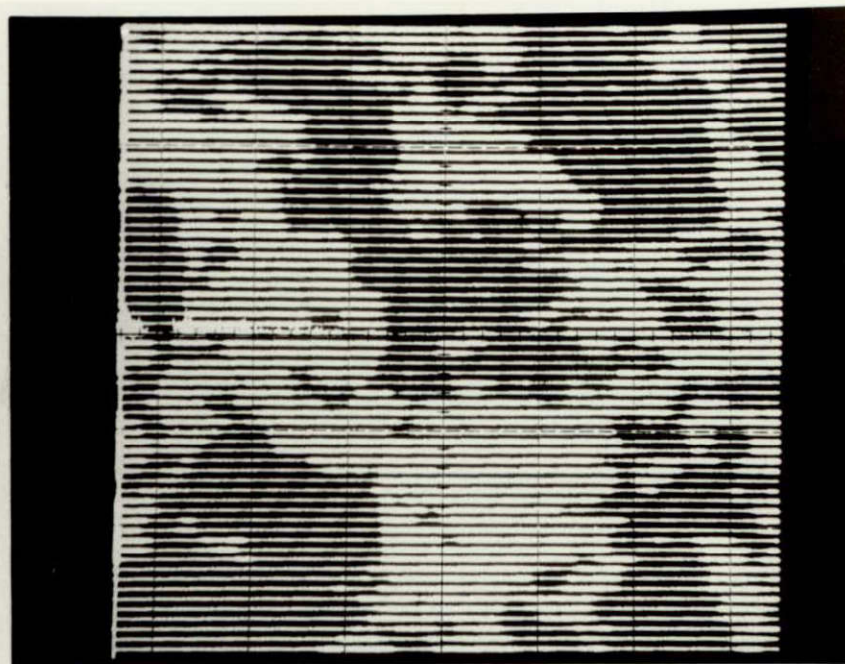


Auger Spectrum mapping for O at 510eV

Figure 37 Auger Spectrum mapping for N and O of the fracture surface of a notch bend specimen of Fe-12Ni-0.47Ti alloy heat treated at 550°C and tested at 77K.



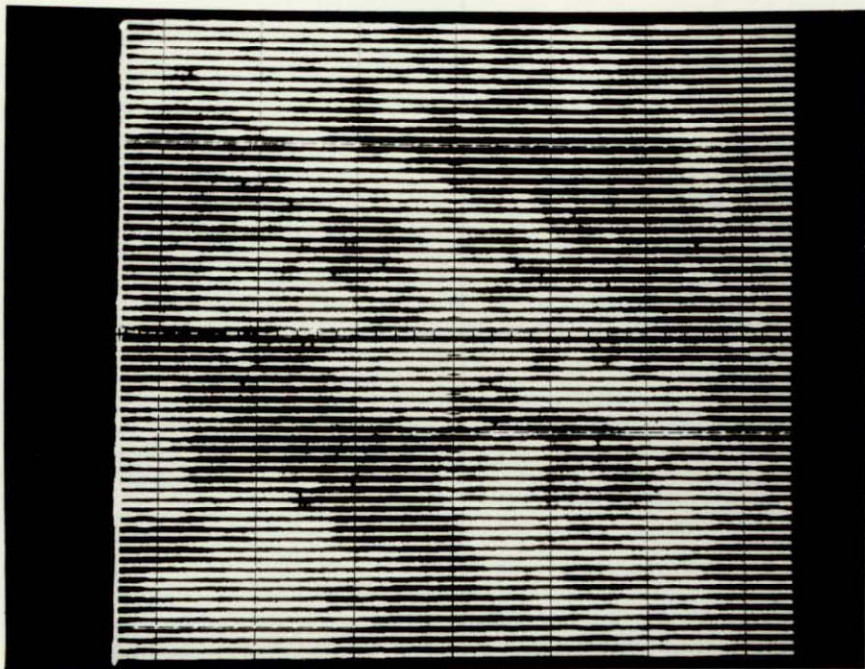
Auger Spectrum mapping for Ni at 847eV



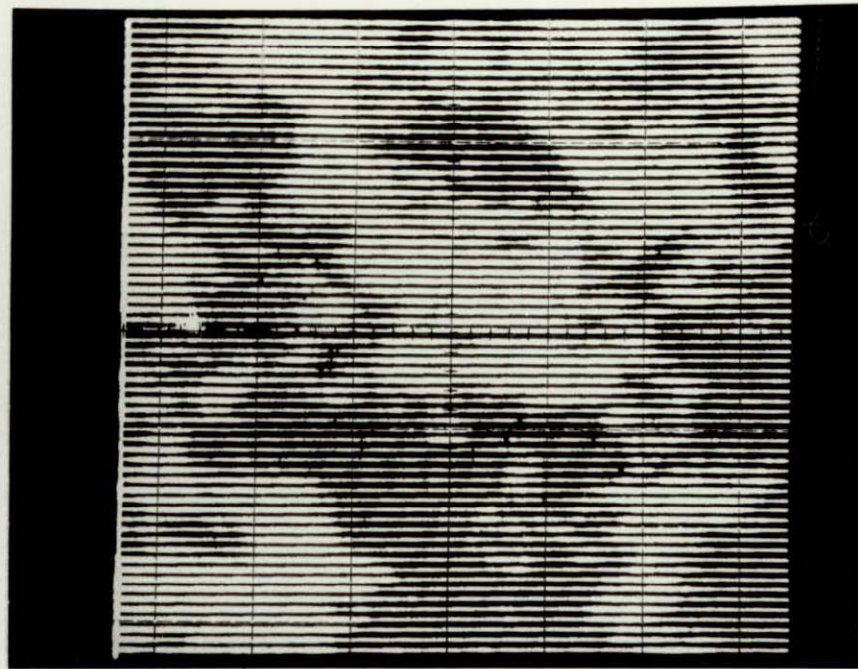
Auger Spectrum mapping for Fe at 595eV

Figure 38 Auger Spectrum mapping for Ni and Fe of the fracture surface of a notch bend specimen of Fe-12Ni alloy heat treated at 685°C and tested at 77K.



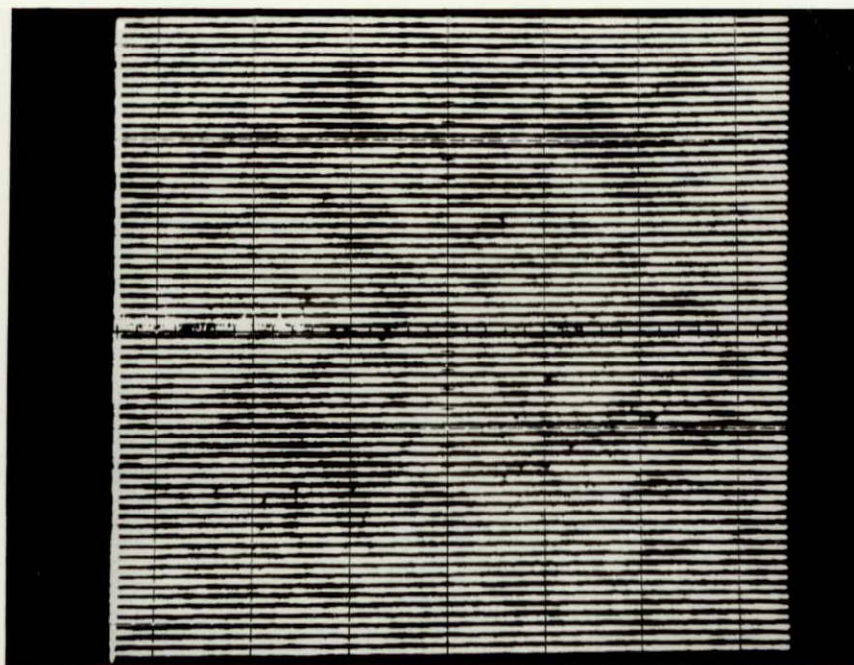


Auger Spectrum mapping for O at 510eV



Auger Spectrum mapping for C at 271eV

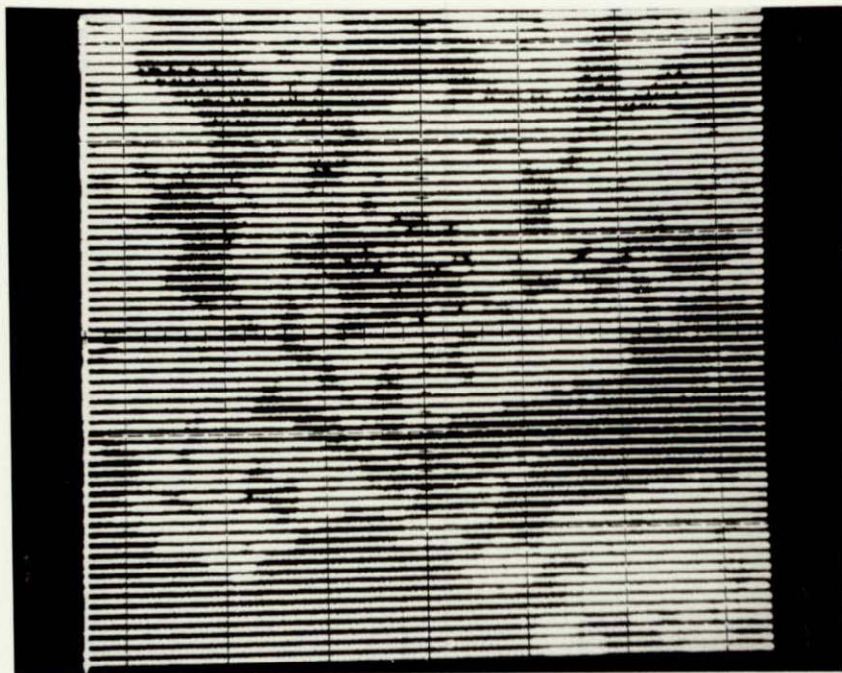
Figure 39 Auger Spectrum mapping for O and C of the fracture surface of a notch bend specimen of Fe-12Ni alloy heat treated at 685°C and tested at 77K.



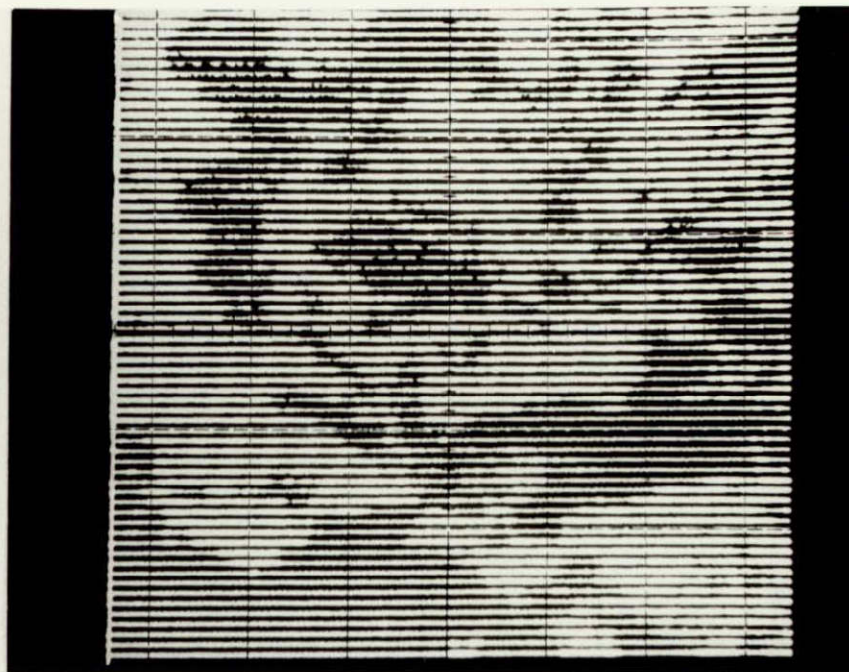
ORIGINAL PAGE IS  
OF POOR QUALITY

Auger Spectrum mapping for N at 383eV

Figure 40 Auger Spectrum mapping for N of the fracture surface of a notch bend specimen of Fe-12Ni alloy heat treated at 685°C and tested at 77K.

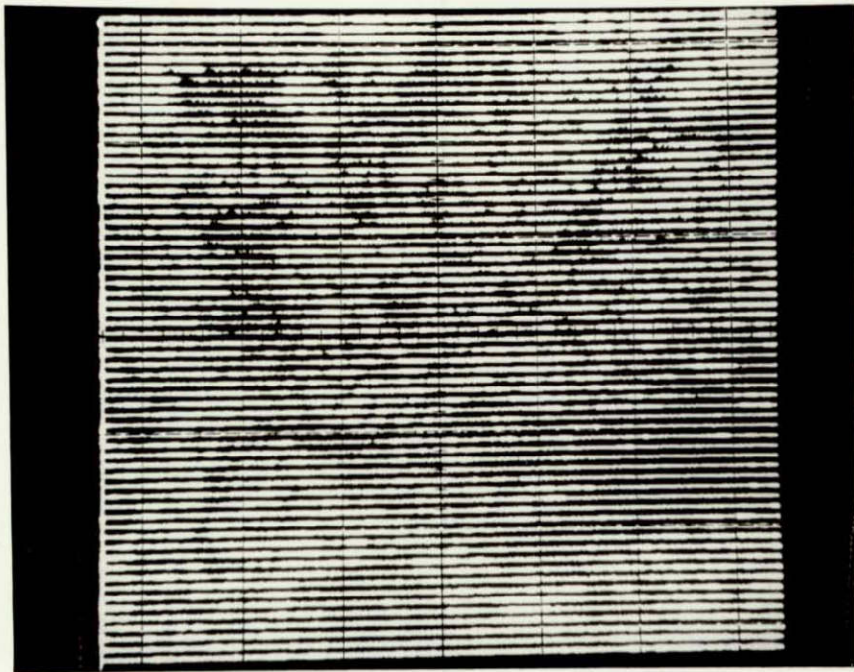


Auger Spectrum mapping for Ni at 847eV

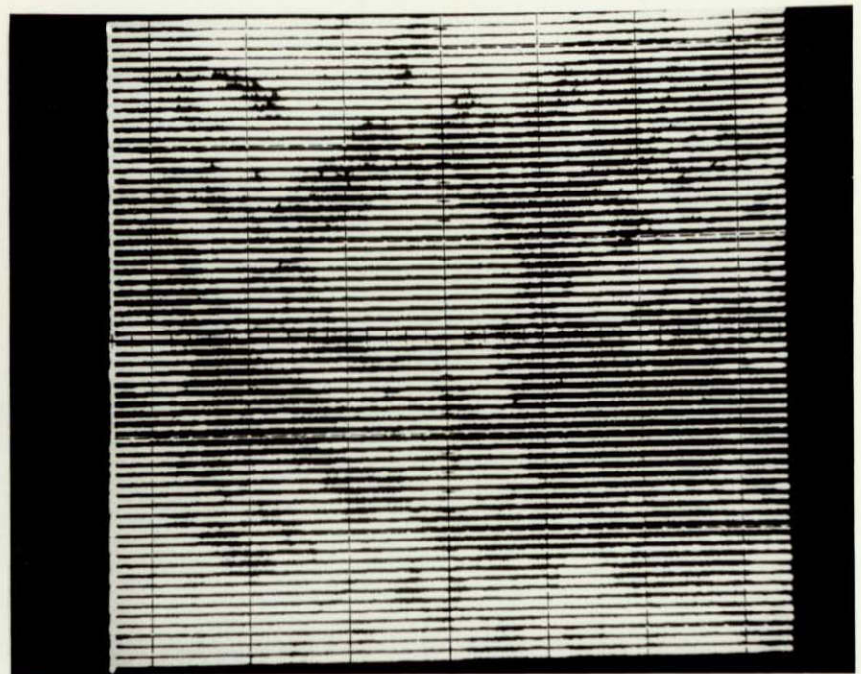


Auger Spectrum mapping for Fe at 595eV

Figure 41 Auger Spectrum mapping for Ni and Fe of the fracture surface of a notch bend specimen of Fe-12Ni-0.18Ti alloy heat treated at 685°C and tested at 77K.

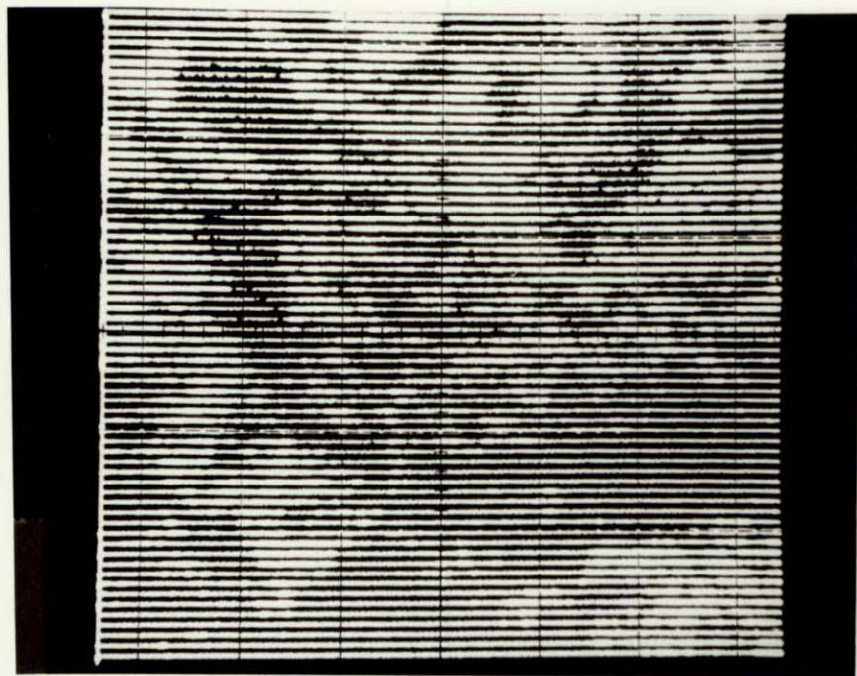


Auger Spectrum mapping for Ti at 453eV

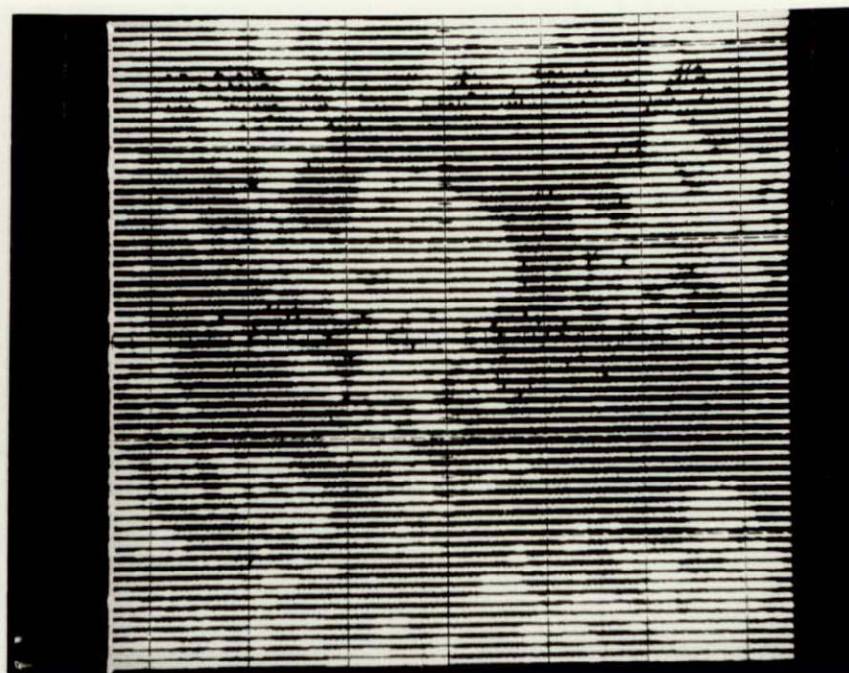


Auger Spectrum mapping for C at 271eV

Figure 42 Auger Spectrum mapping for Ti and C of the fracture surface of a notch bend specimen of Fe-12Ni-0.18Ti alloy heat treated at 685°C and tested at 77K.



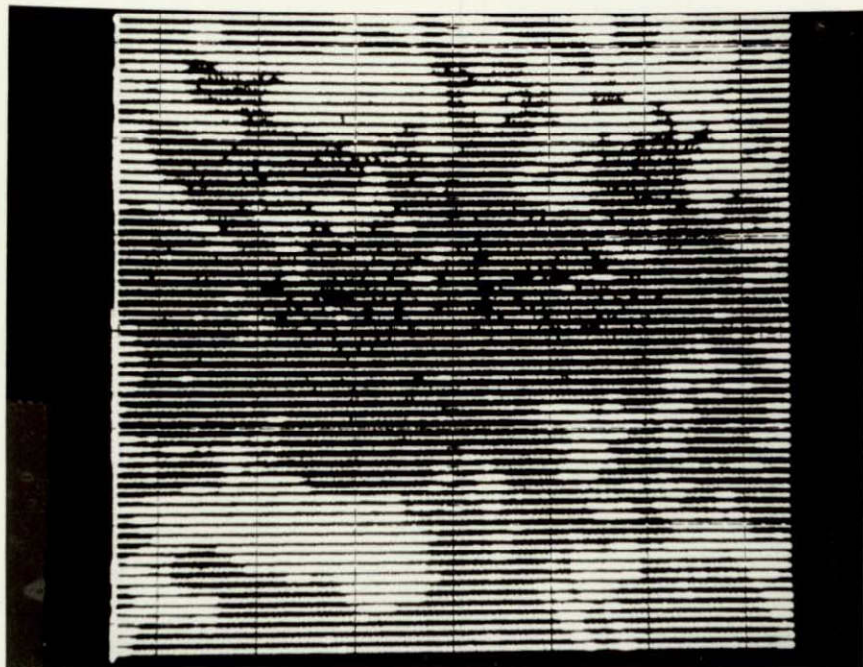
Auger Spectrum Mapping for N at 383eV



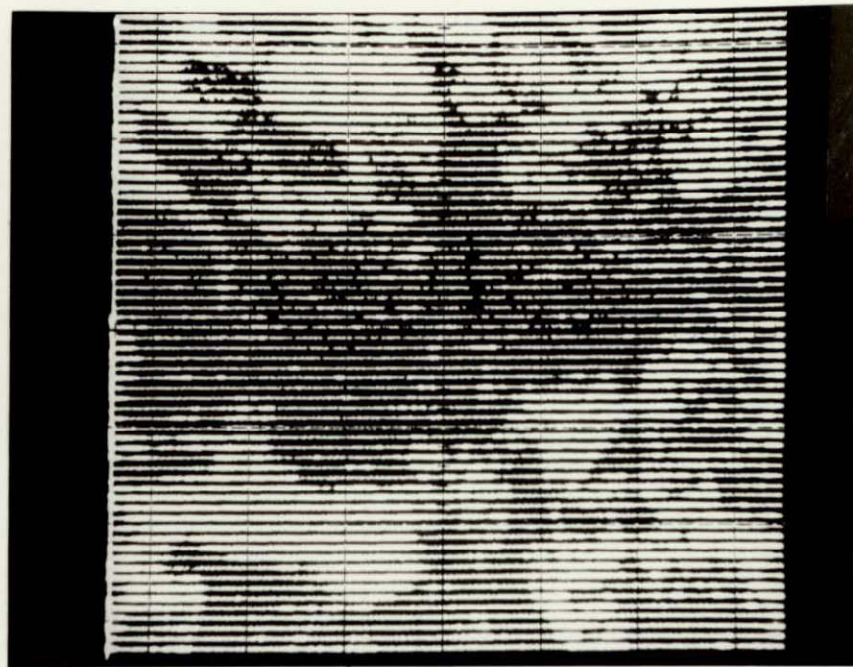
Auger Spectrum mapping for O at 510eV

Figure 43 Auger Spectrum mapping for N and O of the fracture surface of a notch ben specimen of Fe-12Ni-0.18Ti alloy heat treated at 685°C and tested at 77K.

ORIGINAL PAGE IS  
OF POOR QUALITY

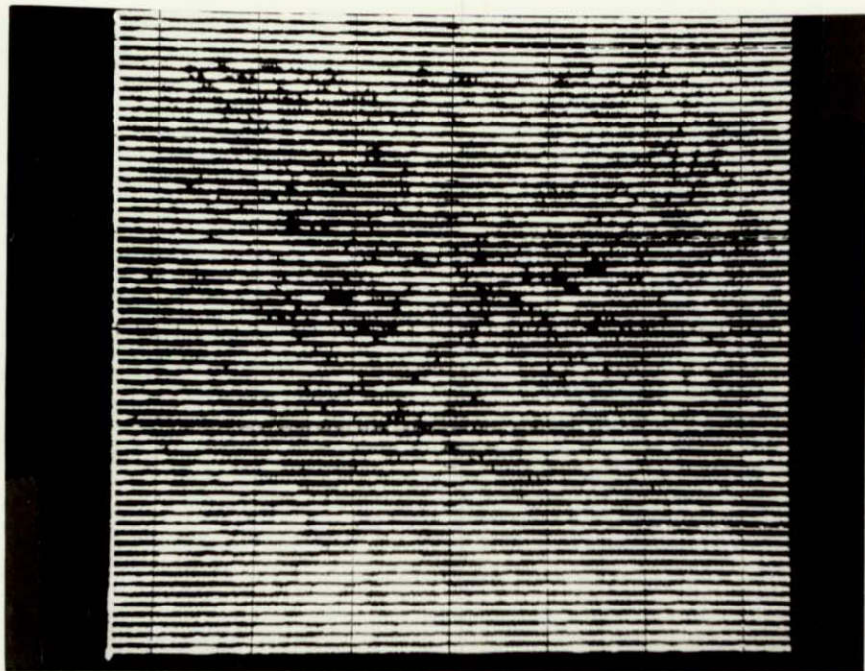


Auger Spectrum mapping for Ni at 847eV

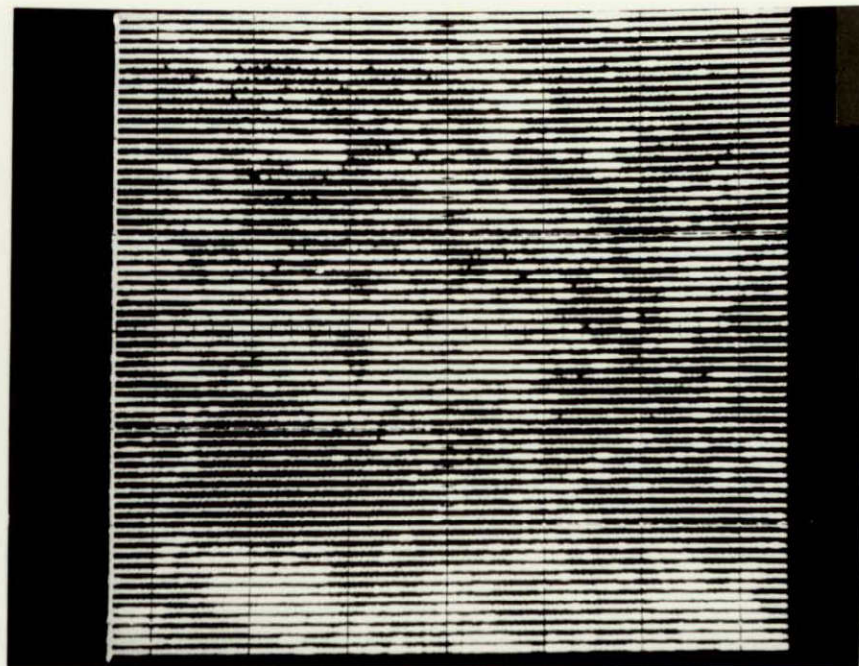


Auger Spectrum mapping for Fe at 595eV

Figure 44 Auger Spectrum mapping for Ni and Fe of the fracture surface of a notch bend specimen of Fe-12Ni-0.99Ti alloy heat treated at 685°C and tested at 77K.

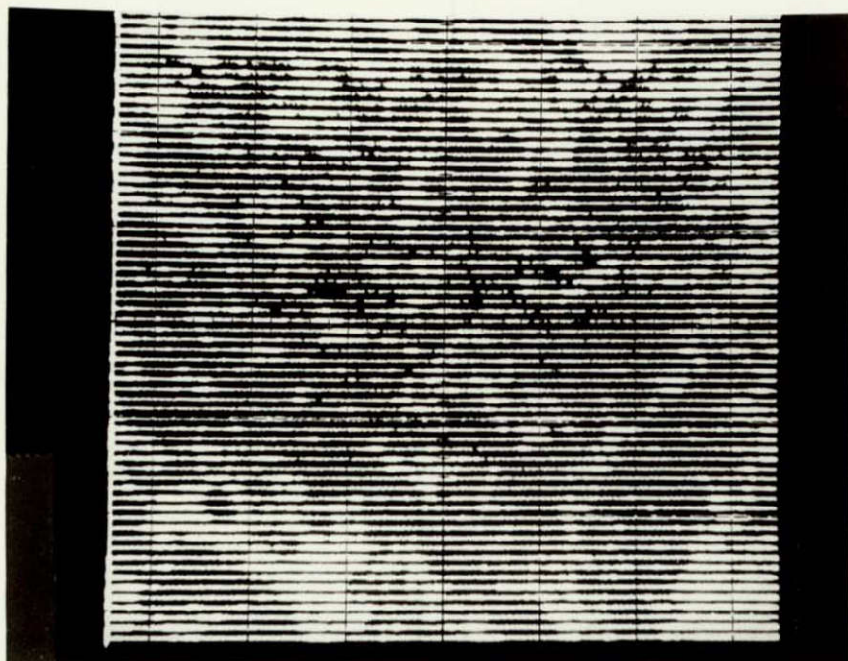


Auger Spectrum mapping for Ti at 453eV

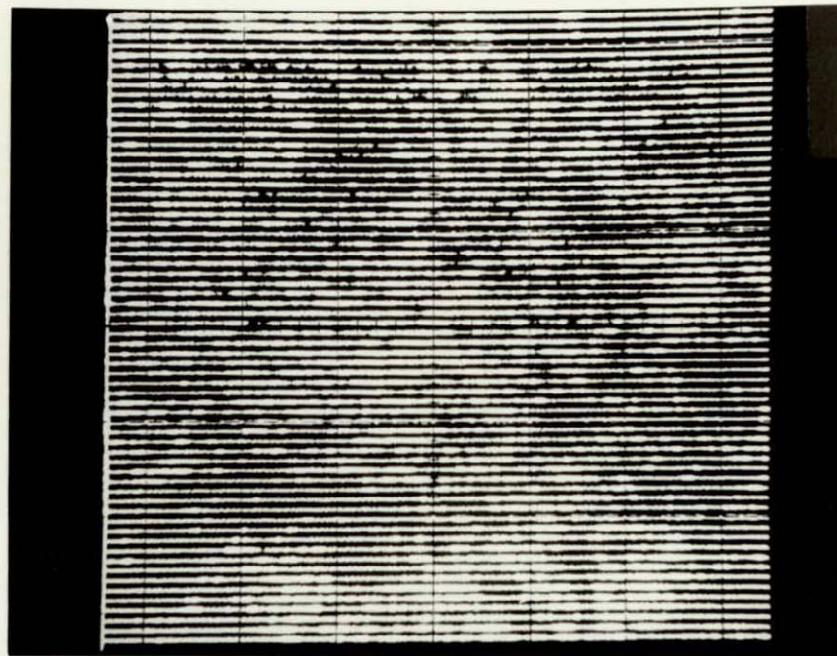


Auger Spectrum mapping for C at 271eV

Figure 45 Auger Spectrum mapping for Ti and C of the fracture surface of a notch bend specimen of Fe-12Ni-0.99Ti alloy heat treated at 685°C and tested at 77K.



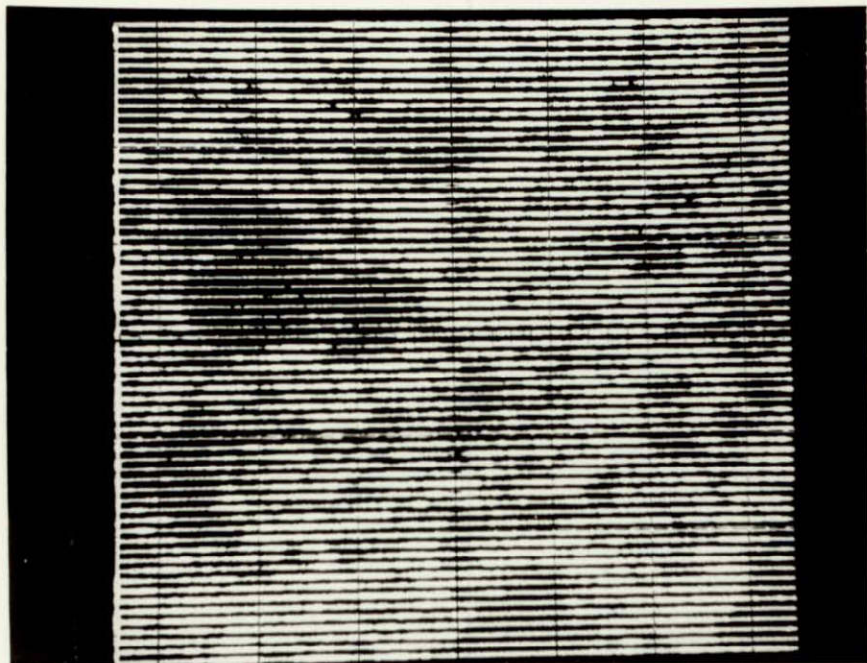
Auger Spectrum mapping for N at 383eV



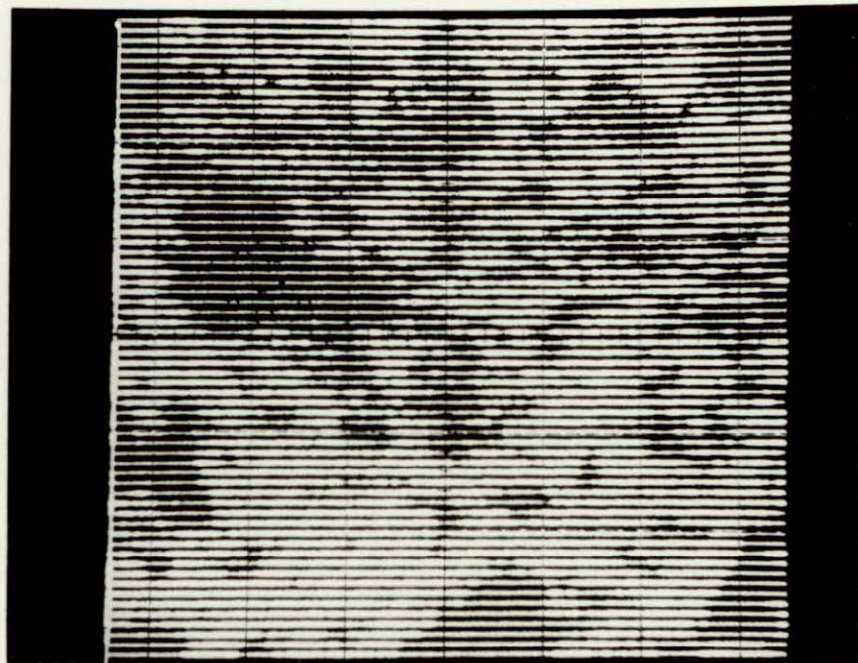
Auger Spectrum mapping for O at 510eV

Figure 46 Auger Spectrum mapping for N and O of the fracture surface of a notch bend specimen of Fe-12Ni-0.99Ti alloy heat treated at 685°C and tested at 77K.



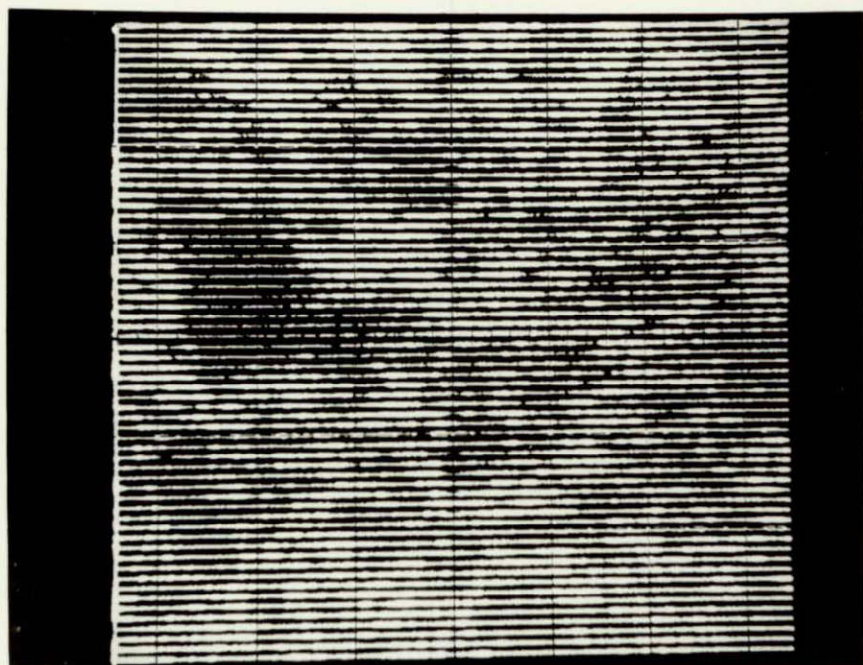


Auger Spectrum mapping for Ni at 847eV

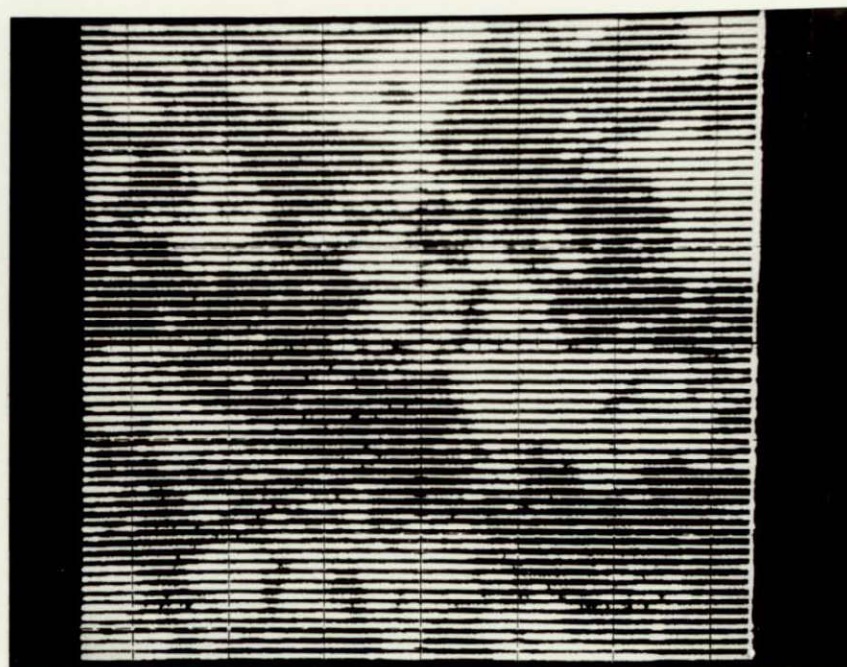


Auger Spectrum mapping for Fe at 595eV

Figure 47 Auger Spectrum mapping for Ni and Fe of the fracture surface of a notch bend specimen of Fe-12Ni-0.18Ti alloy heat treated at 820°C and tested at 77K.

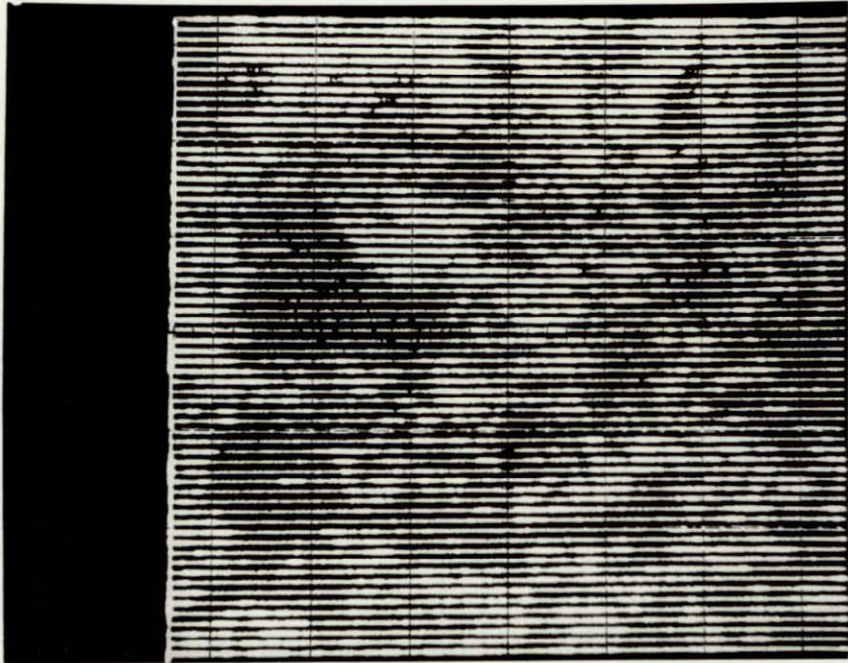


Auger Spectrum mapping for Ti at 417eV

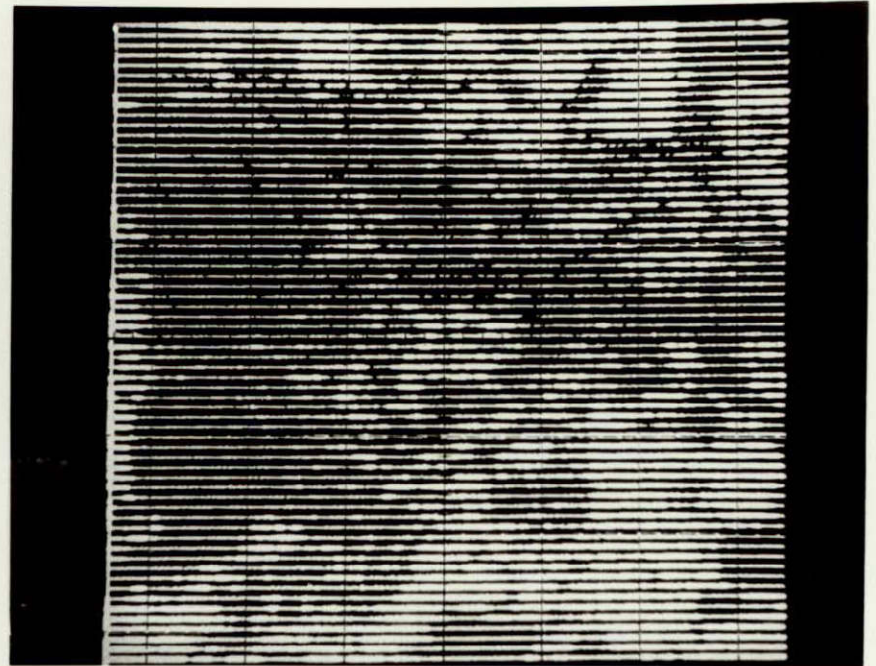


Auger Spectrum mapping for C at 271eV

Figure 48 Auger Spectrum mapping for Ti and C of the fracture surface of a notch bend specimen of Fe-12Ni-0.18Ti alloy heat treated at 820°C and tested at 77K.

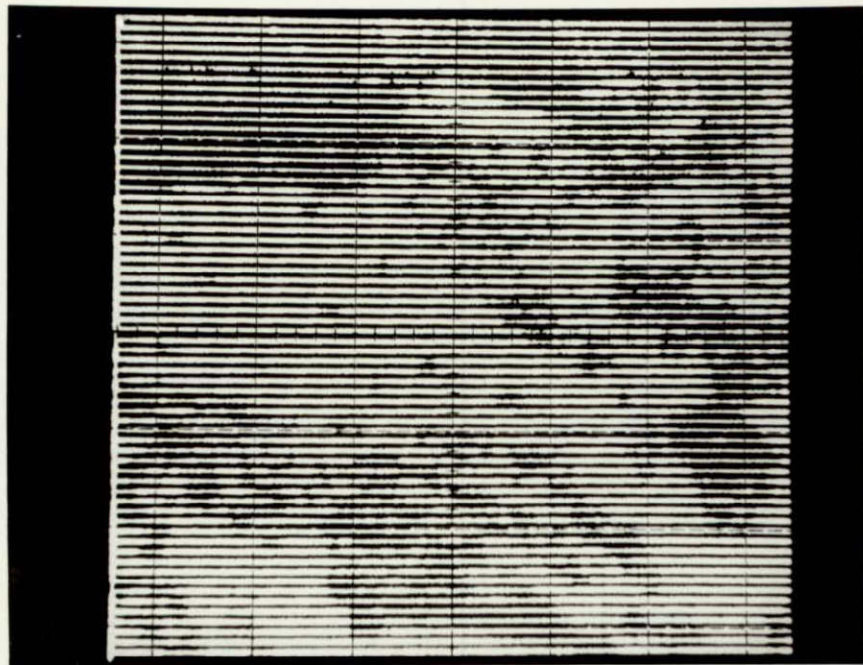


Auger Spectrum mapping for N at 383eV

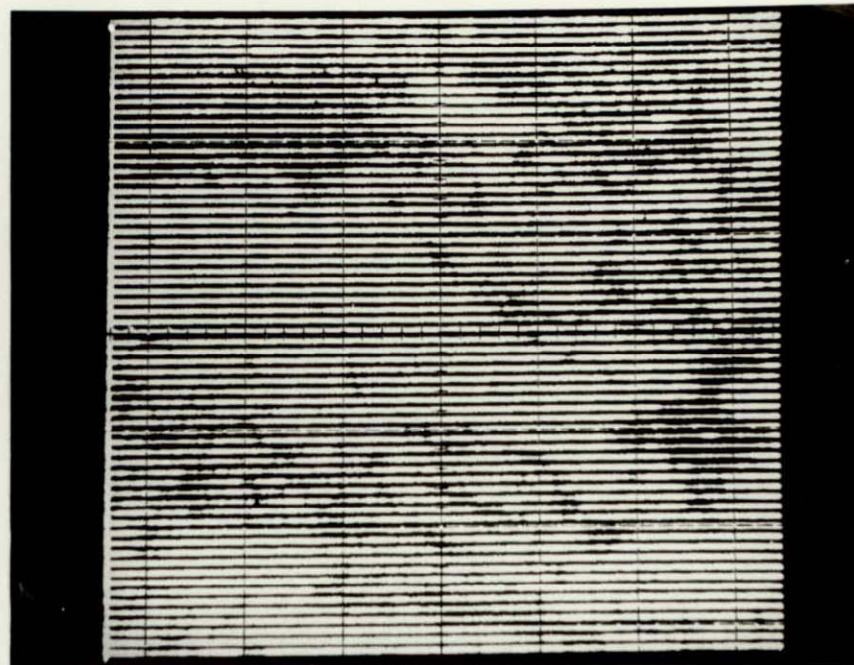


Auger Spectrum mapping for O at 510eV

Figure 49 Auger Spectrum mapping for N and O of the fracture surface of a notch bend specimen of Fe-12Ni-0.18Ti alloy heat treated at 820°C and tested at 77K.

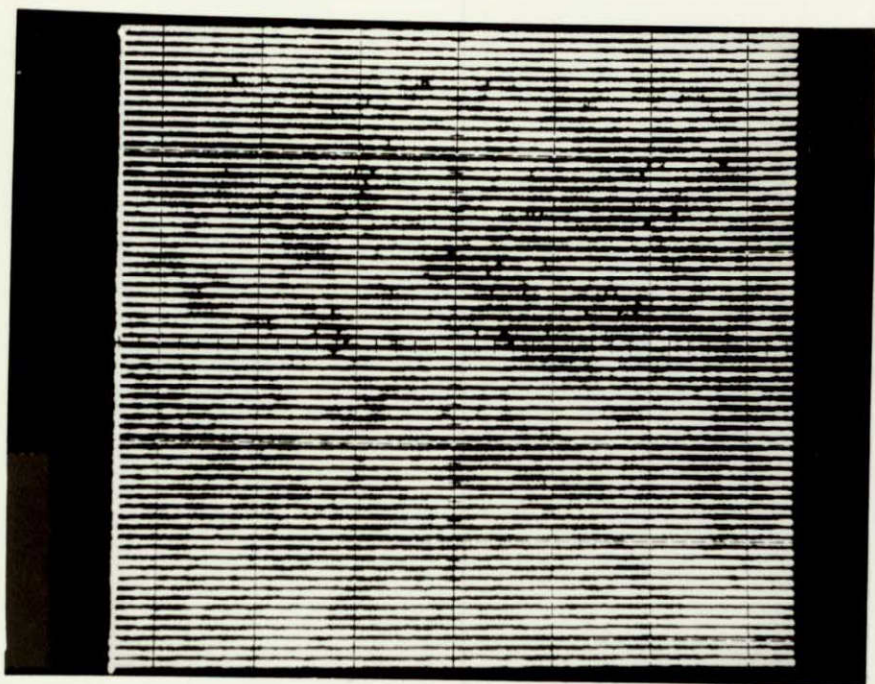


Auger Spectrum mapping for Ni at 847eV

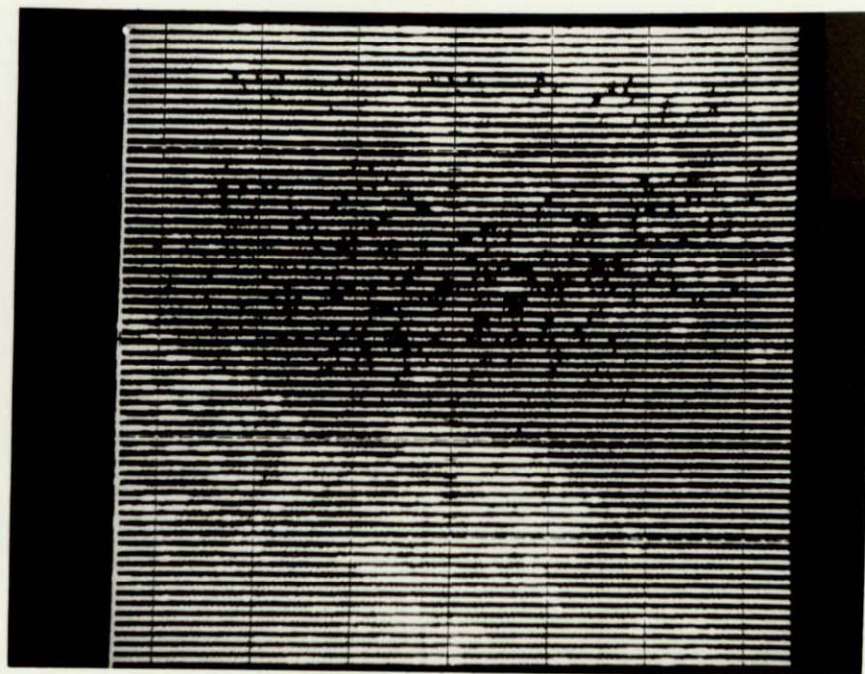


Auger Spectrum mapping for Fe at 595eV

Figure 50 Auger Spectrum mapping for Ni and Fe of the fracture surface of a notch bend specimen of Fe-12Ni-0.47Ti alloy heat treated at 820°C and tested at 77K.

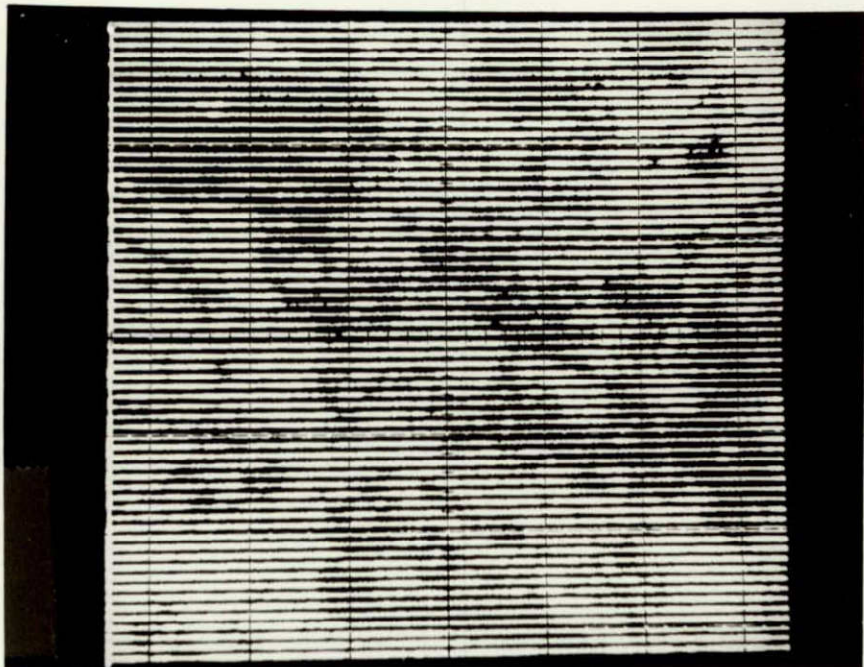


Auger Spectrum mapping for Ti at 417eV

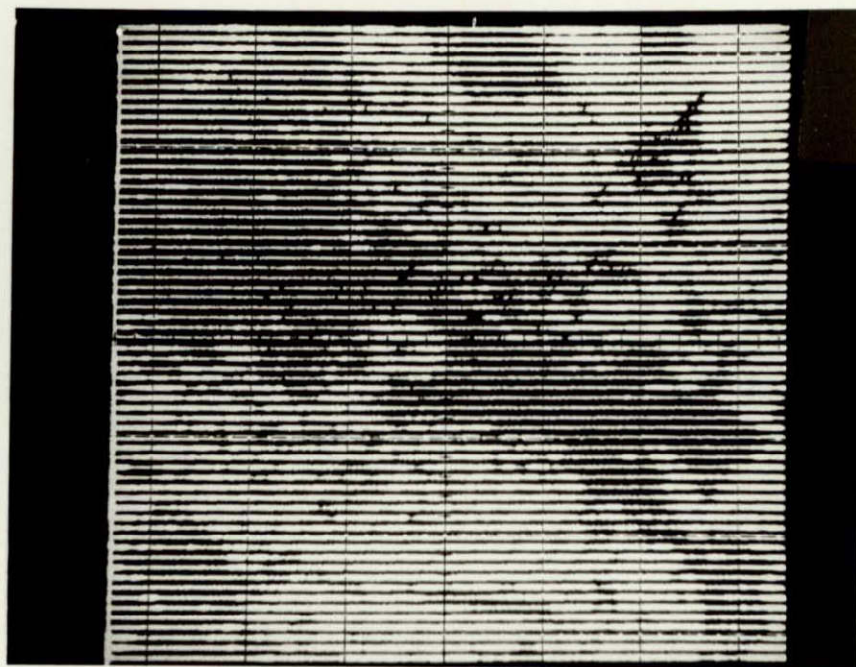


Auger Spectrum mapping for C at 271eV

Figure 51 Auger Spectrum mapping for Ti and C of the fracture surface of a notch bend specimen of Fe-12Ni-0.47Ti alloy heat treated at 820°C and tested at 77K.

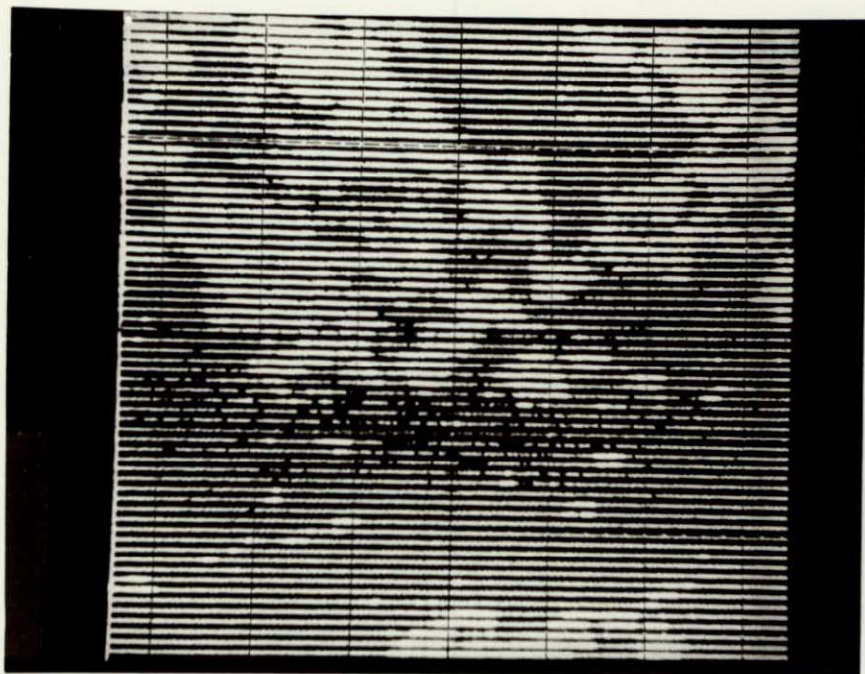


Auger Spectrum mapping for N at 383eV

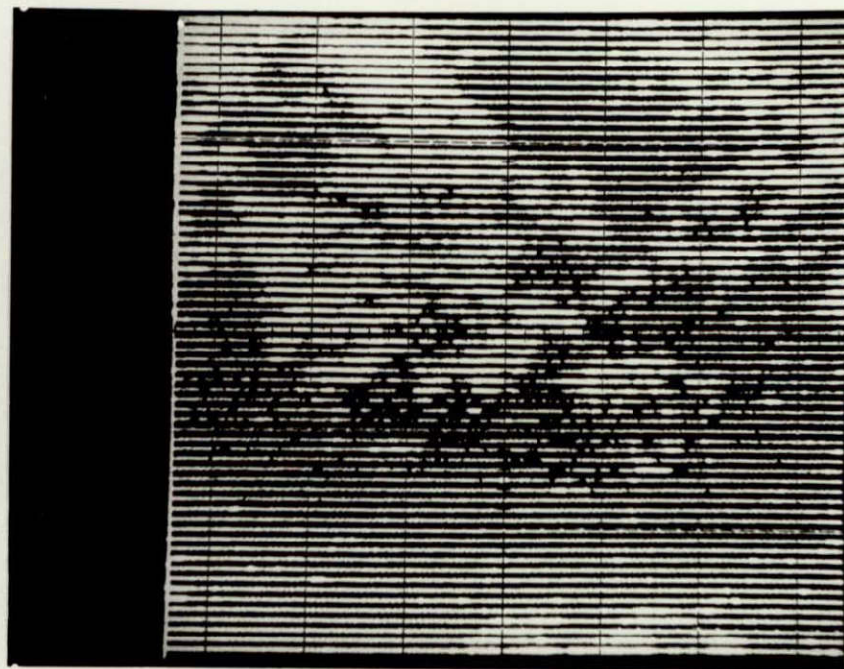


Auger Spectrum mapping for O at 510eV

Figure 52 Auger Spectrum mapping for N and O of the fracture surface of a notch bend specimen of Fe-12Ni-0.47Ti alloy heat treated at 820°C and tested at 77K.

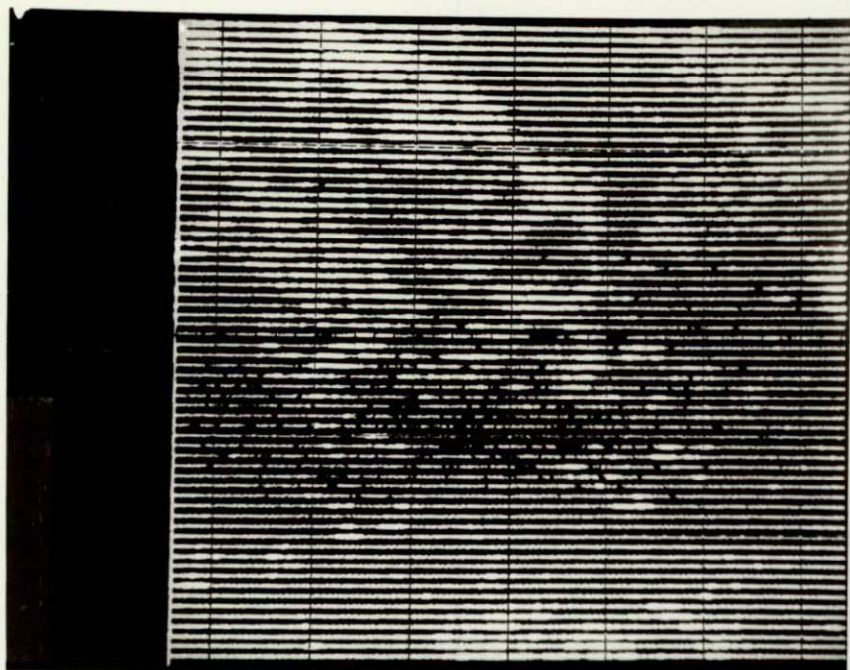


Auger Spectrum mapping for Ni at 847eV

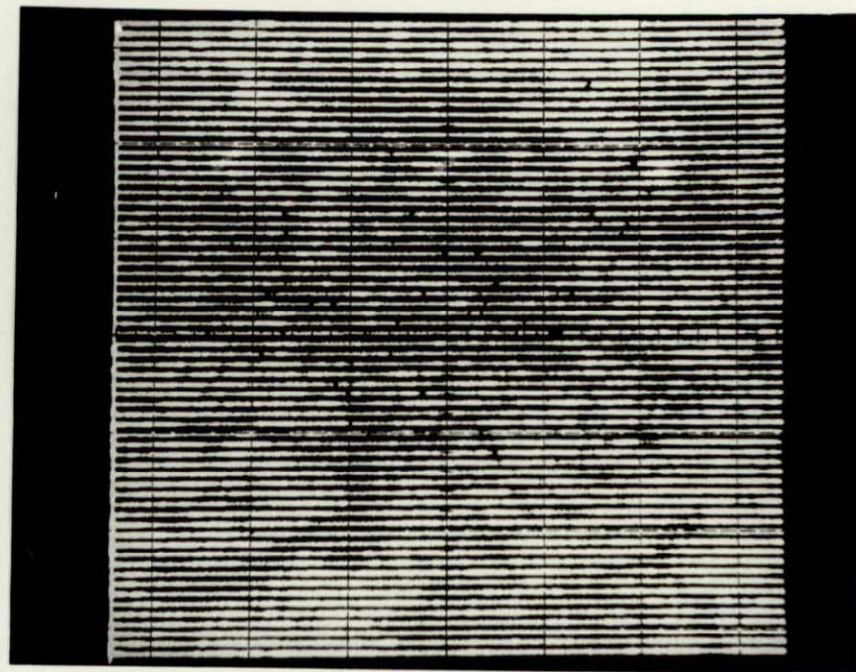


Auger Spectrum mapping for Fe at 595eV

Figure 53 Auger Spectrum mapping for Ni and Fe of the fracture surface of a notch bend specimen of Fe-12Ni-0.99Ti alloy heat treated at 820°C and tested at 77K.



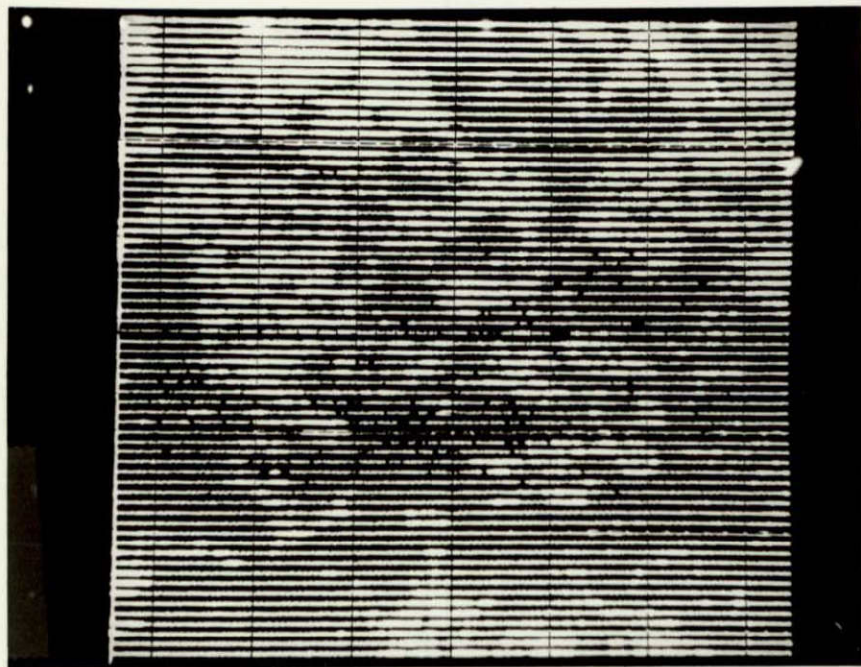
Auger Spectrum mapping for Ti at 417eV



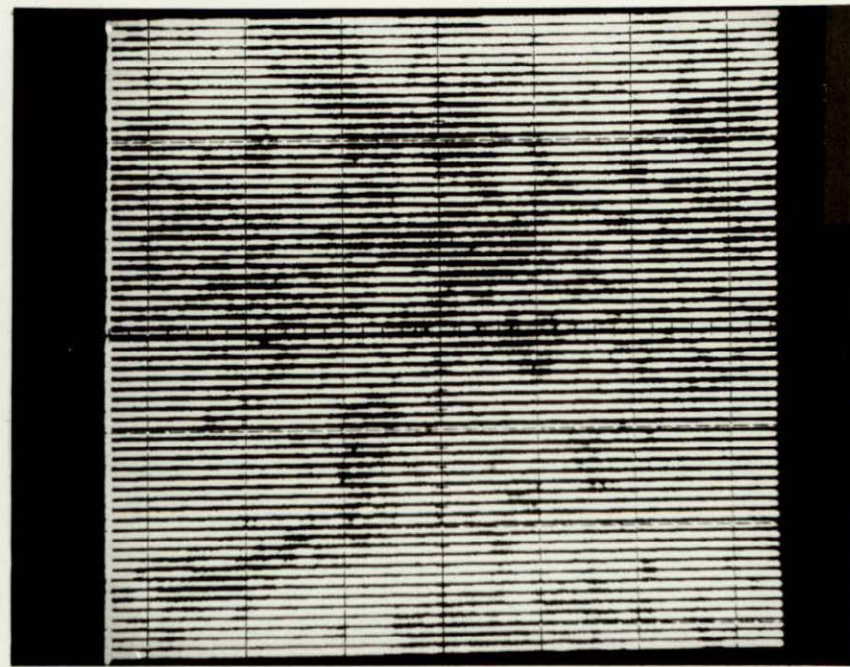
Auger Spectrum mapping for C at 271eV

Figure 54 Auger Spectrum mapping for Ti and C of the fracture surface of a notch bend specimen of Fe-12Ni-0,99Ti alloy heat treated at 820°C and tested at 77K,





Auger Spectrum mapping of N at 383eV



Auger Spectrum mapping for O at 510eV

Figure 55 Auger Spectrum mapping for N and O of the fracture surface of a notch bend specimen of Fe-12Ni-0.99Ti alloy heat treated at 820°C and tested at 77K.

ORIGINAL PAGE IS  
OF POOR QUALITY